University of Southampton Research Repository

UNIVERSITY OF SOUTHAMPTON

Optoelectronics Research Centre
School of Electronics and Computer Science

Developing an Environmentally Robust Optical Storage for Aerospace (EROS)

by

Senta L. Jantzen

A thesis for the degree of
Doctor of Philosophy

November 2021

University of Southampton

Abstract

Optoelectronics Research Centre
School of Electronics and Computer Science

Doctor of Philosophy

Developing an Environmentally Robust Optical Storage for Aerospace (EROS)

by Senta L. Jantzen

This thesis investigates the capability of using an optical platform as data storage for calibration data, which is used for harsh environments. The optical device is based on fibre Bragg gratings, which are fabricated with small spot direct ultraviolet writing (SSDUW).

Specifically, this work investigated different writing methods for co-locating gratings, aimed to achieve a high grating density to meet the required storage capacity. Co-locating more than 40 gratings have been achieved with two different techniques. For read out, a system was chosen that allowed the read out of both the spectral and the spatial domain and was able to differentiate between different grating types, and hence contributing to a larger data storage capacity. The three parameters contributing to the storage capacity per unit length are: number of co-located gratings, the ratio between spectral grating bandwidth and the bandwidth of the light source and the amount of grating types that can be distinguished between each other.

In this thesis not only the optical technology behind the storage device was investigated, but also the information technology required to translate calibration data into a spectral pattern and the correction methods to manage errors.

Through this work, numerous findings have been made; the evaluation of different inscription methods for co-located fibre Bragg ratings; achieving more than 40 co-located Bragg gratings using SSDUW; the inscription of individual cores of a multicore fibre using SSDUW; the use of machine learning algorithms to identify mechanical vibrational modes of a cantilever; the classification of gratings inscribed with SSDUW into the widely used grating framework.

Contents

List of Figures

List of Tables

Academic Thesis: Declaration Of Authorship

I, Senta Lisa Jantzen declare that this thesis and the work presented in it are my own and has been generated by me as the result of my own original research.

Title of thesis: Developing an Environmentally Robust Optical Storage for Aerospace (EROS)

I confirm that:

1. This work was done wholly or mainly while in candidature for a research degree at this University;
2. Where any part of this thesis has previously been submitted for a degree or any other qualification at this University or any other institution, this has been clearly stated;
3. Where I have consulted the published work of others, this is always clearly attributed;
4. Where I have quoted from the work of others, the source is always given. With the exception of such quotations, this thesis is entirely my own work;
5. I have acknowledged all main sources of help;
6. Where the thesis is based on work done by myself jointly with others, I have made clear exactly what was done by others and what I have contributed myself;
7. Either none of this work has been published before submission, or parts of this work have been published as shown in Appendix A.

Signed: ....

Date: ....

Acknowledgements

I am extremely grateful to my supervisory team. I would like to sincerely thank Dr Christopher Holmes for being such a fantastic supervisor, for striking the perfect balance between giving support and freedom throughout my PhD. I would also like to thank Prof Peter Smith for his technical expertise, his support and guidance during my project. I wish to thank Dr Mohammed El-Hajjar, who always made time to share his ideas and encoding expertise for this project. I am deeply grateful for the industrial support from Parker Aerospace, and would like to thank Dr Lewis Boyd for his creative ideas and inspiring curiosity.

A special thanks to EPSRC, the ORC and Parker Aerospace for making this exciting project possible and for allowing me as a PhD student to work on it.

I would like to thank all members of the PGRS group, who always made time for questions and conversations. Thank you, James Gates, Corin Gawith, Sam Berry, Rex Bannerman, Lewis Carpenter, James Field, Devin Smith, Matthew Posner, Salman Ahmed, Charlie Turner, Paul Gow, Paula Smith, Paolo Mennea and Alan Gray. And of course, the Silicon Photonics group; it was a pleasure to work with you!

Doing a PhD in Southampton has formed me as a person and I feel incredibly lucky and thankful for having been part of the University of Southampton and particularly of the Optoelectronics Research Centre. I would like to thank everyone I got to know during my time in Southampton. The conversations on the corridors or at the coffee machine really have made a difference to me. Special thanks to Angeles Camacho for her friendship and of course to Pearl John for sharing her infectious enthusiasm and passion of outreach with me and to Maurits de Planque for trusting me with the ESC Mentoring Scheme.

I would like to thank my family, my parents and my brother for believing in me, for supporting me and for always having a space for me to come home to.

And finally, to my husband Alex. You are such an inspiration to me. You make me a better person and motivate me to reach my goals and to go further. I have learned so much from you and I am incredibly lucky to have you in my life! I cannot thank you enough.

To my husband Alexander Jantzen and my parents Heidi and Jürgen Scholl. You have inspired and supported me throughout my PhD and far beyond. I dedicate this work to you.

Chapter 1

Introduction

1.1 Introduction

Commercial aviation has gained interest and popularity due to its convenience compared to other methods of transport. Before the COVID-19 pandemic, the number of people who chose to travel by plane steadily increased, as shown in Fig. 1.1 [3]. Although the COVID-19 pandemic caused the worldwide revenue passenger kilometres (RPK) to drop by 70% according to the International Air Transport Association (IATA) [4], the effects of COVID-19 on the RPK is expected to be only temporary [5]. This increase in global air travel, however, comes to the cost of the environment. Therefore the environmental responsibility for the aerospace industry has increased and the sector reacted to invest in new technologies to make flying more environmentally friendly. Research shows that flying has come far in regards to becoming a greener means of travel, for example by improving fuel efficiency. However, the increase in air travel has outpaced the technological improvement and the aviation industry is now taking stronger measures to react [6].

The European Commission released the Flightpath 2050, a report that presents Europe's Vision for Aviation [7]. This report was published in 2021 and one of the goals presented is the reduction in CO2 emissions per passenger kilometre by 75 %. In October 2021, the International Air Transport Association (IATA) released a press statement outlining the goal for achieving net zero carbon emission by 2050 [8]. The idea is that CO2 is reduced as much as possible with technology within the sector (such as increased operation efficiency, sustainable fuels, etc.), but also to utilise technologies that offset the carbon footprint with for example carbon capturing. One of the concrete actions listed in this release is the production of "radically more efficient airframe and propulsion technologies" [8]. Using more lightweight composite material has been identified a key technology to reduce the weight of an aircraft, which increases fuel efficiency and thus makes the operation of the aircraft more environmentally friendly [9]. Using these new composite materials instead of metal, however, removes the Faraday cage that used to protect electrical components such as electrical sensors. Optical components are seen as an important key player in this scenario as they are non-conductive and hence are less affected by lightning strikes. They have also gained much interest in this area, as an easy deployable solution that allow health monitoring of composite structures [10, 11]. Therefore, optical sensors have been progressively introduced to aerospace applications as they are small, lightweight and due to chemical inertness and their ability to operate in high temperature environments well suited for harsh environments [12, 13]. However, just like many electrical sensors, these optical sensors also require calibration as manufacturing processes cause a variation in the sensor. This typically means that without dedicated calibration, sensor offsets and responsivity are different. As a consequence, system integrators correct for this with each individual sensors by including additional circuitry that can perform in-situ corrections by setting calibration parameters during testing. For optical devices, this has to be done ex-situ by informing interrogation equipment of the appropriate calibration parameters to use when interpreting sensor data.

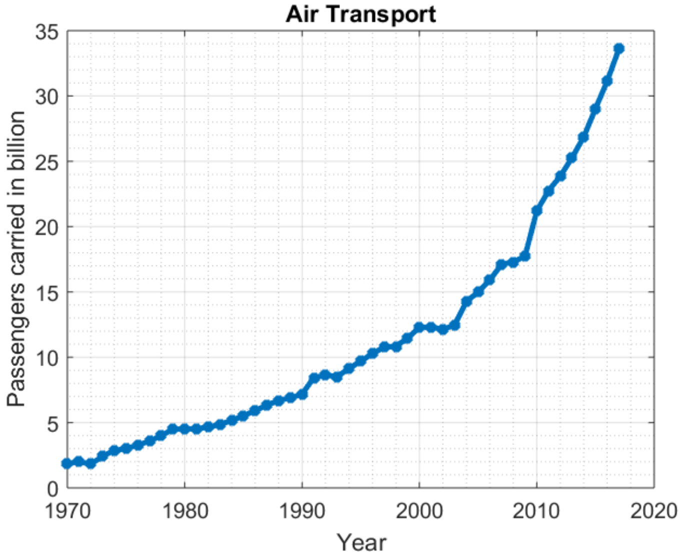

FIGURE 1.1: Passengers carried with air transport per year.

A look into the not too distant history of commercial avionics puts a dark reminder of the importance of sensor calibration: The Lion Air Boeing 737 MAX accident on October 2018. It has been one of two tragic accidents in the commercial aerospace industry that has led to the whole Boeing 737 MAX fleet to be grounded for almost two years. The final aircraft accident investigation report by the Komite Nasional Keselamatan Transportasi (KNKT) [14] and the summary of the FAA's review of the Boeing 737 MAX 8 [15] conclude that one cause of this accident was erroneous data from an angle of attack sensor, a sensor that measures the angle between the oncoming air and the longitudinal axis of the air plane. The erroneous sensor data was caused by a miscalibrated angle of attack sensor. This resulted in a reading that was 21° larger than the actual angle of attack. Due to a chain of other issues, this mis-calibration had not been noticed and the aircraft was declared fit to fly. This is a tragic example that shows the importance of correct calibration data for sensors in aerospace and as technology grows in complexity, the onus on inherently making the technology safer grows, too. This is one example that underlines how important and mission critical correct sensor data is.

Parker Aerospace, the industrial sponsor of this PhD project identified the importance of calibration data and set up this project in 2017 with the aim to create an all optical storage device for calibration data, which is directly attached to the sensor. If the calibration data is not physically attached to the sensor, the calibration data needs to be transferred to the avionics bay during the sensor install. Parker Aerospace wants to develop an all optical plug and play device, assuring that the correct calibration data is delivered together with the sensor as shown in Fig. 1.2. The sensor and calibration data package reduces the risk of human error during install, which could lead to calibration data being linked to the wrong sensor. An alternative solution could be running an electrical cable to every sensor to read the calibration data. This however would add additional weight and defeats the benefit of using optical sensors in the first place. Therefore, to align with the demand for more environmentally friendly aerial transport and to make use of the full capabilities of optical technologies, this sensor package is implemented as an optical system. This PhD CASE project was further funded by the Engineering and Physical Sciences Research Council (EPSRC) and followed up on a previous project called FIGRARO with the same supporting bodies [16]. While FIGARO aimed to develop the optical sensor, EROS, short for Environmentally Robust Optical Storage, aimed to provide the optical storage for its calibration data. Currently the calibration data for each sensor is manually transferred to the avionics bay. The creation of the optical storage will allow in-situ calibration data to be included and hence reducing the chance of incorrect values being used when reading sensor data for all optical devices.

1.2 EROS - Project Aim and Objectives

There are different ways of storing data optically and one of the most prominent optical storage is the compact disc, or more commonly known the CD. On this thin, round disc, pits and lands are inscribed on a spiral track, which form binary symbols that can be read out with a laser that follows the spiral track on the rotating disc [17]. Of course, a CD is not an ideal choice for an aerospace application. Therefore a different storage has to be developed. The read out system, which consists of the laser and the detector will be located in the avionics bay, while the sensor together with EROS will be located at the point of sensing. The storage device itself has to be in line with the sensor, it requires to be read out the same or similar way to the sensor and one should not affect one another.

An important criteria for the storage device EROS, is that it should be designed as an in-line solution, which fulfils two modes of operation: Read and Measure. ”Read” means that the calibration data will be read out and ”Measure” is when the sensor measurement is taken. If these two modes of operation can be separated from each other, then the full laser bandwidth will be available to both modes. This is under the assumption that the first device is transparent and does not block the transmission of a certain wavelength range to the device connected subsequently. If the system design however does not allow independent processes, the bandwidth must be shared. This means that the calibration data stored in EROS will have to be stored out of band of the measurement bandwidth for the FIGARO sensing data.

EROS needs to fulfil similar environmental specifications as the sensor itself and is preferably is co-located and installed together with the sensor. Fig. 1.2 shows the integrated sensing device, which can be implemented as plug-and-play device. This design enables quick and easy maintenance and reduces the risk of faulty installation. As both sensor and storage are implemented as one single device, EROS must be compatible with the sensor technology. A requirement of the FIGARO sensor was to be connected with a fibre and after considering both planar platform and fibre, the decision was made to implement EROS in fibre.

Further EROS requirements regard environmental considerations: the storage device shall operate in a thermal environment of -55 to +70°C and the performance shall be independent from local thermal fluctuations. The degree to which local thermal fluctuations are acceptable require further testing. EROS shall be fuel resistant.

This leaves the most critical parameter last: the storage capacity. The calibration data to be stored in EROS contains 37 floating point numbers, which can be found in Appendix B. There are different ways of calculating the binary representation of these floating point numbers and therefore different amounts of storage capacities that are required. However, as explained in Chapter 4 a minimum of 492 bits need to be stored. It should be noted that this only reflects data bits, and does not include additional error correction bits, which will most certainly be required.

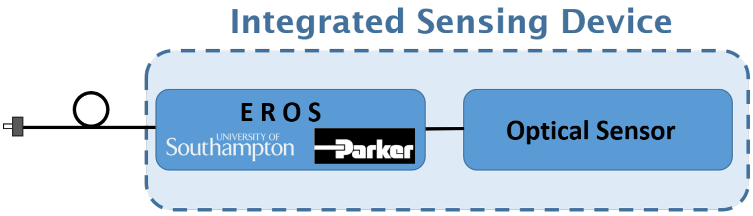

FIGURE 1.2: The optical storage EROS co-located with an optical sensor. They are packaged as one sensing device with sensor and calibration data in one package, allowing easy maintenance.

1.3 State of the Art

The idea of storing information spectrally by using Bragg gratings was patented in 1996 by Kashyap et al. [18]. Kashyap's patent explores storing a binary signal based on the presence (=1) or absence (=0) of a Bragg grating in an optical fibre for network addresses in optical communication networks. This patent only explores the spectral storage of data, which would in itself not provide sufficient storage space for the calibration data.

In 2002, a research group from Israel published a paper on data storage using spectral and spatial encoding [19]. Instead of only analysing the optical spectrum, they also took the physical location of the grating into consideration, which allowed more information to be stored in the fibre. This system was set up with a noise-like fibre laser, a spectrum analyser, a splitter, a mirror and the storage device. Instead of only storing single gratings, they also multiplexed grating structures such that multiple gratings were located on one position. Although they stated a theoretical storage capacity of 45 kbits, they only demonstrated a device with a storage capacity of 99 bits.

Englund et al. published a patent in 2007 which describes a technique similar to what was done by Keren et al. and to what is proposed in this thesis [20]. In his patent, he describes a multichannel Bragg grating, fabricated by superposition, which can be used to store data as a read only device. Although it is not mentioned how the investigation on multiple positions can be done, it is mentioned that is would be possible to differentiate between them.

In 2015, Castiglioni et al published a white paper describing an optical storage as a commercial product for in-line identification in fibre networks [21]. The idea is that instead of a red-light test, where light is shone through fibre from the distribution to the destination in order to check the connection. The OLiD (Optical Line Identification) however not only checks the connection, but is also used to inscribe the network address. Bragg gratings are used to represent the network address. This reduces the time for fault detection. On the specification sheet, which can be accessed through their website, Diamond SA mentions that up to 48 different addresses in a 70 nm range can be produced in the adapters [22]. The gratings are written out-of-band to not affect transmission capability. The storage capacity for the OLiD adapters is much smaller compared to the requirements for EROS.

1.4 Thesis Outline

This thesis is divided up into three pillars: Fabrication, Interrogation and Encoding. Each of those pillars forms an individual part of research. These are the three main components of the development of EROS data storage device as shown in Fig. 1.3.

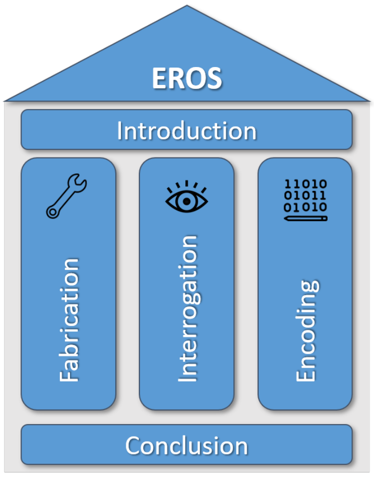

FIGURE 1.3: Thesis outline: Introduction and Conclusion form an overarching part, whereas Fabrication, Interrogation and Encoding are individual chapters.

Fabrication will cover the fabrication of the Bragg gratings, the different fabrication techniques and fibres used and will elaborate on benefits and drawbacks. This chapter explores the underlying principles and physical mechanisms of Bragg grating formation, particularly using small spot direct UV writing to inscribe the gratings. In this chapter, different writing conditions and parameters have been analysed, compared and evaluated against each other. Different techniques to co-locate gratings, creating a higher grating density in the fibre have been explored. Apart from single core fibre, experiments with multicore fibre have been conducted. These understandings formed the basis of publications, adding to the scientific knowledge in this field.

The second chapter, Interrogation focuses on the read out of the gratings. Besides the spectral interrogation, where only the spectral response of Bragg gratings is considered, a second system, Optical Frequency Domain Reflectometry (OFDR) is evaluated. The bandwidth of spectral interrogation can quickly be exhausted, as the bandwidth is not only limited by the bandwidth of the light source and the bandwidth of the grating, but also by the operating wavelength of the adjacent sensor (Figaro) as EROS might be required to operate out-of-band. OFDR allows not only the spectral, but also the spatial information of Bragg gratings to be analysed. It therefore allows spectral interrogations independently on multiple locations along the fibre, which enhances the amount of data that can be stored in a fibre. This chapter focuses on how OFDR works, on the different gratings types that can be differentiated between in both spectral and spatial domain and demonstrates the functionality on two EROS prototypes.

While the first two chapters focused on optical engineering, the third chapter takes a step back from optics and hones in on information technology. The chapter starts off with explaining number conversion and shows an efficient way of converting the calibration data into a binary format. Different ways are presented to store data in form of

Bragg gratings: non-binary, by dividing up the spectral bandwidth into smaller bins, where each bin represents one digit from 0-9; and binary, where a lookup table translates the spectral representation of Bragg gratings to a string of binary digits. This chapter also covers strategies on error correction, although these techniques are dependent on the experienced errors and further research will need to be conducted in order to draw a conclusion on error correction and hence the amount of data storage required.

The thesis closes with the Conclusion, which includes the conclusion from all chapters. The key findings are summarised and a way forward for future research is suggested.

Chapter 2

Fabrication

2.1 Introduction

The development of an environmentally robust optical storage (EROS) comes in three parts: Fabrication, Interrogation and Encoding. Fabrication is the first of three pillars that set the foundation of this project. Fabrication means building or manufacturing the device and in this project, it is the inscription of the calibration data to create the optical storage device. In EROS, the calibration data is stored in form of Bragg gratings. Bragg gratings are periodic refractive index changes inside a waveguide. When light is incident on a Bragg grating, the gratings reflects only a specific wavelength constructively, which can be measured with a power meter or an optical spectrum analyser. This wavelength specific reflection can be used to encode information.

Fibre Bragg gratings are used in various applications, for example in structural health monitoring, to measure strain, temperature, but also for filtering [23, 9]. Optical fibres, often made from glass, are chemically inert, can withstand high temperatures and are lightweight, which makes them an ideal candidate for the harsh environment of aerospace applications [24, 25, 26].

There are different ways to inscribe Bragg gratings into an optical fibre. The first time a Bragg grating has been inscribed was back in 1978 by Hill et al, where blue light was launched into a fibre [27]. The 4% back reflection on the cleaved end of the fibre caused a standing wave within the fibre core, which exposed and altered the refractive index in a periodic pattern. Since this technique allows only a limited variety in grating period (depending on the wavelength of the laser), different techniques have been developed to inscribe Bragg gratings with a different periodicity and mainly by exposing the fibre from the side, which was first introduced in 1989 [28]. One method, which is often used for industrial fabrication of Bragg gratings is by using phase masks, lithographic masks that contain the grating structure [29, 30]. Fibres exposed through these masks will have the desired pattern printed from the outside by illuminating through the cladding and core, rather than launching the light into the fibre. Another common way to fabricate Bragg gratings is by femtosecond point-by-point writing, where individual grating planes are inscribed after one another [31, 32, 33]. This chapter however, covers a very unique method to inscribe gratings: the small spot direct UV writing technique, where an interference pattern is used to inscribe the grating. The interference spot is only around 14 μm wide and allows the focusing of the spot into the fibre core. This unique technique is described in more detail in this chapter.

This fabrication chapter is organised as follows: Section 2.2 gives an overview on grating theory and cover the processes behind photosensitivity. Section 2.3 explains the small spot direct ultraviolet writing (SSDUW) technique, which was used to fabricate the Bragg gratings for this project. The writing parameters, the classification of gratings and the fabrication in different types of fibres are contained in Section 2.4. The chapter closes with the conclusion in Section 2.5

2.2 Background

2.2.1 Electromagnetic Theory

This section covers the background for light propagation in waveguides and Bragg gratings to understand the physical principles that give rise to the application of the optical data storage EROS.

The four Maxwell's equations below describe how electric and magnetic fields are generated, which set the foundation for classical optics:

$$\nabla \cdot \vec{E} = \frac{\rho}{\epsilon_0} \tag{2.1}$$

$$\nabla \cdot \vec{B} = 0 \tag{2.2}$$

$$\nabla \times \vec{E} = -\frac{\partial \vec{B}}{\partial t} \tag{2.3}$$

$$\nabla \times \vec{B} = \mu_0 \vec{J} + \mu_0 \epsilon_0 \frac{\partial \vec{E}}{\partial t} \tag{2.4}$$

The vector operator ∇ is the divergence, $\vec{E}$ is the electrical field, ρ the charge density and ϵ_0 the permittivity of free space. $\vec{B}$ is the magnetic field. $\nabla \times$ is the curl, another vector operator that indicates the circulation of a field. t is the time and μ_0 is the magnetic permeability of a vacuum. $\vec{J}$ is the electric current density, a measure for the charge that flows through a unit area in a certain time.

The first of the Maxwell's equations is also known as Gauss' law. Equation 2.2 is the equivalent for magnetic fields, describing that magnetic field lines do not diverge and that the magnetic flux density is source-free, has closed field lines, not allowing magnetic monopoles. The Maxwell-Faraday's equation, equation 2.3 describes that a change in the magnetic flux density results in an electrical field. This is similar to Ampere's law in equation 2.4, which describes that a magnetic field can be induced in two different ways: by an electric current or with a changing electrical field (displacement current).

Applying the Maxwell equations to the propagation of an electromagnetic field in a medium rather than a vacuum introduces electric and magnetic dipoles as the charges inside a dielectric material move in respect to the electromagnetic field. To account for these effects, the displacement vector $\vec{D}$ and the magnetising vector $\vec{H}$ are defined as

$$\vec{D} = \epsilon_0 \epsilon_r \vec{E} \tag{2.5}$$

$$\vec{H} = \frac{1}{\mu_0 \mu_r} \vec{B} \tag{2.6}$$

To apply the Maxwell's equation to propagation in optical fibre, the material constants ϵ_r (relative permittivity) and μ_r (relative permeability) are considered in addition to the free space constants ϵ_0 and μ_0 to account for the effect that the field encounters by the medium. Amorphous glass is assumed to be a linear, isotropic, non-conducting, non-magnetic medium with no free charges. Therefore, the Maxwell's equations simplify with $\vec{J} = 0$, $\nabla \cdot \vec{D} = 0$ and $\mu_r = 1$.

Taking the curl of equation 2.3 and inserting it in equation 2.4, with $(\nabla \times (\nabla \times \vec{E})) = \nabla(\nabla \cdot \vec{E}) - \nabla^2 \vec{E}$ results in

$$\nabla^2 \vec{E} = \epsilon_0 \epsilon_r \mu_0 \frac{\partial^2 \vec{E}}{\partial t^2} \tag{2.7}$$

with the speed of light in free space $c_0 = \frac{1}{\sqrt{\epsilon_0 \mu_0}}$.

The refractive index n is then defined as the ratio between the speed of light in free space and the phase velocity of the light in a medium:

$$n = \frac{c}{v} = \sqrt{\frac{\epsilon_0 \epsilon_r \mu_0 \mu_r}{\epsilon_0 \mu_0}} \tag{2.8}$$

The plane wave equation is a solution to equation 2.7 in the 3 dimensional space

$$\vec{E} = \vec{E_0} e^{i(\vec{k} \cdot \vec{r} - \omega t)} \tag{2.9}$$

with $\vec{r}$ as the position and $\vec{k}$ as the wavevector, which indicates the direction of travel and for light travelling in a straight line $\vec{k}_i = \frac{2\pi}{\lambda}\hat{\mathbf{i}}$. ω is the angular frequency and $\vec{E}_0$ is the field amplitude for each respective direction.

It should be noted that the equations for the magnetic field equations are equivalent to the equations for the electric field above.

2.2.2 Waveguides

Most of the devices fabricated in this thesis were based on fibre. Both platforms require a waveguide, a structure for the light to propagate in. The planar waveguides in this thesis are inscribed with the small spot direct UV writing technique, which is further explained in Section 2.3. All optical fibres that were used in this thesis already had a guiding channel, the fibre core(s). Since the majority of devices for this thesis were fabricated on the fibre platform, the focus of this chapter will be the guiding of light in a fibre, however, it should be noted that the principles are applicable to planar waveguides as well.

The resulting direction of travel for the light is along $\hat{\mathbf{z}}$, the light ray inside the core however, experiences total internal reflection and bounces off the core-cladding interface as indicated in Fig. 2.1. This schematic shows the vertical cross section of a fibre with the core in the middle and the cladding on top and bottom. For a refraction angle θ_r of above 90°, the light is reflected back into the core. Applying this to Snell's Law [35]

$$n_1 \sin(\theta_i) = n_2 \sin(\theta_r), \tag{2.10}$$

with the angle of incidence θ_i and the refractive indices n_1 and n_2 of the respective material, results in a critical angle $\theta_c = \sin^{-1}(\frac{n_2}{n_1})$. This means that under these conditions total internal reflection occurs and all incident power is reflected and maintains the light in the core of the fibre.

It is worth noting here, that there is a small evanescent field that extends into the cladding and decays rapidly as shown in the schematic in Fig. 2.2a [34, 36].

The power plot in Fig. 2.2b shows the amount of power transmitted in the cladding and in the core. The fractional power transmitted in the core $\left(\frac{P_{core}}{P_{tot}}\right)$ for a single mode fibre can be calculated using the following equations [34, 36] with

$$\frac{P_{core}}{P_{tot}} = \left[\frac{W^2}{V^2} + \frac{U^2}{V^2}\frac{K_0^2(W)}{K_1(W)K_{-1}(W)}\right], \tag{2.11}$$

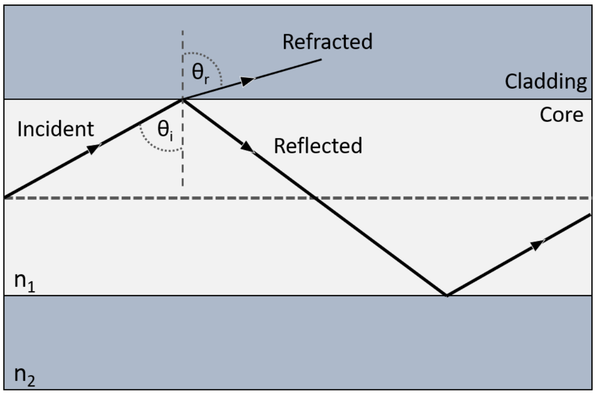

FIGURE 2.1: Schematic of light travelling in a waveguide, indicating the refracted and reflected wave.

with the modified Bessel function K_i, using the function parameters W and U, together with the propagation constant β, vacuum wave vector k_0, the normalised propagation constant b, the V-number $V = k_0 a\sqrt{n_1^2 - n_2^2}$ for the core radius a and refractive indices of the core and cladding n_1 and n_2.

$$W = a\sqrt{(\beta^2 - k_0^2 n_1^2)} \tag{2.12}$$

$$U = a\sqrt{(k_0^2 n_1^2 - \beta^2)} \tag{2.13}$$

$$\beta = \sqrt{k_0^2(b(n_1^2 - n_2^2) + n_2^2)} \tag{2.14}$$

$$k_0 = \frac{2\pi}{\lambda} \tag{2.15}$$

The V-number for a single mode fibre is between 0 and 2.4048 to only support the fundamental LP_{01} mode. More detail about the calculation can be found in various textbooks and papers such as [34, 36].

The mode leaking into the cladding has consequences in regard to calculating the central wavelength of a fibre Bragg gratings, when the refractive index is not just the refractive index of the core, but the *effective* refractive index. The effective refractive index is a value in between the refractive index of the core and the cladding and represents what the mode is ”seeing” when travelling through the fibre. A closer look into Bragg gratings will be taken in the following section.

2.2.3 Bragg Gratings

Bragg gratings are periodic refractive index patterns in a waveguide, which cause light to partially reflect. By placing these partial mirrors a particular distance apart, only the

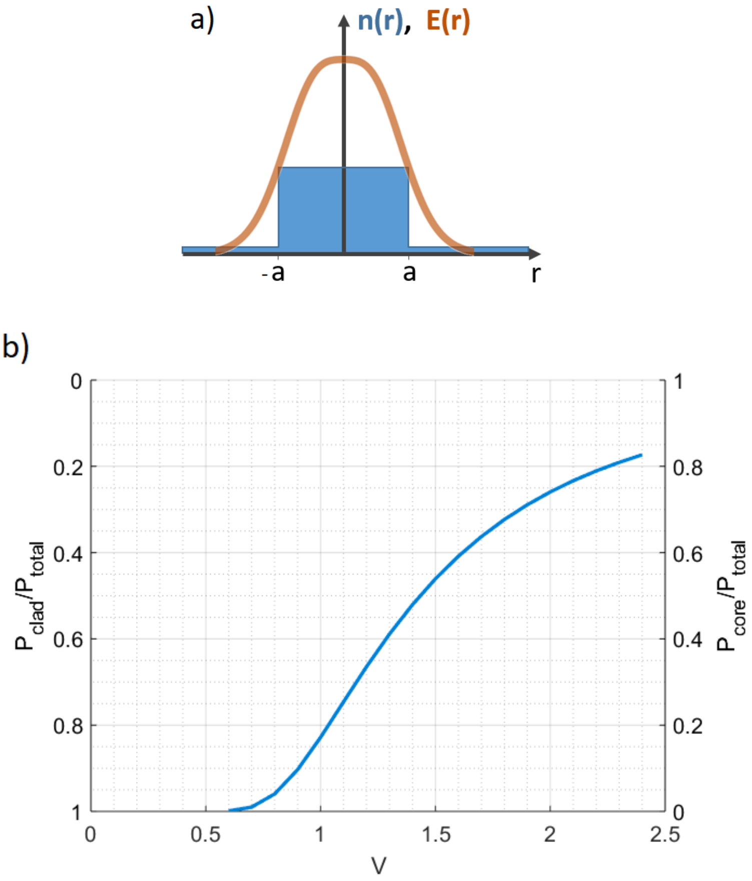

FIGURE 2.2: a) Schematic diagram of the mode distribution in regard to the refractive index profile. Most of the power travels in the core (high index region) and a small amount of power in the cladding (low refractive index region) b) This graph shows the fractional power travelling in the core and cladding for a single mode fibres.

reflections of a certain wavelength interfere constructively, which results in a peak in the reflection spectrum and a dip in the transmission spectrum as indicated in Fig. 2.3.

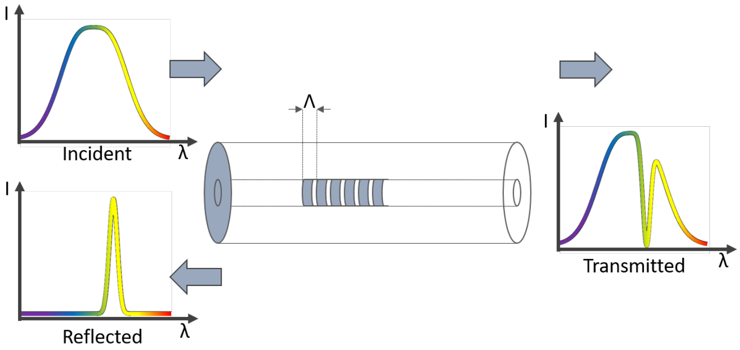

FIGURE 2.3: An example of how a Bragg grating works: Incident light on a Bragg grating results in a dip in the transmission and a peak in the reflection spectrum.

Snell's law in equation 2.10 states that radiation incident at an interface with a different refractive index will be reflected under a certain angle. For the reflected light to interfere constructively the wavevector and the physical spacing of the grating Λ needs to be matched. It is assumed that energy and momentum is conserved, therefore the wavevector of the incident wave k_i and grating spacing K must be equal to the backwards propagating wave k_r:

$$k_r = k_i + K \tag{2.16}$$

To ensure energy conservation, the frequencies of the incident and the reflected wave must be equal: $k_i = -k_r$. Substituting the wavevector $k = \frac{2\pi}{\lambda} n_{\mathrm{eff}}$ in equation 2.16 results in:

$$-\frac{2\pi}{\lambda} n_{\mathrm{eff}} = \frac{2\pi}{\lambda} n_{\mathrm{eff}} - \frac{2\pi}{\Lambda} \tag{2.17}$$

which can be rearranged to the Bragg equation, where λ_B represents the central wavelength of reflection:

$$\lambda_B = 2 n_{\mathrm{eff}} \Lambda \tag{2.18}$$

This equation is important to define the spectral position of the Bragg grating, however it does not make any prediction about the grating's amplitude or bandwidth. To analyse these features, coupled mode theory can be used. This thesis focuses on the key parameters for uniform Bragg gratings which are given with the following equations, however, more detail about coupled mode theory can be found in [34] and [37]. The peak reflection R can be calculated with

$$R = \tanh^2\left(\frac{\pi \delta n_{\mathrm{ac}} L}{\lambda_B}\right), \tag{2.19}$$

with the grating length L and the refractive index contrast of the Bragg grating δn_{ac}.

The bandwidth $\Delta\lambda$ is given by

$$\frac{\Delta\lambda}{\lambda_B} = \frac{\delta n_{\mathrm{ac}}}{n_{\mathrm{eff}}} \sqrt{1 + \left(\frac{\lambda_B}{\delta n_{\mathrm{ac}} L}\right)^2} \tag{2.20}$$

From equation 2.19, one can see that the grating reflection increases for a longer grating with a higher refractive index contrast. The bandwidth depends on the grating regime as there are two different regimes: weak gratings with $\delta n_{\mathrm{ac}} L \ll \lambda_B$ and strong gratings. For weak gratings, the bandwidth depends on the length of the gratings, hence these are called "length-limited" [37]:

$$\frac{\Delta\lambda_0}{\lambda_B} \rightarrow \frac{\lambda_B}{n_{\mathrm{eff}} L} \tag{2.21}$$

The bandwidth of strong gratings are limited by the refractive index contrast:

$$\frac{\Delta\lambda_0}{\lambda_B} \rightarrow \frac{\delta n_{\mathrm{ac}}}{n_{\mathrm{eff}}} \tag{2.22}$$

The difference in grating profile and spectral response between uniform and Gaussian apodised gratings structures is shown in Fig. 2.4. The refractive index profile is of uniform strength for uniform gratings and with a Gaussian apodisation for Gaussian apodised gratings. Non-uniform gratings can be described and analysed by combining a series of uniform gratings with different amplitude. The benefit of Gaussian apodised grating is the side lobe suppression in their spectral response as shown on the right side of Fig. 2.4. These side lobes appear for uniform gratings, because these gratings abruptly begin and end. The Fourier transform of such structures results in a sinc function, which causes these side lobe structures. A Gaussian apodisation however, yields in a Gaussian structure, without such side lobes. [38]

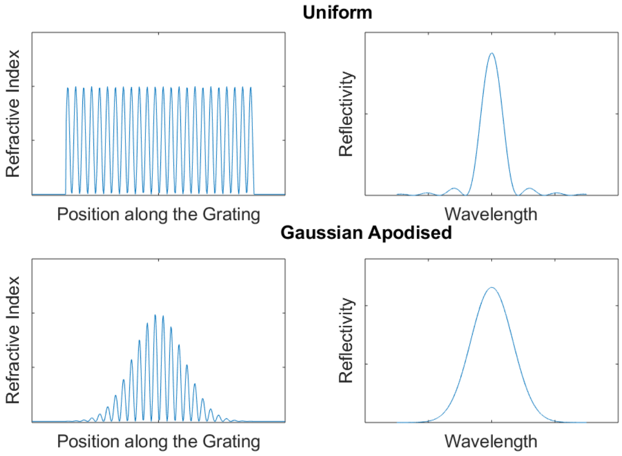

FIGURE 2.4: Bragg gratings can be written with different apodisation. This is an overview of the two most commonly used apodisation within this thesis: uniform and Gaussian apodised. The left plot shows the grating in the spatial, the right plot in the spectral domain.

EROS made use of different gratings types, among them both uniform and Gaussian apodised gratings. The different grating types allowed a distinction to be made between the spectral response of the shapes during read-out, which then enabled another dimension for encoding. This will discussed further in the Interrogation chapter.

2.2.4 Photosensitivity and Hydrogenation

Bragg grating inscription techniques have changed greatly with time, yet the underlying processes for achieving a refractive index change using ultraviolet light are not completely understood. It is broadly agreed that there are two mechanisms responsible for the index change described in the colour centre model and the densification model.

A colour centre is a defect in the lattice structure, leading to irregular spacings and vacancies. These defects can create an excess of electrons, which enhances the absorption. The colour centre model describes the change of colour centres and modification of the absorption spectrum resulting from UV exposure [39]. The change in absorption then results in an alteration of the refractive index according to the Kramers-Kronig relations:

$$\Delta n(\lambda') = \frac{1}{2\pi^2} \cdot \fint_{\lambda_1}^{\lambda_2} \frac{\Delta\alpha(\lambda)}{1-(\frac{\lambda}{\lambda'})^2} d\lambda \tag{2.23}$$

where $\Delta n(\lambda')$ defines the refractive index change at λ', $\Delta\alpha$ is the change in absorption and λ_1 and λ_2 are the spectrum boundaries. In other words, the fibre absorbs the light of a certain wavelength range (λ), which causes a change in refractive index at another wavelength (λ'). This means that a change in refractive index can be achieved without inducing higher losses at the wavelength of interest [40].

The densification or compaction model on the other hand states that radiation induces changes in the density of the material and hence alters the refractive index of the material [41]. This effect is expected to be prevalent for high doses of UV radiation [39], [42].

Depending on the UV dose, either model or a combination of both are believed to be causing the refractive index change through UV exposure of doped silica glasses.

Silica glasses with a low Germanium concentration, which are not considered to have an enhanced photosensitivity can be hydrogen loaded to enhance the photosensitivity. Corning's SMF28 is an example of such fibre. During hydrogen loading, hydrogen diffuses into the glass and after exposure, Germanium-OH bonds and Germanium oxygen deficiency centres are formed, which absorb UV and increase photosensitivity [39, 43, 38]. This technique has been used to treat optical fibre with a low photosensitivity.

2.3 Small Spot Direct UV Writing Technique

Small Spot Direct UV Writing (SSDUW) is a technique that is used to create waveguides and Bragg gratings simultaneously in planar samples as well as writing Fibre Bragg Gratings (FBGs) in the core of a fibre. This technique is a modification of the transverse holographic method, which was first reported in 1989 by Meltz et al. [28]. They illuminated the core of a fibre from the side with a 244 nm laser in a two-beam interferometer and reported a resulting focal spot of approximately 4 mm by 125 μm. Several variations of this technique were since developed [44, 45, 46]. Historically the research group in Southampton referred to this technique as small spot direct UV writing due to the overlapping spot being focused down to only a couple of microns [47, 48, 49]. The SSDUW fibre set up is displayed in Fig. 2.5

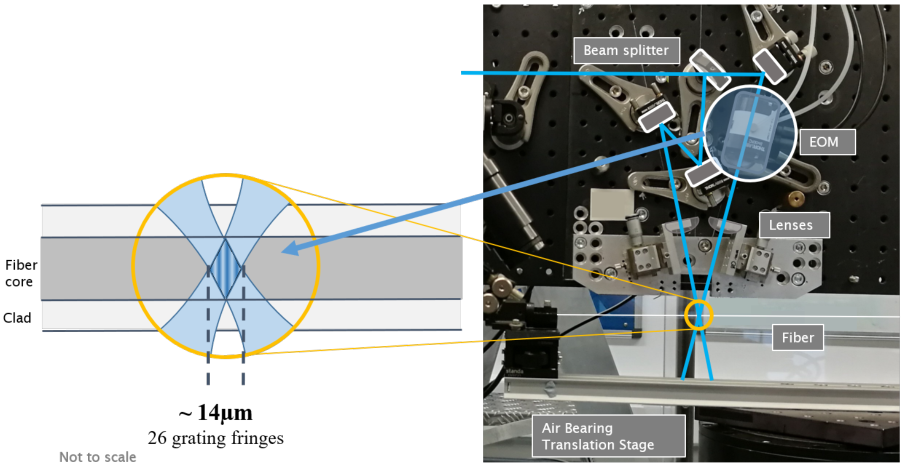

FIGURE 2.5: SSDUW set up for fibre writing: The fibre is clamped in on two fibre mounts. An interference pattern is created by splitting the 244 nm laser light into two arms and combine them onto a single spot in the core of the fibre. One beam path passes through an Electro-Optical Modulator (EOM), which allows phase tuning and hence movement of the interference fringes in the core of the fibre.

A planar sample or a fibre is mounted on a nanometre precision four-axis air bearing translation stage from Aerotech. Fibre samples are stripped before writing and clamped into fibre holders on both ends with an applied tension of 0.5 N to restrict movement and avoid dropping of the middle section of the fibre. Planar samples are placed on three-axis ball bearing translation stage with a vacuum chuck.

A beam of a 244 nm frequency-doubled argon-ion laser light is divided up into two arms before being focused and combined into a 14 μm diameter interference spot in the core of a fibre, or a 7 μm spot on a planar sample. The fixed crossing angle of $\theta = 26.9 \pm 0.4^\circ$ defines the interference pattern spacing and therefore the central Bragg wavelength. With the laser wavelength $\lambda_{UV} = 244$nm, the period of the interference pattern can be calculated with the following equation [50]:

$$\Lambda = \frac{\lambda_{UV}}{2sin(\frac{\theta}{2})}, \tag{2.24}$$

Under the above mentioned conditions, the interference pattern is designed to have a grating period of $\Lambda = 524 \pm 8$ nm.

An electro-optic modulator (EOM) driven with a sawtooth signal is introduced into one of the interferometer arms. The triggering of the saw-tooth signal is synchronised with the translation of the fibre. The spatial period of the sawtooth wave defines the Bragg period, allowing for wavelength detuning [51, 52].

As stated in Section 2.2.3, the period Λ of the periodic refractive index pattern defines the Bragg wavelength λ_B that it reflects according to the Bragg equation. The translation velocity of the fiber, the spot size and the power of the laser define the fluence, the energy density that is introduced into the core. The fluence is measured in $\frac{kJ}{cm^2}$ and typically ranges between 1-40 $\frac{kJ}{cm^2}$ in photosensitive fibre. The inscription time of a grating is dependent on the laser output power and the fluence as with a slower translation speed, a higher energy density and therefore higher fluence can be achieved.

2.4 Fibre Writing

This section describes the characteristics of Bragg grating fabrication using the SSDUW technique for different types of fibre and focuses on different grating types that can be achieved with this technique. SSDUW is a particularly good technique for multicore writing, which will be discussed further in Section 2.4.4.

2.4.1 Writing Characteristics and Parameters

Different types of fibres require different writing parameters in order to achieve a refractive index change in the core. This project focused on the following three different fibre types:

- SMF28 (Corning): a standard telecommunication fibre with an operating wavelength of 1260 - 1625 nm, a core diameter of 8.2μm and a numerical aperture of 0.14 [53]
- GF4A (Nufern): a cladding mode offset photosensitive fibre developed for Bragg grating fabrication with an operating wavelength of 1500 - 1600 nm, a core diameter of 3.5μm and a numerical aperture of 0.30 [54]
- PS-PM980 (Nufern): a photosensitive polarisation-maintaining fibre with an operating wavelength of 970 - 1550 nm, a core diameter of 6.0μm and a numerical aperture of 0.12 [55]

Each of these fibres have a different glass composition, which alters the writing parameters to achieve the same grating response. As mentioned in Section 2.3, the wavelength variation, also referred to as detuning, is achieved by synchronising the movement of the fibre on the stage and the sawtooth pitch of the EOM signal. Therefore detuning is expected to be largely independent from the fibre type and PS-PM980 has been chosen to visualise the detuning curve.

To fabricate a detuning curve, several 5 mm gratings with a Gaussian apodisation profile were written at a fluence of 40 kJ/cm^2 in a randomised order to reduce misalignment effects. To characterise the detuning, gratings were written from 1235-1650 nm, however only gratings within 1362 - 1599 nm were observed (see Fig. 2.6). Gratings written outside of this area (1235-1347 nm and 1599-1650 nm) did not result in a sufficient periodic effective index change to create Bragg gratings.

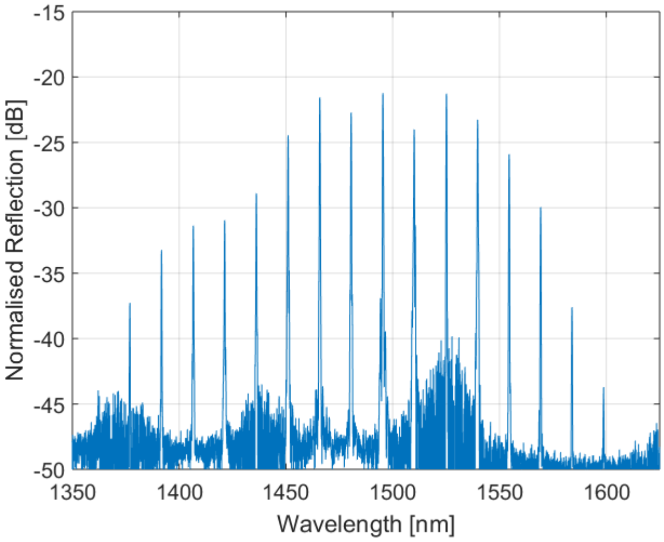

FIGURE 2.6: Detuning Curve for PS-PM980 (Cyclops 40)

The detuning curve in Fig. 2.6 shows a steeper drop off at longer wavelengths compared to the flatter decrease in gratings strength at shorter wavelengths. This indicates the writing barriers for grating fabrication using the writing board with a crossing angle of 26°. As mentioned in Section 2.2, the reflection of weaker gratings on either side of the detuning curve could be adjusted by increasing the fluence (achieving a higher refractive index contrast and hence increasing the grating stregth) or by increasing the grating length, should an equal reflectivity be desired.

For the purpose of an optical storage with an interrogation that will be described in Chapter 3, it is desired that all gratings occupy the same physical space. Therefore the length of the gratings was fixed. The other dial to turn is the refractive index change, which is influenced by the fluence. Therefore the effect on fluence has been analysed, which for the SSDUW technique is defined by the speed that the sample travels underneath the laser spot. Up to a point of saturation, a higher fluence will increase the "ac" of the refractive index change; it will result in a higher grating contrast and therefore a stronger reflection [37].

The fluence curve is generally expected to be different for different fibres, as absorption varies for different glass composition. In Fig. 2.7, the fluence curves for GF4A and PS-PM980 are shown. These are both photosensitive fibres and show a similar fluence trend. The distinct dip around 30 kJ/cm^2 will be addressed in Section 2.4.2 along with

TABLE 2.1: Overview of grating types according to [2]

Grating Type	Description
Type I	Gratings show a red shift during inscription. Gratings are found in photosensitive fibres. Thermally stable up to around 320°C.
Type In	Usually follow from Type I gratings, when a roll over occurs. Gratings can present a blue shift in the central wavelength. Thermally stable to up to 800°C.
Type IH	Hydrogen loaded gratings with a similar behaviour to Type I gratings. Usually thermally stable to less than 320°C.
Type IHp	Follow up from Type IH gratings. Show higher thermal stability of up to 500°C.

the fluence curve for SMF28 as this allows the classification of different grating types and hence certain features of the grating. For Fig. 2.7, the fluence was again randomised to reduce misalignment effects and 11 Gaussian apodised gratings with a length of 5 mm at fluences from 1 -100 kJ/cm^2 were written in 10 kJ/cm^2 steps.

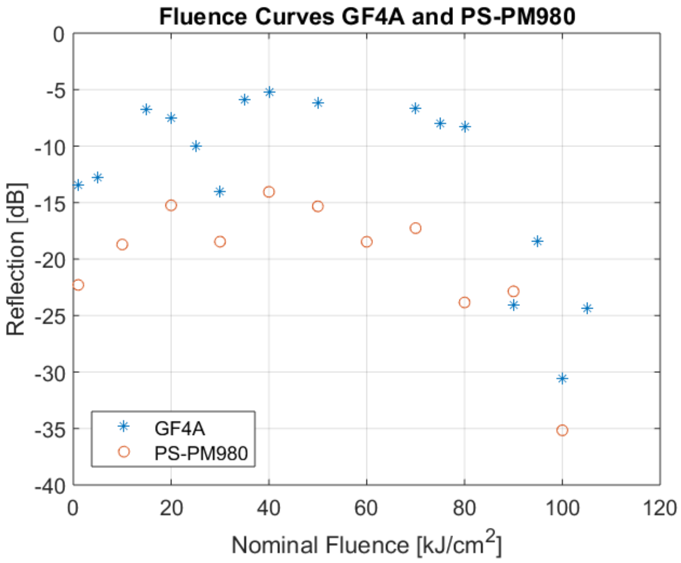

FIGURE 2.7: Fluence Curve for PS-PM980 (Cyclops 39) and GF4A (Cyclops 45) written with the small spot direct ultraviolet writing system.

2.4.2 Classification of Grating Types

For the fabrication of Bragg gratings with UV exposure, the material is required to be photosensitive. As mentioned in Section 2.2.4, there are two mechanisms involved in changing the refractive index of a material with UV radiation: colour centres and densification. The type of mechanism has an impact on the properties of the Bragg gratings, especially regarding their resilience to temperature [2]. Table 2.1 shows an overview of the different gratings types, which were identified in the following experiments.

In Germanium doped fibre, such as GF4A, a *Type I* grating (positive index) will shift to longer wavelengths during continuous exposure, as the effective refractive index increases along with the Bragg wavelength according to the Bragg condition. With further exposure, the grating response will then decrease, which is known as roll over point and then slowly increase again whilst shifting to shorter wavelengths, which marks the onset of *Type In* gratings. The spectral blue shift is based on negative index contributions. At the roll over point, the positive and negative index contribution cancel each other out, resulting in a weaker grating response.

Different grating types have specific characteristics; *Type In* gratings for example are more resilient to higher temperatures, this is because the prolonged UV exposure caused the material to densify. *Type I* gratings on the other hand experience less UV exposure and the refractive index change is caused by color centres, which are caused by a change in atomic bonds. These bonds are more sensitive to high temperatures.

Monitoring the grating response during exposure is a common technique to fabricate gratings of a certain type, however, it is not applicable to the SSDUW. SSDUW is a sequential writing technique, also known as direct writing and the grating is built up consecutively, a couple grating planes at a time [56]. The effect of UV exposure to the optical spectrum cannot be analysed for sequential techniques as with time the grating dimensions increases rather than the refractive index profile. As the resilience to temperature presents itself as good indicator for determining the grating type, heat treatment was used for characterisation [1].

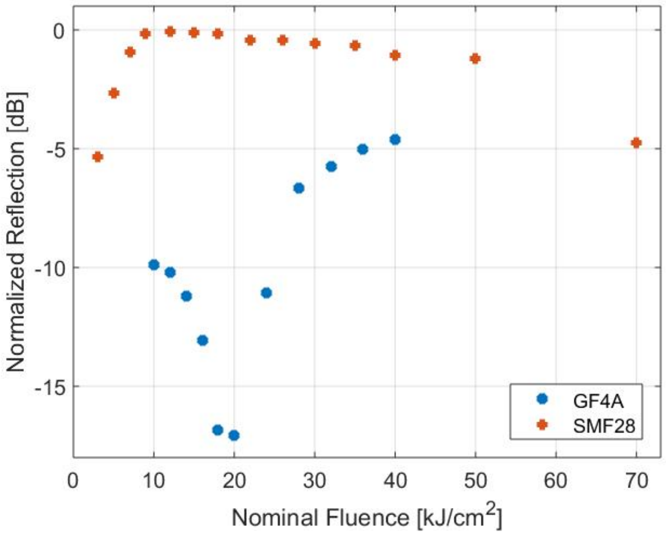

FIGURE 2.8: Fluence Curve at room temperature for GF4A and SMF28. The characteristic dip in the GF4A curve marks the onset of grating *Type In*. This dip cannot be seen for SMF28 [1].

To analyse the grating types for SSDUW, 11 gratings were written with different fluences into GF4A in a range from 10-40 kJ/cm^2 and 14 gratings in SMF28 with fluences

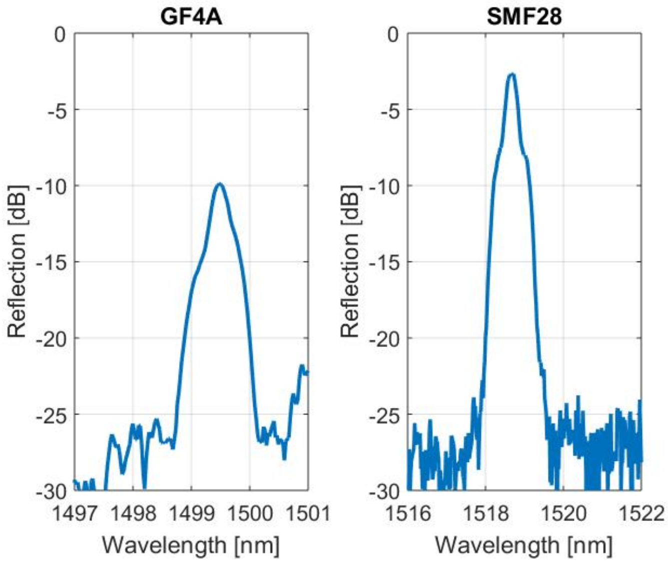

FIGURE 2.9: Reflection spectrum of a single Gaussian apodised Bragg grating in GF4A and SMF28 [1].

between 1-70 kJ/cm^2 (see Fig. 2.8). The fluence describes the energy per surface area and therefore defines the UV exposure dose of the grating. It can be adjusted through the movement speed of the fibre: the slower the fibre moves along, the longer UV exposure. It is equivalent to exposure time for non-sequential writing techniques assuming a constant laser power. The laser power is used as an input to then calculate the required translation speed to achieve a certain fluence. We therefore only report on the fluence.

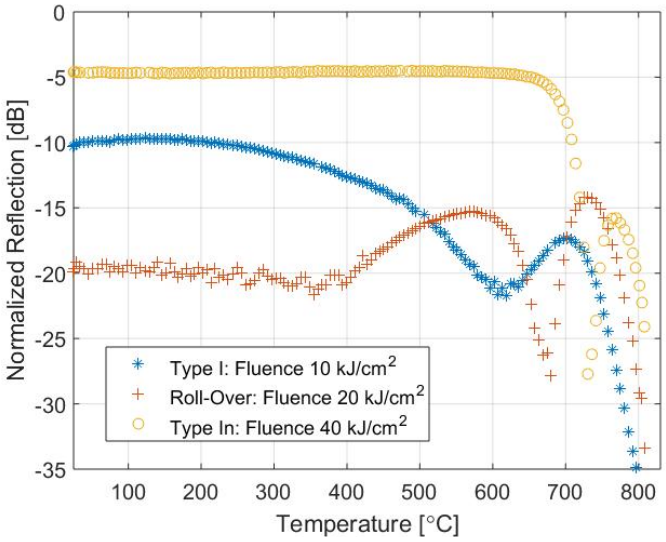

FIGURE 2.10: Peak over time during thermal treatment of GF4A fibre Bragg gratings [1].

A Gaussian function was fitted to the spectrum of each grating and the peak reflection was plotted in Fig. 2.8. This figure shows the normalised peak reflection for the gratings written at different fluences in GF4A and SMF28. The data points for GF4A fibre show a dip with a trough at 20 kJ/cm^2. This trough indicates the roll over point from *Type I* to *Type In* gratings, as the positive and negative index contributions compete and therefore the grating strength decreases. Based on this information, it can be assumed that *Type I* gratings are inscribed with fluences below, and *Type In* gratings are inscribed with fluences above this roll over point of 20 kJ/cm^2.

The hydrogen-loaded fibre SMF28, does not show a dip in Fig. 2.8. Fibres with the presence of hydrogen are classified into different types, known as *Type IH* and *Type IHp* gratings and they do not show the characteristic roll over [2].

To confirm the classification of gratings, the fibres were placed in a furnace to undergo heat treatment as the different grating types vary in their thermal resilience [50]. From literature it is known that *Type I* and *Type IH* gratings are less resilient to high temperatures than their high fluence opponents *Type In* and *Type IHp*. Low fluence gratings are expected to be erased at temperatures lower than 320 °C, whereas the high fluence gratings can withstand temperatures up to 500-800 °C [2]

Both fibres were thermally treated in a furnace (Seven Thermal Solutions CU2006) one at a time. An argon gas purge was introduced 30 min prior to the thermal ramp up to create an inert environment inside the furnace. The temperature was ramped up at the maximum ramp rate of 5 °C/min to 850°C for the GF4A fibre, and to 750°C for the SMF28 fibre. The temperature was monitored with a thermocouple during the duration of the experiment. To capture the reflection spectrum, a broadband super luminescent source (Amonics ASLD-CWDM-5B-FA) and an optical spectrum analyzer (ANDO AQ6317B) was used.

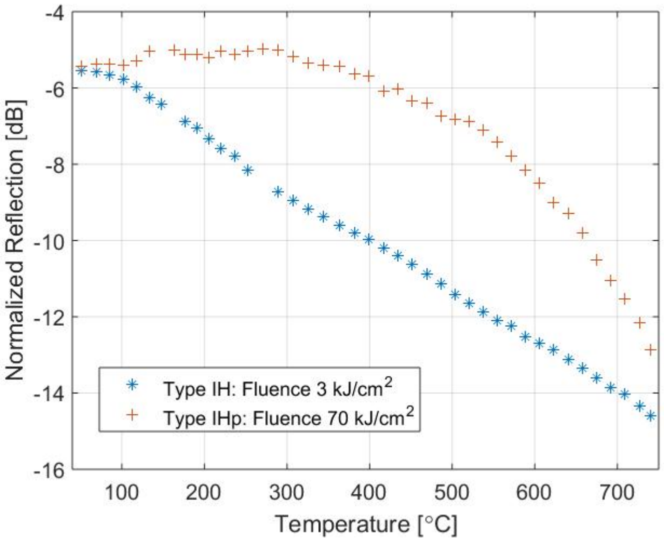

FIGURE 2.11: Peak over time during thermal treatment of SMF28 fibre Bragg gratings [1].

The reflection spectrum of one of the single Gaussian apodised gratings is displayed in Fig. 2.9 in GF4A and SMF28. A Gaussian function was fitted to each of the grating spectrum and the peak over temperature was plotted for three different fluences in GF4A (see Fig. 2.10). This graph shows the distinct thermal behaviour for each grating type in GF4A: The blue, starred graph shows the thermal behaviour of the low fluence grating (10 kJ/cm^2). The reflection starts to decrease at around 250 °C, reaching its minimum at 600 °C. This characteristic allows the grating to be classified as *Type I* grating.

The yellow, circled graph shows the behaviour of a high fluence grating to high temperature. The grating was written with a fluence of 40 kJ/cm^2 and is therefore expected to have a high thermal resilience as the grating will have been formed by densification of the glass. The peak reflection of this grating is stable up to a temperature of 650 °C, when the grating abruptly weakens. This is characteristic for a *Type In* grating response.

Arguably the most interesting grating out of the three is the red, crossed graph written with a fluence of 20 kJ/cm^2. This weak grating started with a reflection 10 dB (15 dB) lower than the *Type I* (*Type In*) grating. Surprisingly, with an increase in temperature, the grating reflection does not drop, but increase, reaching a high at 580 °C, after which the reflection decreases again. The explanation for this behaviour goes back to the competing positive and negative index that formed this ”roll over” grating. At the beginning, both positive and negative index were present, resulting in a competing overall index and hence low reflection. With increasing temperature however, the less thermal resilient *Type I* grating slowly anneals out, allowing the negative index grating (*Type In*) to become present. The grating reflection slowly increases as the positive index slowly erases with temperature.

All three gratings types result in a regeneration at high temperatures. Literature suggests that there appears to be a permanent change in the glass structure, to allow even a *Type I* grating to be visible after annealing [2]. It is believed that these gratings result from thermal quenching and internal stresses, but the complete processes involved are yet to be fully understood.

The fluence curve (Fig. 2.8) of the hydrogenated fibre, SMF28 does not show a distinct feature, which would allow a classification of different grating types at room temperature. Fig. 2.11 shows the thermal response of two gratings written with 3kJ/cm^2 and 70kJ/cm^2. This figure shows again two distinct thermal behaviours with the high fluence grating showing a thermal resilience up to 350 °C, wheras the low fluence grating already decaying at 100 °C. This thermal behaviour classifies the two gratings in the *Type IH* for the low-fluence grating and *Type IHp* for the high-fluence grating.

With the thermal processing, it was possible to characterise and classify gratings written with the SSDUW technique for the first time. For GF4A, this conclusion could have been drawn from the reflection spectrum at room temperature (Fig. 2.8), however, a prediction of grating types for SMF28 would not have been possible.

2.4.3 Spatial Co-location

2.4.3.1 Superimposed and Superstructured Gratings

The aim of this project is to store calibration data in form of Bragg gratings in a fibre or on a chip. As a rule of thumb, the data storage capacity increases with a higher number of Bragg gratings inscribed. To increase the grating density, multiple gratings can be inscribed at the same physical location, so on top of each other. This is called spatial co-location and depending on the technique used also known as superimposed gratings or superstructured gratings.

Superimposed gratings are gratings that are written consecutively on top of each other. It is therefore a simple, serial writing technique for co-located gratings. Superstructured gratings on the other hand are written at once, by using a predefined refractive index pattern. The desired refractive index pattern is designed based on the desired gratings and transferred to the fibre in one writing step, making this technique a parallel writing process.

Both superstructured and superimposed gratings have been around for a long time. They were first mentioned in the same year as the first fibre Bragg grating was reported, in 1978 [57]. In their paper, Kawasaki et al. mentioned that co-located gratings could be fabricated by exposing the fibre with different wavelengths either consecutively for superimposed or simultaneously for superstructured gratings.

Co-located gratings have not been fabricated with SSDUW before. It was therefore important to fabricate gratings with both techniques and compare the results particularly in regards to relative writing precision, or in other words: is the final relative Bragg wavelength where they are expected to be? To answer this question, a set of 45 gratings with a length of 200 mm have been superimposed into photosensitive polarisation maintaining fibre (PS-PM980) with a fluence of 1 kJ/cm^2 and a spectral separation of 4 nm. Writing such a large number of long gratings into the fibre and taking a wide range spectral scan after each new grating formation took in total approximately 9 hours. This limited the amount of gratings that could be inscribed to 45. A further concern was the choice of spectral separation, which led to the requirement for a wider bandwidth. The gratings which were inscribed last typically can be found on the edges of the bandwidth. This is less ideal as per the fibre's specifications, the operating wavelength of PS-PM980 fibre is between 970 - 1550 nm. In addition to that, there is a limiting system component from the writing set up, as detuning from the central wavelength defined by the crossing angle of small spot direct UV writing system will cause the grating reflection to decrease. Due to all of these limitations, the number of gratings inscribed in this fibre was 45.

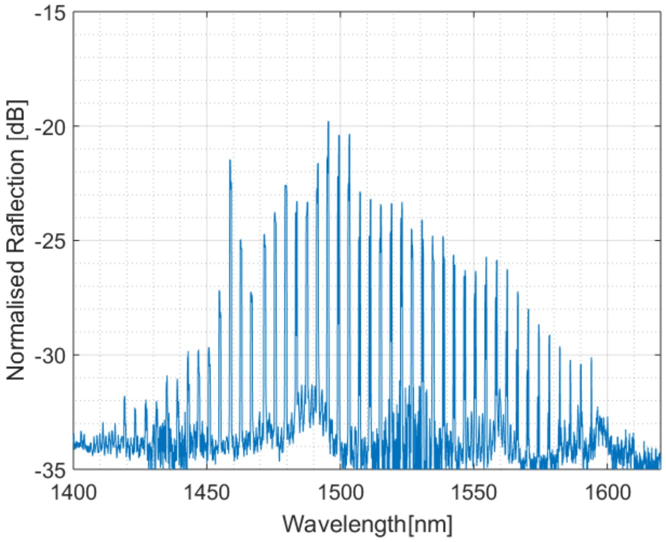

FIGURE 2.12: Superimposed fibre Bragg gratings written in photosensitive, polarization- maintaining fiber (PS-PM980) at the same physical location.

Fig. 2.12 shows the reflection spectrum of the superimposed gratings after all 45 gratings have been written. The envelope decreasing on either side is due to detuning, however, the grating at 1458 nm, which was written first, is almost double in reflection than compared to the neighbouring longer wavelength grating (written on the 9th superimposition) and three times the reflection of the neighbouring short wavelength grating (written on the 14th superposition). This implies that this first grating was able to maintain a higher refractive index contrast compared to subsequently written gratings. The first grating is not the only grating that displays a comparatively higher reflectivity; 1496 nm, 1500 nm, 1504 nm and 1480 nm are the grating wavelengths inscribed after the first grating. All three gratings show a higher reflectivity than the gratings on either side. It should be noted that the reflection of the grating at a wavelength of 1466 nm appears particularly low, because the interlock of the laser was accidentally tripped during this grating inscription.

Gratings written in a unexposed or scarcely exposed fibre appear to have a higher reflectivity compared to gratings written in an exposed fibre. This would imply that the material has finite availability to react to subsequent exposure. And therefore limits the formation of new colour centres that can contribute to grating reflectivity. Another explanation is that the glass is starting to densify due to the to the increased number of superposition and the resulting accumulated fluence that has been introduced into the fibre. It becomes increasingly difficult to continue densify the glass during further inscription and therefore the refractive index contrast of subsequent gratings becomes weaker. In order to find out if densification has taken place, and therefore a *Type In* grating has been inscribed, thermal processing was carried out. This is further described in Section 2.4.3.2.

An optical spectrum was taken after each inscription to monitor the evolution of the gratings with further inscription. The grating's index contrast n_{AC} is calculated with the following equation.

$$n_{AC} = \frac{\pi}{\lambda_B L} \text{arctanh} \left(\sqrt{r_{max}} \right), \tag{2.25}$$

with the Bragg wavelength λ, the grating length L and the peak reflection r_{max} [37]. The evolution of n_{AC} was plotted against accumulated fluence, which is shown in Fig. 2.13. This graph shows the rapid decrease in the index contrast with inscription of further gratings. As discussed in Section 2.2.4, there are two underlying processes for achieving a refractive index change through UV exposure: colour centres and densification. Initially, it can be assumed that colour centres will be easily formed, however, with further exposure, this effect will get depleted and and therefore the n_{AC} decreases. Then the second process, densification becomes evident. This densification is believed to take place at higher levels of UV exposure, even if delivered subsequently. As shown in Fig. 2.13 gratings that are inscribed after the first gratings (10th, 20th, 30th grating) still follow the index trend of the initial grating, indicating that the process is more dependant on material history than immediate effects caused by laser exposure. The effects on reflection and grating type for superimposed gratings is further discussed in Section 2.4.3.2, where GF4A was used.

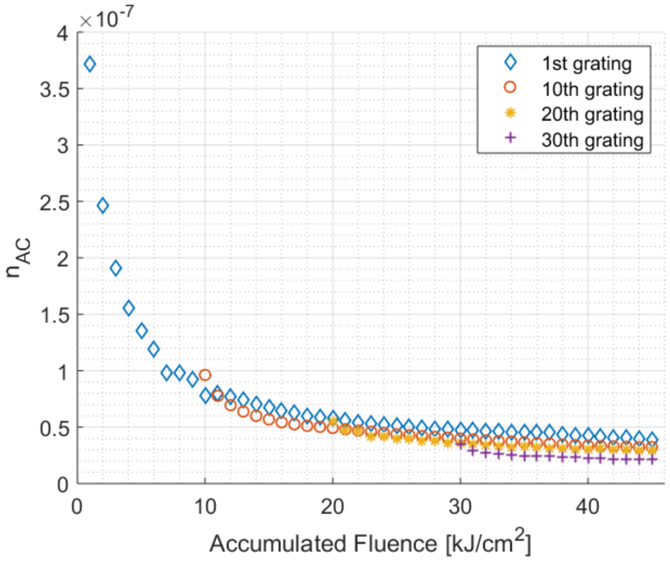

FIGURE 2.13: AC refractive index change vs accumulated fluence. This figure shows how the n_{AC} changes with further inscription of superimposed gratings. Four gratings have been selected to demonstrate the trend in n_{AC}

To fabricate superstructured gratings on the other hand, a refractive index profile is generated, aimed to mimic the superimposed gratings from Fig. 2.12. 44 gratings were designed, however the fluence was set to 20 kJ/cm^2 instead of 45 kJ/cm^2, which would be the total accumulated fluence of the 45 superimposed gratings written with an individual fluence of 1 kJ/cm^2. The reason why the lower value was chosen is because it was feared that a high fluence could erase all gratings due to thermal annealing by the slow-moving spot.

The spectrum of the superstructured gratings is shown in Fig. 2.14. It should be noted that the envelope of the superimposed gratings in Fig. 2.12 is centred at around 1500 nm, whereas the envelope of the superstructured gratings in Fig. 2.14 is centred at around 1550 nm. This is caused by slight variations in the angle of the crossing beams in the SSDUW set up due to alignment modification.

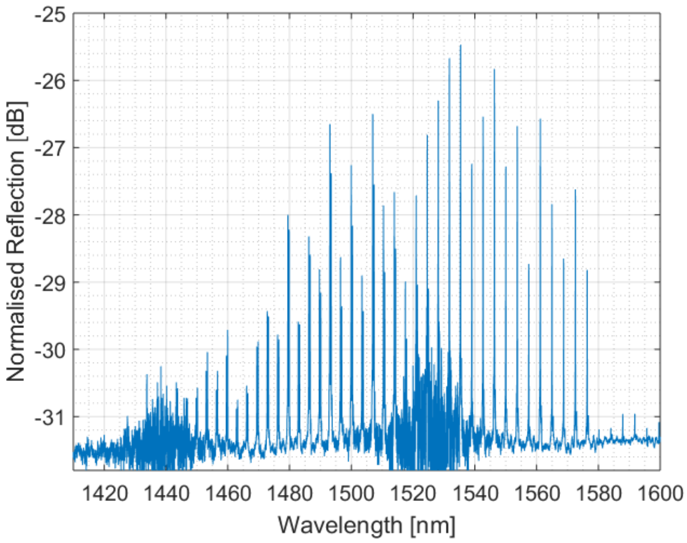

FIGURE 2.14: Optical reflection spectrum of superstructured gratings.

To analyse the difference between measured Bragg wavelength (”real wavelength”) and design wavelength, i.e. the precision of both techniques, both wavelengths were plotted against each other in Fig. 2.15. The black line indicates the ideal case, where the design wavelength and the real wavelength are matching. A deviation from this line therefore indicates an error in the initial assumption for the effective refractive index n_{eff}, which was used to calculate the Bragg wavelength according to Equation 2.18.

When comparing these techniques, it is important to not only focus on the outcome of the grating fabrication, but also the writing process itself. Superimposed gratings are written in series, so one after the other. This requires additional time, as the fibre rail has to be translated back to the starting position after each write. This step adds approximately 6 seconds for each grating, resulting in an excess of just under 4.5 minutes for inscribing 45 gratings with a length of 200 mm. Superstructured gratings do not require this additional writing time as they are fabricated in parallel, all at once.

Writing one gratings after the other has an effect on the reflectivity of the gratings, which will be discussed in more detail in the next section.

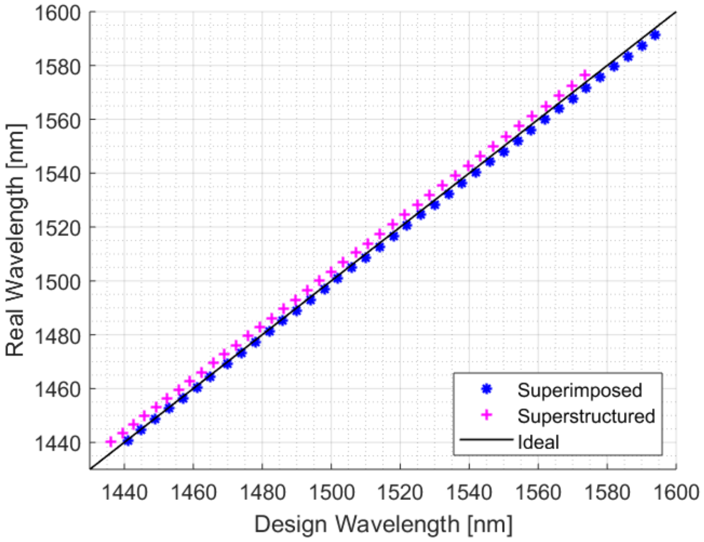

FIGURE 2.15: Real wavelength vs design wavelength to demonstrate the fabrication accuracy of superimposed and superstructured grating writing.

2.4.3.2 Thermal processing

To understand the processes in superimposed writing a bit better and to understand which grating types were fabricated, one of the fibres has been thermally treated in a furnace to evaluate their thermal response. With thermal processing, the grating type could be determined and it is therefore expected to reveal information on the impact that newly written gratings have on already existing gratings.

When superimposing gratings, it was noticed that for individual fluences above 0.5 kJ/cm^2, the reflection of already defined gratings dips. To investigate this effect further, three sets of 26 gratings were written into the same fibre (GF4A). This ensured that the gratings are fabricated under the same conditions, particularly in regards to laser power, lab environment and alignment. The gratings were each 5 mm long and each set was written 5 mm apart from each other as shown in Fig. 2.16. All three initial gratings were superimposed with 25 gratings of their respective fluence (either 0.5, 1 or 2 kJ/cm^2).

Fig. 2.17 shows the peak reflection of the initial three gratings with further inscription. At the beginning, the reflection of all gratings decreases rapidly, after which the reflection of gratings written with a fluence above 0.5 kJ/cm^2 rapidly increases again. This dip is similar to the roll over dip described in Section 2.4.2, where gratings written with a fluence of around 20 kJ/cm^2 are in the roll over state, where positive and negative refractive index compete, which results in a weak grating reflection. If the dip from superimposing gratings comes from the grating becoming a *Type In* grating, it would mean that in order to fabricate different grating types, the power does not have to be delivered at once, but can be accumulated over time.

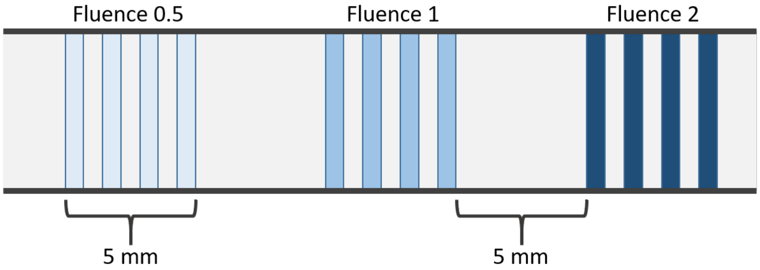

FIGURE 2.16: Schematic of the three sets of fibre Bragg gratings superimposed with 25 gratings of the same fluence. Each set of gratings was 0.5 mm long, with a separation of 5 mm to reduce the effect of potential alignment errors.

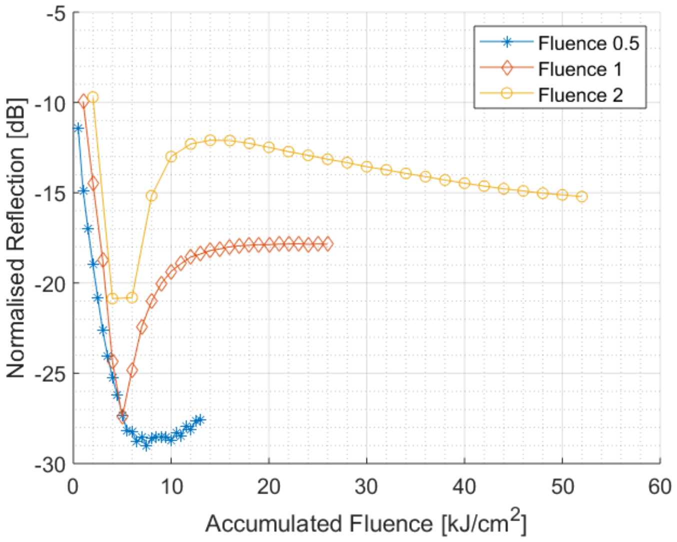

FIGURE 2.17: Comparison of superimposed grating inscription for different fluences written in the same fibre on the same day. The fluence of 0.5 kJ/cm^2 did not display a characteristic dip, which may be due to insufficient thermal treatment during the inscription process.

To investigate the grating type in superimposed writing, a fibre was fabricated with 24 superimposed gratings and a single grating on either side as shown in Fig. 2.18 a. Each grating was fabricated with a fluence of 5 kJ/cm^2. This means that the single gratings are expected to be a *Type I* grating and the first grating of the superimposed section experienced an accumulated fluence of 120 kJ/cm^2.

Fig. 2.18 b shows the peak reflection of each grating after each consecutive grating inscription. It should be noted that the reflection is only a relative representation. For an absolute value, the Fresnal back reflection of a cleaved fibre end, typically 4% is used as a reference and the measured reflection spectrum is normalised against this. In this case however, this reference measurement was not taken. The two flat lines with circles represent the two single gratings, which were written on either side of the superimposed gratings. The reflection of these gratings is expected to remain largely unchanged as

TABLE 2.2: Overview of chronological and spectral order of fibre Bragg gratings of Fig. 2.18

Spectral Order	Wavelength [nm]	Chronological Order
1	1450	1
2	1470	2
3	1475	7
4	1480	4
5	1485	8
6	1490	5
7	1495	9
8	1500	6
9	1505	10
10	1510	11
11	1515	12
12	1520	13
13	1525	14
14	1550	26
15	1555	25
16	1560	24
17	1565	23
18	1570	22
19	1575	21
20	1580	20
21	1585	19
22	1590	18
23	1595	17
24	1600	16
25	1605	15
26	1620	3

they have not experienced any superimposition. The first of the superimposed gratings shows again a rapid decrease of reflection, which reaches a trough at 20 kJ/cm^2. Similarly to Fig. 2.17, it is assumed that this is due to the onset of *Type In* gratings. Interestingly, gratings inscribed at a fluence above this threshold appear to have an initial low reflection, which increases with further inscription.

The optical spectrum of the fibre before the furnace run is shown in Fig. 2.18 c. The grating at 1450 nm and at 1620 nm are the single gratings and therefore appear stronger than the other gratings, which are superimposed. The chronological writing order is shown in Table 2.2. The set of gratings at shorter wavelength are written first, the set of gratings at longer wavelength written last. The weakest grating at around 1550 nm is the last grating written.

For the furnace run, the fibre was placed into a tube furnace (Seven Thermal Solutions CU2006) with an argon environment, which was introduced 20 minutes prior to start of the thermal treatment. The furnace was set up to ramp up to 800°C at 5 °C/min, plateau

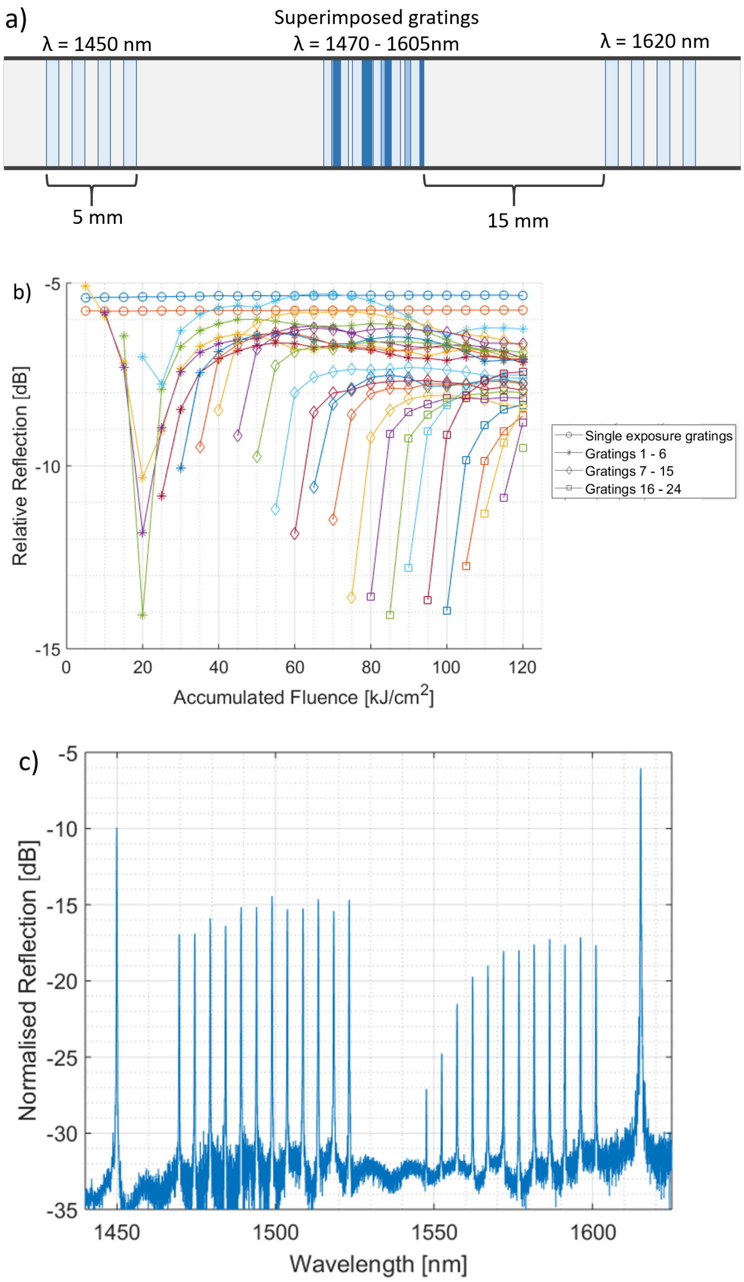

FIGURE 2.18: a) Schematic of the fibre with two single gratings on either side of a superimposed section. b) Peak reflection of each grating with further inscription. Blue and orange circled graph shows the outer single gratings. Each new line from left to write shows one grating that is added on top of the first one. Gratings 1-6 are marked with a star, gratings 7-15 with a diamond and gratings 16-24 with a circle. c) Normalised reflection spectrum of this fibre, taken a couple days after the inscription, before the annealing in the furnace.

for 30 minutes and ramp down at 5°C/min. A thermocouple was used to monitor the temperature in the chamber. After having executed the thermal treatment, it became clear that the temperature in the furnace only went up to 615°C. However, as seen in Fig. 2.10, this was a high enough temperature to allow classification of grating types.

Fig. 2.19 shows the peak reflection of the superimposed gratings. The teal line with the highest reflection shows the reflection of the first (single) grating over temperature. This line has a similar trend to the *Type I* grating in Fig. 2.10, as it starts to decay at around 200°C. The other gratings were superimposed gratings and the order in which they are written changes from bright teal to dark grey. The majority of these gratings do not respond to an increase in temperature up to around 500°C, where the reflection starts to decay. These gratings are more resilient to high temperatures and can therefore be classified as *Type In* gratings. The last grating the black grating with the lowest reflection. This grating was the only superimposed grating that did not have another grating superimposed on top. The reflection starts about 12 dB lower than the first superimposed grating. With temperature, the grating strength decreases further until in increases again at around 250°C. At around 500°C, the reflection reaches its peak and starts to decreases from there. This grating shows similar trend to the roll over grating in Fig. 2.10. The initial competing positive and negative refractive index are annealed out at different temperatures, leaving the more thermally resilient grating type (*Type In*) at high temperatures. These results mean that the superimposed gratings are resilient to high temperatures as long as further gratings are superimposed.

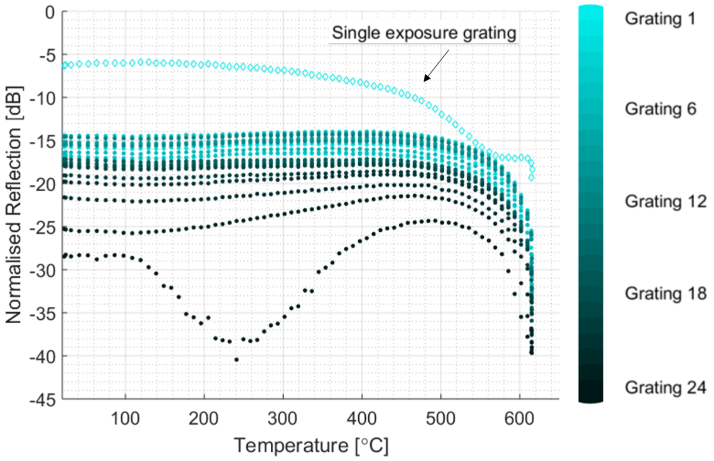

FIGURE 2.19: Peak reflection of the superimposed gratings with increasing temperature. The 1^{st} grating (bright teal), which is the single, non-superimposed grating does show similar behaviour to *Type I* gratings, whereas the other gratings show *Type In* behaviour. The last grating written, the grating in black shows the typical roll over characteristic with the grating strength decreasing starting at a temperature of 100°C. The competing positive refractive index starts to anneal out at 250°C and the *Type In* grating reaches its maximal reflection strength at approximately 500°.

Fig. 2.18b indicates that gratings written after the roll over region (after an acculated fluence of 20 kJ/cm^2) increase the reflectivity with further superimposed gratings.

Therefore, in order to achieve strong *Type In* gratings, additional gratings should be superimposed. These gratings can be superimposed out of band to not interfere with desired data.

Fig. 2.20a shows the normalised peak reflection of 40 superimposed gratings in black with the data points as stars. Gratings were inscribed at the same location in a wavelength range between 1450 and 1530 nm with a fluence of 1 kJ/cm^2 and a length of 5 mm. A Gaussian distribution was fitted to each individual grating and the peak reflection was extracted. The errorbars represent the confidence interval based on the fit. The gratings were inscribed with increasing wavelength. Looking at the black, starred graph in Fig. 2.20a, it becomes clear that the reflectivity is relatively low for short wavelengths, which were the gratings inscribed first. The reflectivity increases for longer wavelengths, reaching the highest reflectivity for the grating at 1490 nm. Gratings inscribed at wavelengths larger than 1490 nm then decrease again in strength. The low reflectivity for short wavelength is due to detuning; the low reflectivity for longer wavelengths however is due to a different phenomena. The longer wavelength gratings were inscribed last. As shown in Fig. 2.18b, gratings after the roll over region are initially weak and gain strength with further inscription.

To show the effect that further inscription has on the already defined gratings, more gratings were written on top of the already existing gratings. The effect is shown in Fig. 2.20a: the green, circled plot shows the reflectivities of the existing gratings, when an additional 20 gratings were inscribed (resulting in a total of 60 superimposed gratings). These 20 additional gratings are out-of-band at a larger wavelength than 1530 nm. The reflectivity of the first inscribed gratings (short wavelength gratings) decreased by approximately 2.15 dB. This was calculated for the first 21 gratings, which are the short wavelength gratings up to 1490 nm. For gratings larger than 1490 nm, the reflectivity increases, making the curve itself flatter compared to the black, starred line with no additional out-of-band gratings. The flatter curve means that a more even reflection distribution was achieved. For encoding, this can be important as equal reflectivity creates fewer errors in the read-out. This is because a threshold will define when a grating is accepted as a grating, and when it is too weak to be considered noise.

Further inscription of 20 out-of-band gratings, resulting in a total of 80 superimposed gratings (40 in-band gratings and 40 out-of-band gratings). This caused the reflectivity of all gratings to decrease by 2.25 dB compared to 60 superimposed gratings (40 in-band and 20 out-of-band gratings). For interrogation, a certain minimal reflectivity is required to be able to detect the grating and therefore the number of superimposed out-of-band gratings should be kept minimal to only increase the reflectivity of the last inscribed gratings, without decreasing other gratings. Fig. 2.20b shows the residuals in reflectivity with further inscription of out-of-band gratings. The reflection of the first grating that was inscribed into the fibre steadily decreases with each out-of-band gratings that is superimposed. The reflection of the last inscribed grating however

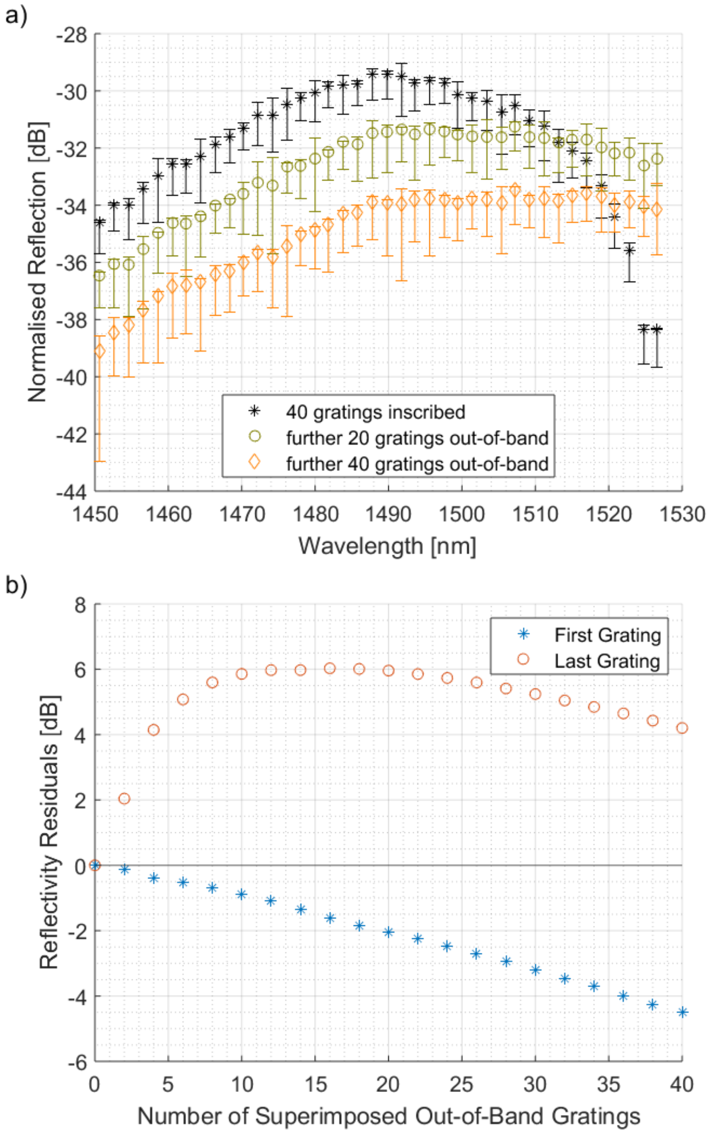

FIGURE 2.20: Evaluation of out-of-band grating inscription in GF4A to achieve a consistent overall reflection strength. Out-of-band gratings are written outside of the wavelength range of interest and serve the purpose of altering the spectral features of the gratings inside the wavelength range of interest. a) The black stars show the peak reflection after 40 superimposed gratings, the green circles after further 20 gratings were superimposed out-of-band, and the orange diamonds after a total of 40 gratings were superimposed out-of-band. b) Residuals of the first and last grating inscribed with superimposition of out-of-band gratings. The first grating decreases consistently in reflectivity, whereas the reflectivity of the last grating increases until 15 gratings have been superimposed. From that onward, the reflectivity also decreases. This figure shows that it can be beneficial to inscribe out-of-band gratings to increase the reflectivity of the gratings in the wavelength range of interest.

initially increases its reflectivity with further out-of-band gratings. After 15 out-of-band gratings, the reflectivity starts to decrease. This shows that there is an optimal amount of gratings to be superimposed to improve the reflectivity of final gratings without reducing the reflectivity of initial gratings.

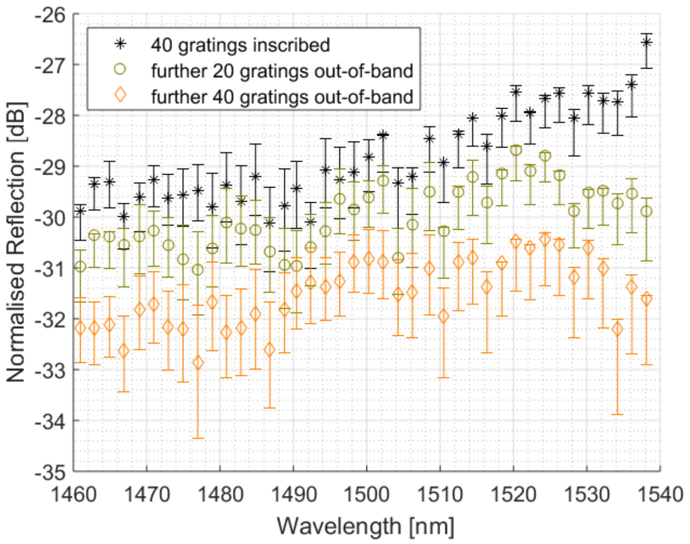

FIGURE 2.21: Evaluation of out-of-band grating inscription in PS-PM980 to achieve a consistent overall reflection strength. Out-of-band gratings are written outside of the wavelength range of interest and serve the purpose of altering the spectral features of the gratings inside the wavelength range of interest. The black stars show the peak reflection after 40 superimposed gratings, the green circles after further 20 gratings were superimposed out-of-band, and the orange diamonds after a total of 40 gratings were superimposed out-of-band.

Fig. 2.21 shows the PS-PM980 equivalent of Fig. 2.20, which was inscribed into GF4A. Comparing these two figures, one can see that the grating reflection after 40 superpositions does not decrease for PS-PM980. With further inscription of out of band gratings, the overall reflection decreases. This means that for PS-PM980, there is no benefit in inscribing further out-of band gratings.

The same gratings were inscribed in both fibres; 5 sets of gratings in total in each fibre. Fig. 2.22 shows the development of the first inscribed grating with further inscription of different amounts of superimpositions in a) PS-PM980 and b) GF4A. The gratings for both fibres were each 5 mm long and inscribed with an individual fluence of 1 kJ/cm^2. The gratings were written on the same day, to avoid any variation in alignment or environmental fluctuations. Five gratings were written into the first position of each fibre; after a gap of 40 mm 10 superimposed gratings were inscribed, after further 40 mm, 15 gratings and so on. It should be noted that a spectrum has been captured after each grating inscription for the set of 5, 10 and 15 gratings. For the set of 20 superimposed gratings, a spectrum was captured after every other inscription and for the set of 30 gratings after every third inscription.

Fig. 2.22 a and b show a distinct difference between those two fibre types with superimposing: The gratings in PS-PM980 steadily decrease with further inscription, whereas gratings inscribed in GF4A initially decrease, but after the roll-over section increase again. They reach their highest reflectivity at an accumulated fluence just over

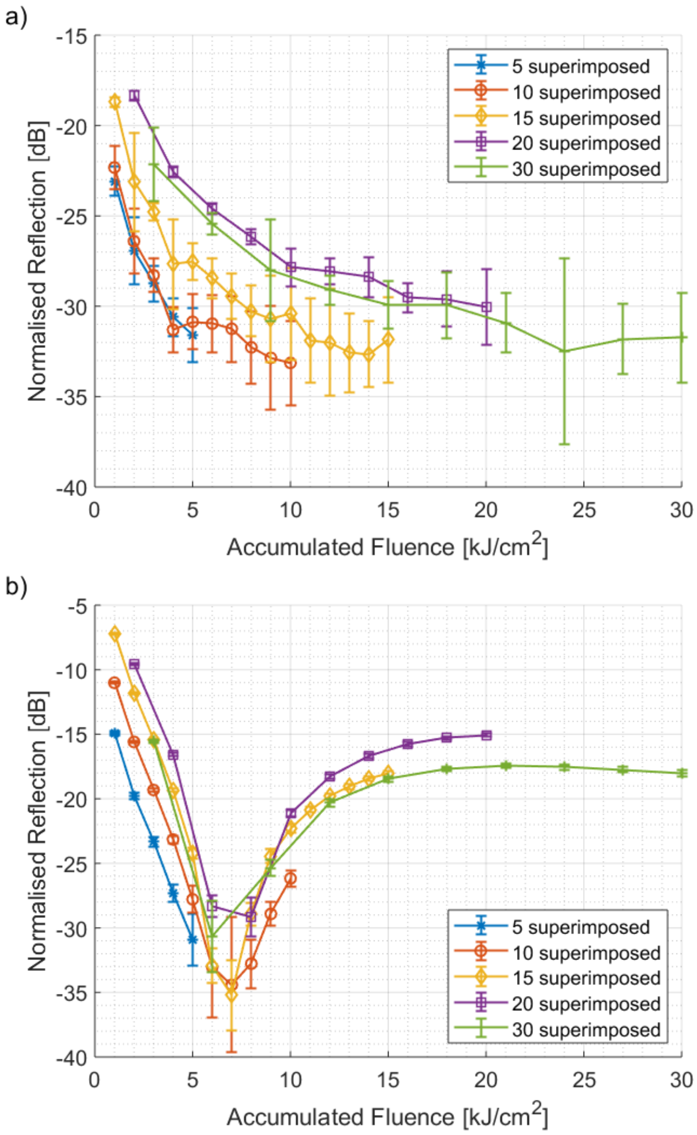

FIGURE 2.22: Comparison of the amplitude behaviour from the first grating with subsequent 5, 10, 15, 20 and 30 superimpositions in a) PSPM-980 and b) GF4A. Each data set represents a new fibre location and the initial vertical offset observed is an artefact of different alignments.

20 k/cm^2. The first grating of the set in GF4A reduces its reflectivity by 69% after 19 gratings have been superimposed whereas the reflectivity of the equivalent grating in PS-PM980 dropped by 95%. This comparison indicates that GF4A is better suited for inscribing multiple gratings on top of each other, even though inscribing out-of-band gratings may be required.

2.4.4 Multicore Fibre

Increasing the grating density is essential for the EROS project. Superimposing in a single core was explored in Section 2.4.3. One option to achieve a higher grating density is using multicore fibre instead of single core fibre. Multicore fibre have, as the name suggests multiple cores in one strand of fibre. Here, we therefore investigate addressing individual cores of a multicore fibre during FBG fabrication.

Different methods to inscribe fibre Bragg gratings into multicore fibre are schematically shown in Fig. 2.23: a) Phase mask, b) Femtosecond point-by-point, c) SSDUW. Phase masks are widely used for fibre Bragg grating fabrication, particularly for high volume fabrication [56]. The first inscription of fibre Bragg gratings into a multicore fibre was carried out with a phase mask in a hydrogenated four-core fibre in 2003 by Flockhart et al. [58]. In their work, all cores were exposed simultaneously, as the wide exposure does not allow focusing into one core only. This results in the same Bragg wavelength inscription in all cores. However, since the cores are located at different positions, the alignment was not ideal, which resulted in significant variation in the grating spectra. In 2014, Lindley et al. inserted a seven core fibre into a flat top capillary to allow reduce aberations caused by the cylindrical fibre and therewith improve the grating spectra [59].

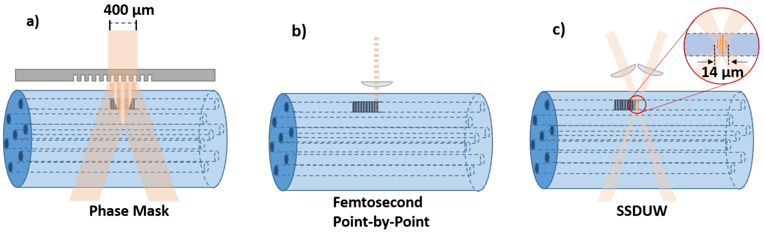

FIGURE 2.23: Different inscription techniques of multicore fibre.

For some applications, it can be beneficial to inscribe different Bragg wavelengths into individual cores. For encoding, for example where each core would contain a different set of information. Since phase mask inscription exposes all cores, a more selective inscription technique is required. Femtosecond point-by-point writing allows such selectivity. Donko et al. inscribed gratings into four cores of a seven core fibre [60]. This technique does not require hydrogen loading and neither does the fibre's coating need to be removed. These gratings generally are attributed to the accumulation of phase errors and micro-voids in the material, which typically introduces higher losses than phase mask gratings [61].

The SSDUW technique sits in the middle of the aforementioned techniques as it has a small spot, which allows a selective inscription into individual cores, and the technique utilizes UV to create a refractive index change, which allows the fabrication of low loss gratings [51].

Fibercore Ltd. provided a seven core fibre with a core diameter of 5 μm and a core spacing of 34.5 μm. In order to enhance the photosensitivity, the fibre was hydrogen loaded at 120 bar for 14 days prior to writing. The fibre coating was removed and clamped with a tension of 0.5 N onto the fibre rail, a rail that holds the fibre in place

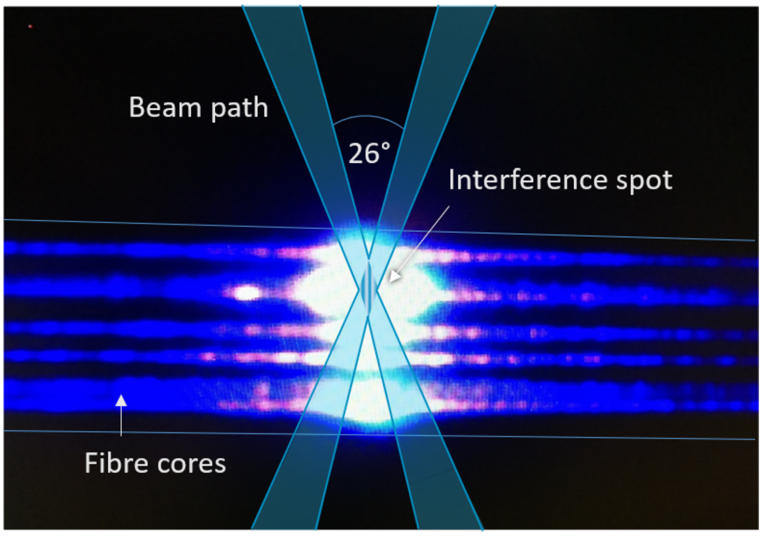

FIGURE 2.24: Side view of the seven core fibre during inscription, showing a schematic of the two crossing beams. The fibre cores are fluorescing due to the exposure.

during the inscription and is mounted on the nanometer precision air bearing stage, see Fig. 2.5.

Grating sets of 6 gratings with a length of 7 mm were written into five different cores. Hydrogen out-diffusion limited the available time for aligning and writing [43]. The output power of the laser was measured before each set and the average power was 27 mW with a fluence of 10 kJ/cm^2. The 14 μm writing spot was focused into one core, however as shown in Fig. 2.24, the other cores were also illuminated. Initially, the fibre was moved horizontally and vertically to align the laser spot into the different cores. Each set of gratings was inscribed on consecutive locations as shown in Fig. 2.25a.

A broadband super luminescent light source (Amonics ASLD-CWDM-5BFA)was connected to a 7-to-1 fan-out and an optical spectrum analyser to interrogate the gratings in the different cores. The spectra of all seven cores are shown in Fig. 2.25. This spectrum exhibits overlapped sections; when for example the spectrum of the purple core, core number 4 was connected, grating reflections at around 1400 nm and between 1450 and 1475 nm were visible along with the intended gratings between 1500-1530 nm. There are two different causes for this. Grating reflection that appear in multicore fibre unintentionally could be either due to cross-exposure, so the undesired exposure of a core during writing or due to cross-talk, which is the light coupling in to neighbouring cores, making it look as if there was a grating inscribed into this core, whereas the reflection actually arises from light of a different core coupling into the core of interest. Those two effects may be separated through bending as bending will cause cores to experience different strain subject to their position. Straining a core causes the spectral response of the Bragg grating to shift. If the optical response of all Bragg gratings in one core shift by the same amount, it can be assumed that the Bragg gratings are written into the same core. If however some gratings' respond with a different shift, it can be assumed

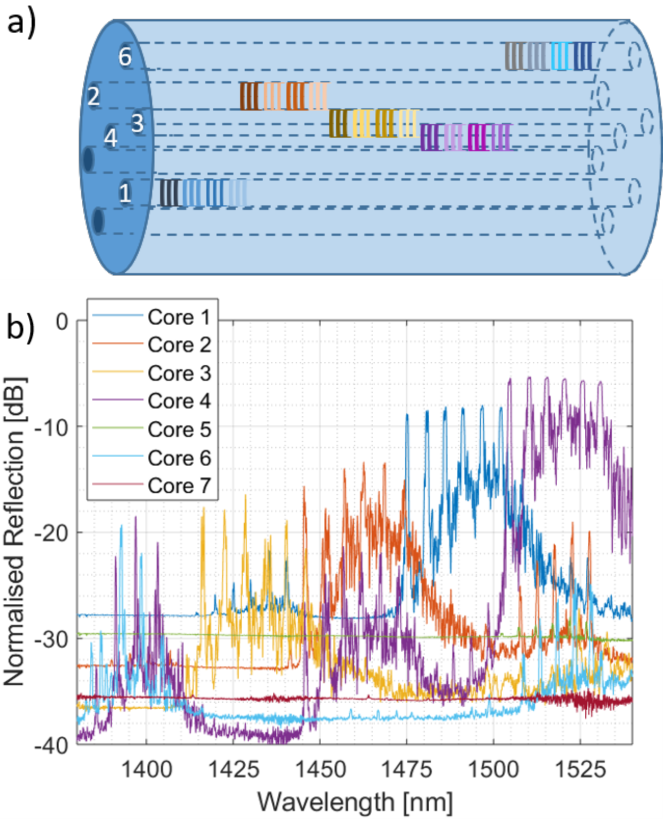

FIGURE 2.25: a) Schematic of grating inscription in five cores. b) Optical reflection spectrum of each core.

that the back reflected light from a different core was coupled into the interrogation core.

To investigate the fibre's response to bending, the fibre was bent around a cylinder with 25.4 ± 0.5 mm in diameter. The Bragg gratings will spectrally shift due to the strain that they experience. The axial strain ϵ_n of the nth core can be calculated with

$$\epsilon_n = 0.78 \frac{\Delta\lambda_{Bn}}{\lambda_{Bn}}, \tag{2.26}$$

where $\Delta\lambda_{Bn}$ is the shift of the Bragg wavelength λ_{Bn} caused by strain [51].

The optical spectrum was taken using the same set up as mentioned above. Fig. 2.26 shows the reflection spectrum for the five cores, into which fibre Bragg gratings were inscribed. It also shows a schematic of the core position in regard to the bending plane, which is marked with the black dashed line. The core position was determined by the amount and direction of the spectral shift after bending was introduced. In the figure, a spectral shift of 0.08 nm is observed. This small shift can be caused by the unavoidable axial straining of the fibre during wrapping the fibre around the cylinder. From the bending response it can be concluded that the spectral artefacts are caused

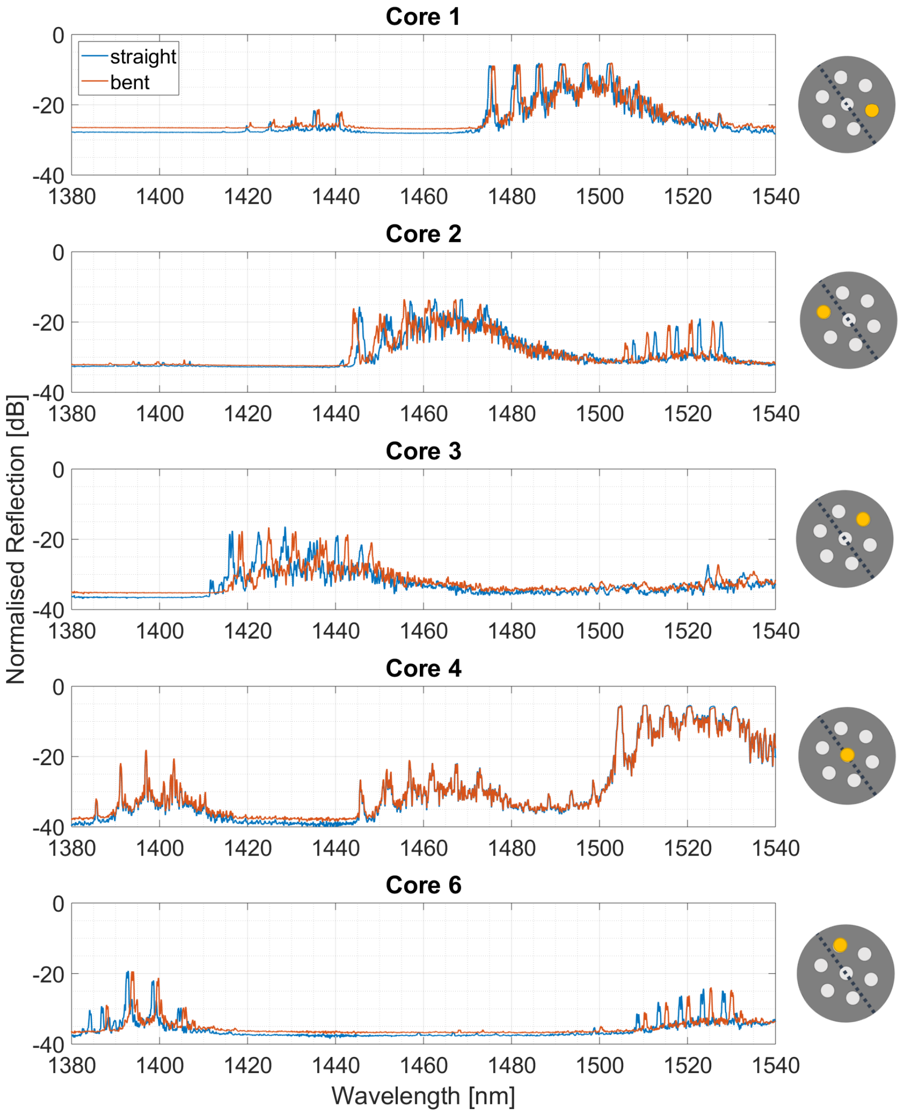

FIGURE 2.26: Spectral response of gratings in different cores to bending. The direction of the shift indicates if the core was stretched or compressed and the amount of shift indicates the core position in regard to the bending plane: the closer to the bending plane, the less stretching/compression the core experiences.

by cross-exposure rather than cross-talk, as all spectral features (grating responses and artefacts) in the same core shift by the same amount.

The artefacts in the optical spectrum are caused by cross-expose and in order to mitigate or eliminate these effects, a different writing technique was developed. Instead of moving the fibre horizontally and adjusting the height of the fibre to focus in the desired core, the fibre was clamped into rotatable fibre clamps. The fibre can then be rotated like a pistol barrel such that the desired core is located on the top position. By aligning the desired core to the top, the crossing beams are focused directly into the core without being distorted by neighbouring cores.

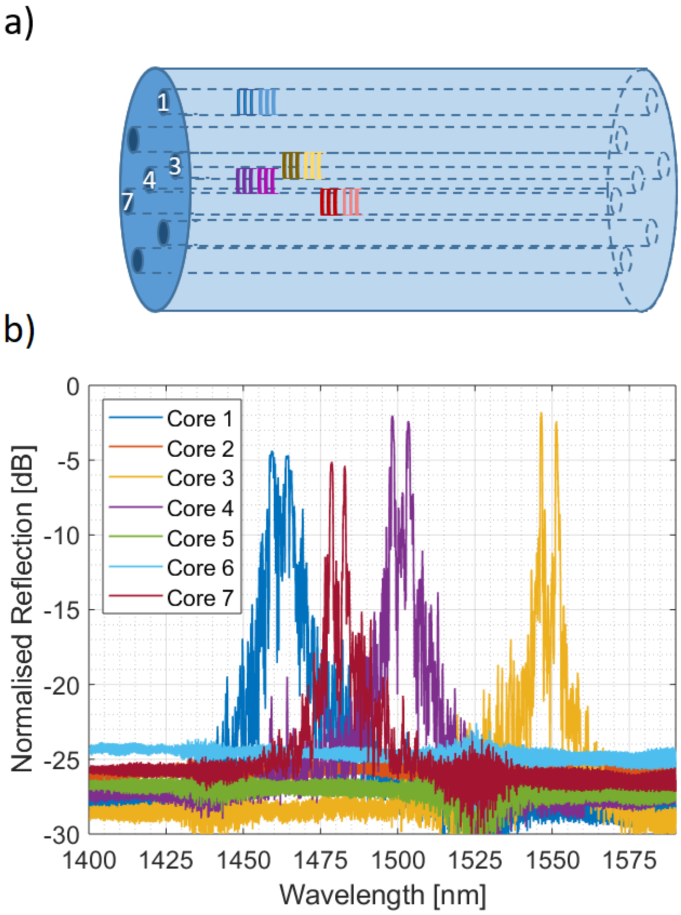

FIGURE 2.27: a) Schematic image indicating the grating position for writing with the new alignment method. b) Optical reflection spectrum of the multicore fibre written with the pistol barrel alignment method.

To test the pistol barrel aligning method, two 7 mm long Gaussian apodised gratings were inscribed into 4 cores at the same longitudinal position. Fig. 2.27 shows a schematic of the individual gratings as well as the final optical spectrum. The first two grating sets have been inscribed into Core 4 and Core 1 on the same longitudinal position, whereas the following grating sets were inscribed on different longitudinal positions in Core 7 and Core 3. The final optical spectrum displays some elements of cross-exposure in Core 4 from Core 1 and in Core 7 from Core 4. These effects are however reduced by 13 dB.

Fig. 2.28 shows the response to bending. Core 4 is the central core as it does not display any response to bending. Gratings that were written on opposite sides of the bending plane (Core 3 and Core 7) respond to bending with an opposing shift.

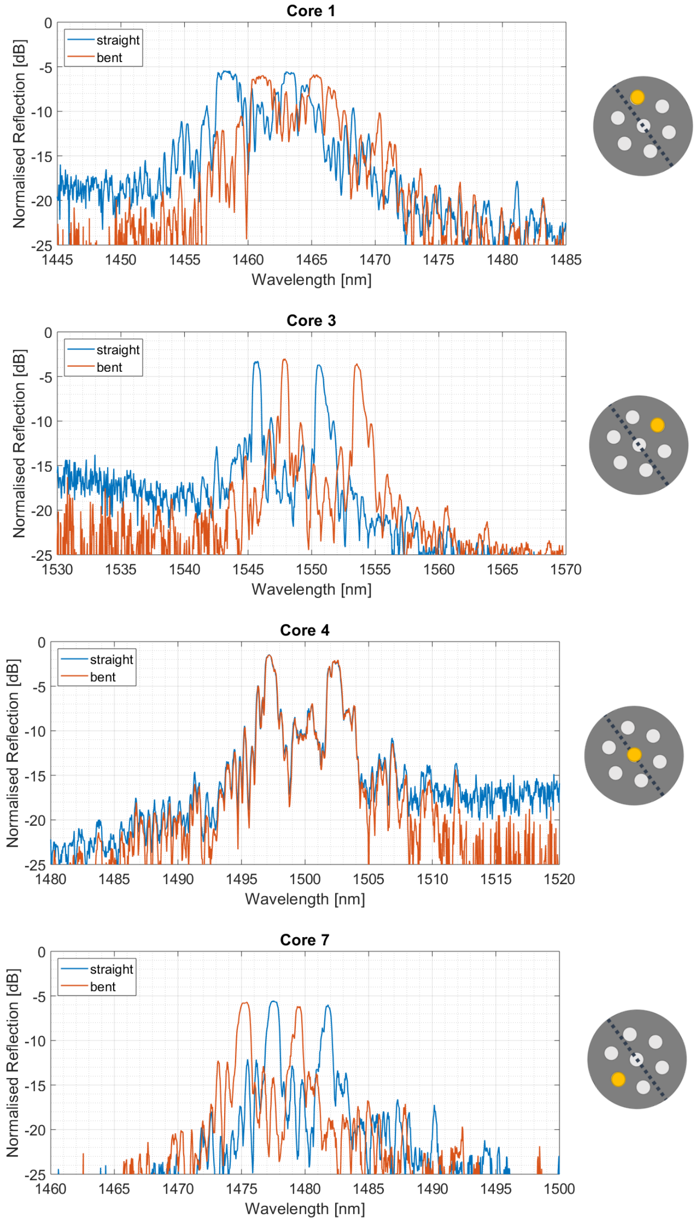

FIGURE 2.28: Response to bending for the four cores which FBGs were inscribed. The shift again gives an indication on the core location in relation to the bending plane.

A spectrum has been recorded after each set was written. Fig. 2.29 shows the wavelength shift of the first grating of each set with the inscription of further grating sets. The first set of gratings was inscribed into Core 4. The second set was inscribed into Core 1, at the same longitudinal position. The inscription of the second set of gratings cause the first set of gratings to shift by approximately 0.8 nm. This means that despite the cores being 34.5 μm apart, inscribing gratings on the same position does still exposes other cores. Inscribing gratings on a different longitudinal position does not affect gratings in other cores, as the gratings only shift by a maximum of 0.2 nm.

Inscribing gratings into multicore fibre was an interesting alternative to single core fibre

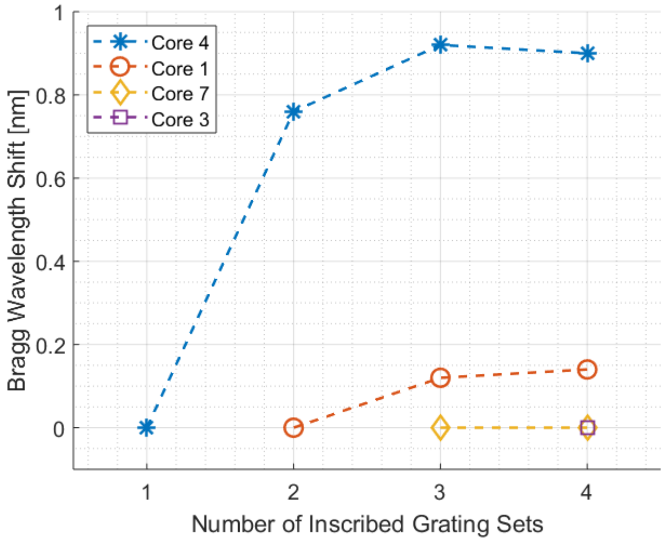

FIGURE 2.29: The wavelength shift with further gratings inscription. Gratings in core 4 and 1 were inscribed at the same longitudinal position, whereas core 7 and 3 were written on consecutive longitudinal locations.

and the benefit for applications such as sensing can be drawn easily. For data storage applications, however, superimposing gratings in single core fibres are more promising as more gratings can be inscribed on one longitudinal position (superimposing or superstructuring). There is also the greater difficulty in getting clean spectra due to cross-exposure, which adds additional risks to this fibre. In addition to this drawback, the use of multicore fibre requires a fan-out to interrogate individual cores, which is currently available at Thorlabs for £400-£500. Since the scope of EROS is to be implemented in commercial aircraft, the cost of each individual device is to be kept minimal. Alternatively, a 1x7 splitter could be used to couple all multicores into a single core, which could increase the co-locted gratings by a factor of seven. But this would come again to the risk of unclean grating spectra. Multicore writing will therefore not be further pursued within this project.

2.5 Conclusion

This chapter focused on the fabrication of Bragg gratings for an optical data storage. Thermal resilience is important for the application environment. Therefore a method to evaluate gratings written with the small spot direct UV writing technique was developed for the first time and different grating types have been classified through thermal processing. This allowed the definition of a suitable grating for the EROS project.

The main focus of EROS is to increase the grating density per location, which was explored by superimposing and superstructuring gratings in single core fibre or inscribing gratings into a multicore fibre. Two different fibres were taken into consideration:

the cladding mode suppressing photosensitive GF4A and the polarisation maintaining photosensitive fibre PS-PM980. GF4A showed better performance for superpositioning, since the grating reflectivity dropped less with superimposition compared to the gratings in PS-PM980. GF4A also has a price advantage as it costs only 2/3 of the price of PS-PM980 (prices viewed on Thorlabs on 24 February 2021).

Despite multicore fibre offer a great solution for various applications, due to the high cost in regard to their interrogation and the noisy optical spectrum, they have been found unsuitable for the EROS project. In addition to the higher cost, the grating density at one location was not sufficient for the project requirements and unintentional cross exposure either resulted in erroneous reflections or in weakening of the previously written gratings.

Chapter 3

Interrogation

3.1 Introduction

The second pillar in the development of an optical storage device is interrogation, or the read-out of the fabricated device. This chapter covers how the fabricated device can be read out. At a glance, the interrogation system seems like something that can almost be developed independently, as it only reads out the information already stored. But it is not. The interrogation system was the main driver for the inscription design of the EROS device. There are different ways to interrogate a fibre Bragg grating, two of them are explored in this chapter. The requirements for the spectral design of the storage device are different for each of them and therefore drives the roadmap to the final device.

The first and most logical step to read out Bragg gratings on a fibre is to read out the spectral information. This can either be done in transmission or reflection. Since the device will eventually be installed in an aircraft, where in terms of weight and cabling, less is more, the reflection measurement was prioritised as it requires less cabling: The interrogation system shall be placed in the avionics bay; the signal has to travel from the light source there to the calibration device (EROS), and then back to the sensor that measures the incoming light (in the avionics bay). For the reflection measurement, besides a splitter to divide the signals, there is only one long cable required to reach the position of the EROS device, as the reflected signal will travel back in the same cable. In transmission however, a separate cable is needed to allow the light to travel back to the sensor in the avionics bay. So for each device, two instead of just one fibre optic cable are required, which adds additional weight to the system. This was not the only reason why it was decide to implement EROS as reflection device. It is also because the sensors that EROS was intended to work with were based on reflection, so changing the EROS design to a transmission system would require a different set up, which also effects the sensor part.

With the type of response in place, the next question was how to implement the spectral interrogation. There are two ways to do this: either with scanning the light source (e.g. tunable laser) or with scanning the detector (e.g. optical spectrum analyser (OSA)). Which system to choose comes down to requirements defined by the industrial partner, which are based on experience in working with aircraft manufacturers, but also on specifications and standards required for commercial aerospace applications. As a rule of thumb, instruments and applications that are already approved for commercial aerospace are almost always favoured as the process of approving new equipment for flight is not only expensive, but also time consuming.

One of the most difficult parts is also the transitioning from a lab set up into an aerospace environment. Particularly challenging are typically the vibrations that equipment experiences during flight. Especially equipment that contains moving parts such as an optical spectrum analyser, can be expected to experience issues in such environments. Of course there is equipment specifically developed for such environment, but this is not always available. Therefore, the interrogation is focused on lab equipment to serve as proof of concept, which can be adjusted with instruments to fit the requirements for flight.

This chapter covers two different interrogation system, explains the working principle of the interrogation methods and demonstrates prototypes developed for the storage of data in a fibre in form of Bragg gratings. It closes with a recommendation for the implementation of EROS in the conclusion.

3.2 Background

3.2.1 Direct Spectral Interrogation

In the simplest case, the Bragg gratings are interrogated spectrally. Either with scanning the light source in combination with a intensity detector or with a broadband light source and a scanning detector (OSA). Fig. 3.1 shows an example of such a set up.

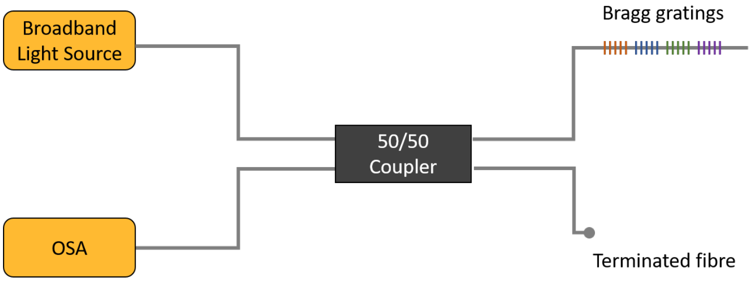

FIGURE 3.1: The spectral interrogation system: a broadband light source, a 50/50 coupler, an optical spectrum analyser (OSA) and the device under test, a fibre with inscribed fibre Bragg gratings.

With spectral interrogation, information can be encoded with respect to the spectral position of the gratings. In the simplest form, a binary system can be used, where the presence of a grating is defined as a 1 and the absence as a 0. Hence the maximum data capacity is given by the amount of gratings that can be written over the maximum wavelength range of the interrogating light source and detector.

The amount of gratings that can be interrogated in a certain length of fibre depends on the individual length of the gratings, their spectral bandwidth and the interrogation bandwidth: Consider for example the total fibre length to be 100 mm and each grating to be 10 mm long. In this case, only 10 gratings would fit into this section of fibre, consider they would be inscribed back-to-back. However, looking at the optical spectrum, if the spectral interrogation range was 10 nm, but the bandwidth of each grating is 2 nm, only 5 of those 10 gratings fit into the spectrum. There is a link between the grating length and the bandwidth, but unfortunately, this is not the way it would be beneficial to this project: The goal of this project is to fit as many gratings both spatially (= short grating length) and spectrally (= narrow spectral bandwidth) in a given piece of fibre. But as described in Section 2.2.3, the bandwidth gets narrower with an increased grating length for a length-limited grating regime. Each grating plane causes a broad band reflection, but with multiple planes a certain distance apart, these reflections interfere and therefore create a narrower spectral response.

Another limitation is the movement of the translation stages in the small spot direct UV writing set up. It is only possible to inscribe a fibre length of 250 mm at once. It could therefore be assumed that the grating length is the limiting factor for this interrogation method. Although fibre pieces can be stitched or retrospectively spliced together, only a single fibre length will be considered for the purpose of comparing the interrogation capacity. For a fibre length of 250 mm and a grating length of 5 mm, only 50 gratings can be inscribed back to back. But gratings can be superimposed, which means multiple gratings can be defined at one location, to the cost of peak reflectivity and bandwidth.

The total number of gratings that can be interrogated with spectral interrogation depend on: the source bandwidth, the grating bandwidth, the grating length and the length of the fibre. If the amount of gratings that fit spectrally in the source bandwidth is greater than the amount of gratings that spatially fit in the fibre length, it also depends on the ability to superimpose gratings.

3.2.2 Optical Frequency Domain Reflectometry

An alternative to spectral interrogation and an opportunity to increase the amount of gratings that can be interrogated, is optical frequency domain reflectometry, or OFDR. This technique allows to not only interrogate the spectral information, but also considers the spatial positioning of the Bragg gratings.

The set up of an OFDR system is shown in Fig. 3.2. It consists of a tunable laser and a photo-detector, which are connected via a 50/50 coupler to the device under test and a broadband reflector, which is ideally matched with the reflectivity of the gratings. The light of a tunable laser source gets reflected on the Bragg gratings in the test arm and the broadband reflector in the reference arm. Both signals interfere with each other in the detector arm and create an interference pattern. This interference pattern not only contains the Gaussian grating envelope of the Bragg grating reflection, but also the relative position of the gratings to the broadband reflector in the form of interference fringes underneath the grating envelope. These high frequency components can be translated into spatial information with a Fourier transformation [62, 63, 64].

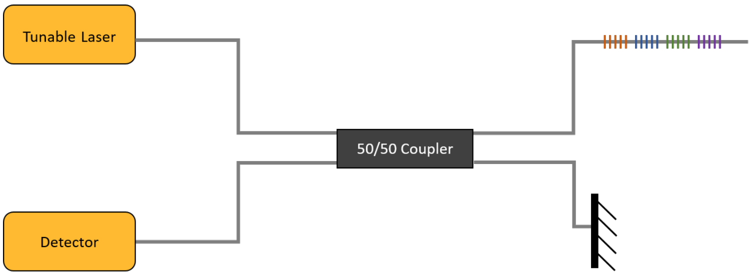

FIGURE 3.2: OFDR set up: Tunable laser source with fibre Bragg gratings in one arm and a broadband reflector on the reference arm. The detector detects the interference of the two reflected signals.

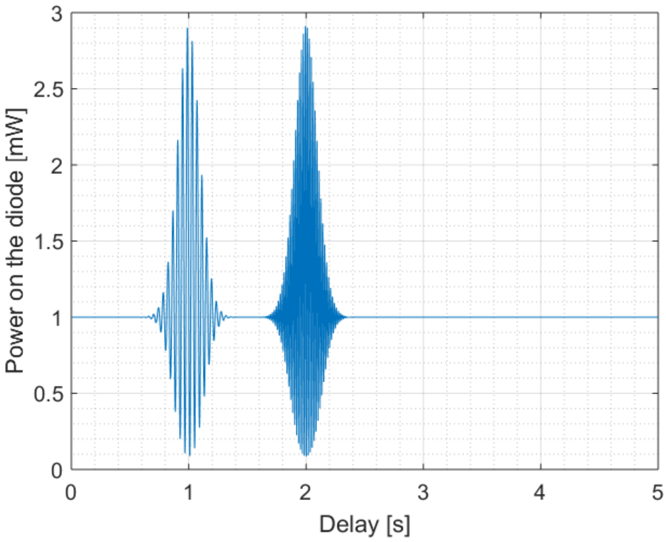

FIGURE 3.3: This plot shows two simulated Gaussian apodised gratings at wavelength $\lambda_A = 1530\,\text{nm}$ and $\lambda_B = 1540\,\text{nm}$. The two gratings are separated in time due to a scanning light source or a scanning detector. Their position along the x-axis will therefore indicate their wavelength, as the delay in the signal (1 s for the first and 2 s for the second gratings) are directly related to the scanning speed of the light source or the detector. Their position relative to the reflector is encoded in the fringes underneath the Gaussian envelope. The grating on the left (the grating with shorter wavelength) is closer to the reflector (d = 2 cm), whilst the grating on the right (longer wavelength) is located with a 3 cm relative path difference to the broadband reflector.

Fig. 3.3 shows the OFDR trace for a device under test with two gratings. The Bragg wavelength of the grating is transformed into a time offset, which defines the time when the reflection occurs in relation to the scan time. The spatial position of the grating relative to the broadband reflector is what defines the fringes underneath the grating envelope in the power spectrum. Fig. 3.3 shows the influence of the Bragg wavelength as well as an offset in spatial position. The two gratings appear with a time delay of 1 s from each other. This is due to the different Bragg wavelength: Since the light source is swept, the grating only reflects the light back to the detector when the laser wavelength matches the grating wavelength. For this simulation, the wavelength sweep was performed from 1520 - 1570 nm and it was assumed that the sweep takes 5 s. The first grating was written at $\lambda_B = 1530$ nm and the second grating at $\lambda_B = 1540$ nm. The 10 nm difference in wavelength then translates to a 1 s delay in time.

The fringe spacing in Fig. 3.3 are narrower for the second grating. This is due to the spatial position of the gratings relative to the broadband reflector. The reflection between the gratings and the broadband reflector can be seen as interference. The frequency of the fringes are defined with the equation for the free spectral range:

$$f = \frac{c}{2n_{\mathrm{eff}}L} \tag{3.1}$$

with the speed of light c, the refractive index n_{eff}, and the distance L between the reflectors [65]. The fringes of the second grating are narrower than the fringes for the first gratings, which means that the second reflector has a greater relative path difference to the broadband reflector than the first grating.

The time delay can be translated into frequency and by applying a Fourier transform, the frequency of the fringes will become evident, which indicate the spatial position of the Bragg gratings. Selecting a small spatial range by applying a windowing function in the spatial domain, for example over one Bragg grating, the spectral information can be retrieved by applying an inverse Fourier transform.

OFDR allows both the spectral and the spatial information to be read and therefore allows more information to be encoded. Spectral encoding only considers the optical spectrum and thus limits the amount of data that can be stored. OFDR on the other hand can be seen as a spectral interrogation at multiple points along the fibre and therefore increases this encoding capacity. Due to this potential of achieving higher storage capacity, it was chosen to continue with the experimental investigation of OFDR. This is described in the following section.

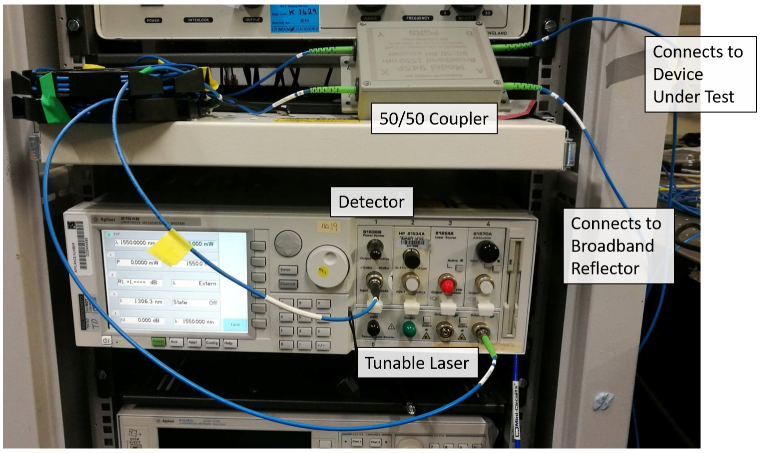

(a)

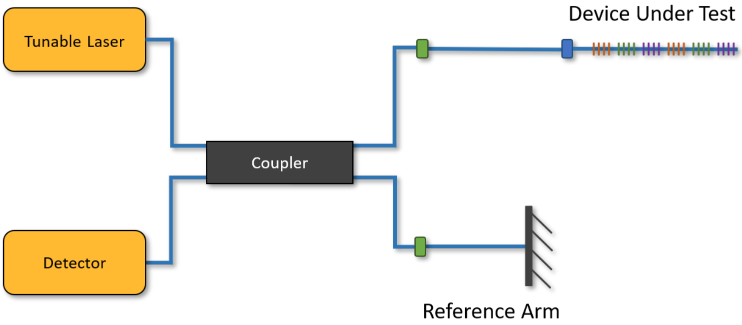

(b)

FIGURE 3.4: (a) Picture of the OFDR system consisting of a tunable laser, a detector and a 50/50 coupler, which connects to the device under test and the broadband reflector. (b) Layout of the experimental set up.

3.3 Experimental Results

The experimental set up of the OFDR system is shown in Fig. 3.4 a, and the schematic of the set up with a test fibre (Cyclops 35) is shown in Fig.3.4 b. The system contains of a tunable laser (Agilent 81600B), which has a wavelength range of 1440-1640 nm [66] and a detector (Agilent 81636B) with a wavelength range from 1250-1640 nm [67]. The system is set up with polarisation maintaining (PM) fibres and a PM 50/50 coupler. Two different broadband reflectors were used with this set up: a PM Retroreflector from Thorlabs with a reflectivity of 98% over an operating wavelength from 970-1550 nm [68], and the end facet of a PM flat cut fibre connector physical contact (FC/PC) with a reflectivity of 4%.

To investigate the capabilities of the OFDR system, a photosensitive PM fibre (PS-PM980) was inscribed with ten Bragg gratings. The gratings were defined with alternating Gaussian apodised and uniform refractive index profiles with the intention

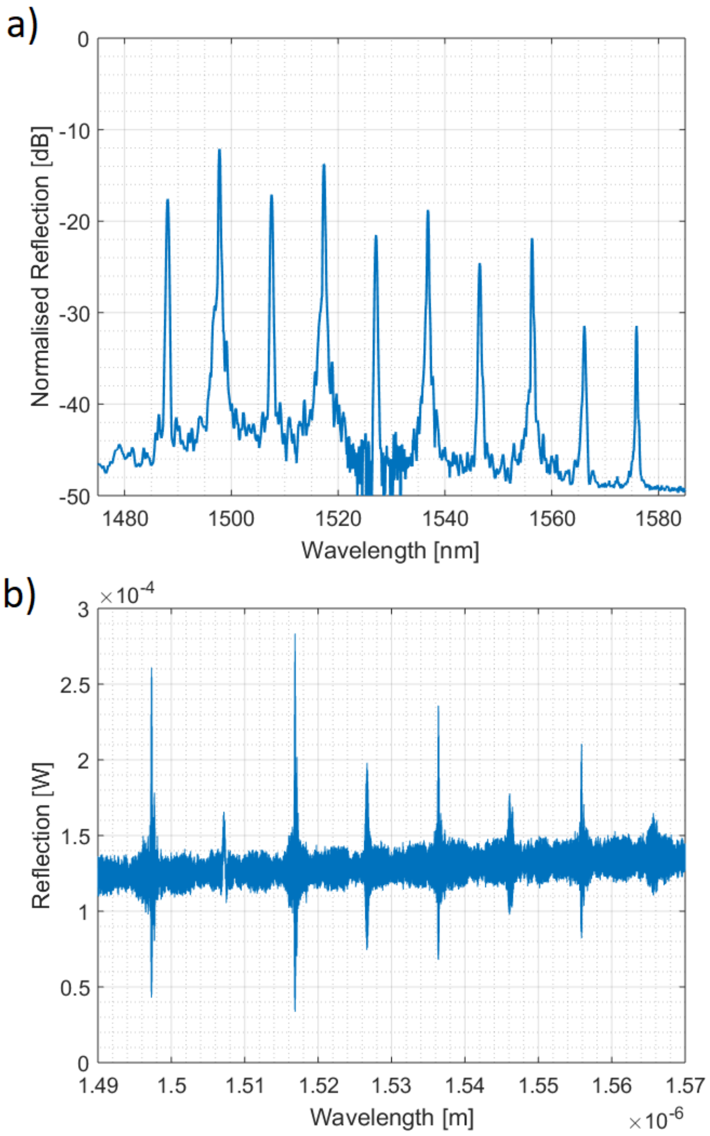

FIGURE 3.5: a) Reflection spectrum of the PS-PM980 fibre with ten alternating Gaussian apodised and uniform gratings. b) The raw OFDR trace shows the interference fringes resulting from the interference of the gratings with the broadband reflector.

to explore the possibility to make a distinction between grating apodisations. All gratings were 5 mm long, with a spatial distance of 15 mm and a spectral distance of 10 nm. They were all written at a fluence of 38 kJ/cm^2 to ensure high reflectivity (see Chapter 2, Fig. 2.7). A reflection spectrum, which was taken with an optical spectrum analyser (ANDO AQ6317B) is shown in Fig. 3.5a. The different apodisation profiles can be distinguished from the spectrum, as the Gaussian apodised gratings have sidelobe suppression.

Fig. 3.5b shows the raw OFDR trace which results from the interference of the gratings with the broadband reflector. As mentioned above, the interference fringes underneath the grating envelope are due to interference fringes, which are dependent on the distance of each grating relative to the broadband reflector. By Fourier transforming the trace, the spatial position of each grating becomes apparent and by applying a windowing function over the spatial position and applying an inverse Fourier transform, the spectral information of this specific spatial position is disclosed.

Fig. 3.6 a shows the spatial OFDR trace of the fibre in Fig. 3.5a. From the ten gratings in the fibre, only eight are inside the spectral range of this OFDR scan (1490-1570 nm). Fig. 3.6 a however, only displays six gratings. It should be noted that the first window (at 20 mm from the reference mirror in Fig. 3.6 a) results in two peaks in Fig. 3.6 b. These grating peaks (at 1497 and 1517 nm) are spectrally adjacent in Fig. 3.6 b, however the grating peak in between, at 1507 nm according to the optical spectrum in Fig. 3.5 a is missing. This example demonstrates the importance of a correct positioning of the reference mirror in relation to the grating array. The spatial grating position is shown as the relative distance to the reference mirror, regardless whether the path difference of the grating is larger or smaller relative to the reference mirror. Fig. 3.7 demonstrates this effect. In Fig. 3.7 a), the reflector is located at 90 cm, whereas all gratings are located at a longer distance. This results in the desired resolution of individual gratings as shown in the bottom of the figure. For scenario b however, the reflector is placed at 115 cm, which results in gratings 2 and 3 to have an absolute distance of 5 cm relative to the reflector. The same overlapping effect applies to gratings 1 and 4. This overlap or folding appears if the reflector is placed incorrectly relative to the grating position. In Fig. 3.8, the grating, which is located at a distance of 20 mm from the reference mirror appears more densely filled (high frequency components underneath the grating envelope) compared to the other gratings, which do not have a dense structure underneath the grating envelope. This is a feature that has been noticed with other samples, when the length of the reference mirror arm was chosen such that the reference was inside the grating array, rather than before the array. The gratings that occur before the reference mirror will still interfere with the mirror, but their grating curve will appear "filled" in the spatial domain. The missing grating in Fig. 3.6 b is due to an unfortunate positioning of the reference mirror. The reference mirror was placed in the equivalent arm between grating 1 and 3. The distance from the reference mirror to grating 2 was therefore so close zero, that it merges into the offset noise in the spatial domain. It is therefore important to adjust the length of the reference arm to be shorter than the distance between the coupler and the first grating of the array.

This grating array does not only highlight the importance of the correct placement of the fibre in relation to the reference arm but also helps to understand what additional encoding variables can be used. This array of gratings was composed with altering Gaussian apodised and uniform gratings. If these different structures can be identified in the OFDR traces, it creates another layer of encoding, since not only the grating being present can be encoded (0-1), but also the grating type (0-1-2). The 3 dB bandwidth of the three Gaussian apodised gratings in Fig. 3.6 b is 0.64 ± 0.16 nm and for the four uniform gratings it is 0.24 ± 0.04 nm. This suggests that a distinction between Gaussian

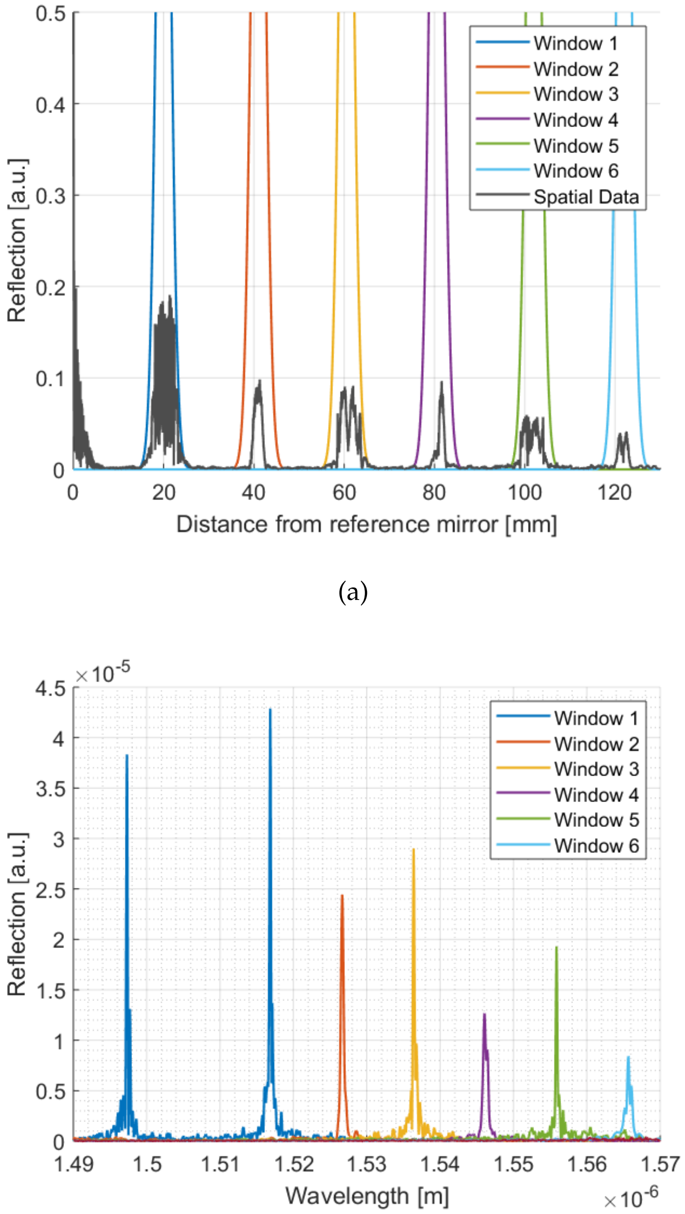

(b)

FIGURE 3.6: (a) Spatial OFDR trace of Cyclops 35, a fibre with alternating Gaussian apodised and uniform gratings. Each grating was superimposed with a windowing function to extract the spectral information by applying a Fourier transform. The windowing functions are normalised to 1 and therefore cut off from the plot. (b) Overlap of the results of Fourier transforming the spatial information from above. Each grating position (spatial information) corresponds to a spectral grating, although the first window covers two gratings. This is due to an undesired spatial offset between the broadband reflector and the grating array.

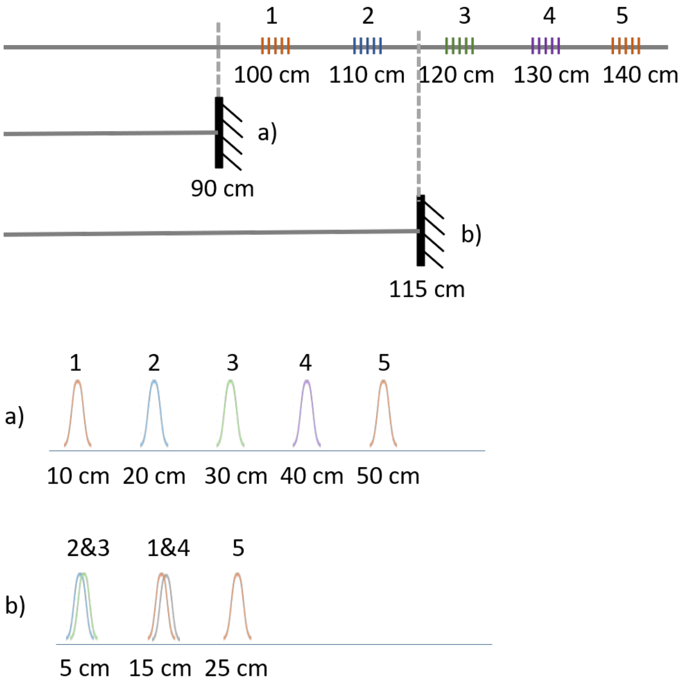

FIGURE 3.7: Two scenarios of the positioning of the reflector in the reference arm. a) Reflector mirror at position 90 cm, with the resulting spectral outcome on the bottom. b) Reflector at 115 cm results at the gratings being folded onto each other, as the absolute of the relative distance between grating and reflector is captured.

and uniform grating shape can be made in the OFDR trace and another encoding dimension could be implemented. Further work is suggested to explore the relationship of bandwidth between Gaussian and uniform gratings in the OFDR trace.

With this understanding, further experiments on grating features were conducted. Instead of changing the shape of the grating with an apodisation, a phase shift was attempted. A π-phase shift usually divides the grating in the middle into two and introduces a half-period phase shift between the halves. Figure 3.8 shows the two different types of phase shift that have been evaluated: a) shows a standard π-phase shift, whereas b) shows a 100 π-phase shift, which means that the planes were shifted by 100 half-periods. A 100 π-phase shift was chosen to investigate the detectability of a reflection dip in the spatial domain. An even number of π is not detectable in the spectral domain and a shift of 100 π was expected to be large enough to be visible in the spatial domain. Both figures show the spatial OFDR trace on the left and the spectral OFDR trace on the right. It can be seen, that the π-phase shift in figure a) is visible in both domains, whereas the shift in b) is only visible in the spatial, not in the spectral domain.

To investigate the 100 π-phase shift further, its location was changed in a following experiment. Instead of introducing the shift in the centre of the grating, it was placed a third into the grating. Figure 3.9 shows the spatial OFDR trace of a grating with the 100

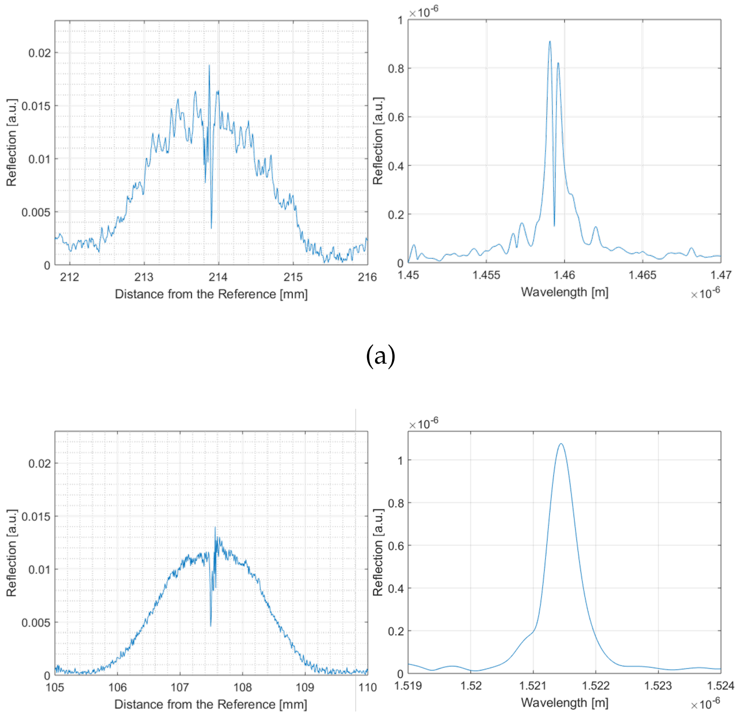

(a)

(b)

FIGURE 3.8: The spatial OFDR trace on the left side and the spectral OFDR trace, which results from windowing the spatial and Fourier transforming the signal back into the spectral domain. (a) This is for a grating with a π-phase shift in the middle of the grating. The phase shift is visible in the spatial and the spectral domain. (b) This is the OFDR trace of a 100 π phase shift grating. The characteristic dip in the middle of the grating is visible in the spatial domain, but not in the spectral domain.

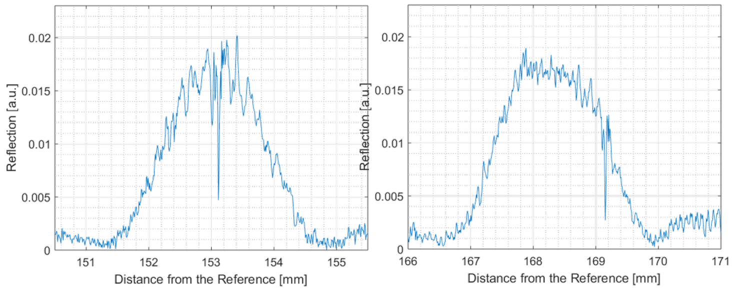

FIGURE 3.9: These are figures of further spatial OFDR traces of 100 π-phase shift gratings. It was chosen not to plot the spectral OFDR trace, as the dip was not visible in the spectral domain (as mentioned in Fig. 3.8). The figure on the left shows a 100-π phase shift grating with the dip in the middle, whereas the figure on the right has the dip shifted 1/3 to the end of the grating.

π-phase shift in the centre on the left and a grating with the 100 π-phase shift 1/3 of the way into the grating on the right. As mentioned above, this feature was not visible in the spectral domain and therefore the spectral OFDR trace is not shown.

For encoding, the additional features in the gratings allow additional layers of encoding. In the simplest way, the presence of a grating could be interpreted as a ″1″ and the absence of a grating as a ″0″. With the additional features however, encoding is not limited to the binary format anymore, which increases the number of data to be stored in the same length of fibre with the same amount of gratings.

3.3.1 Superimposed Gratings and Data Storage Prototyping

One limitation of the data storage is the available bandwidth of the tunable light source. To increase the data capacity of the optical storage without requiring a larger bandwidth, superimposed gratings were attempted. Instead of writing only one grating on one location, multiple gratings were co-located by either superimposing or superstructuring. This allows one spatial location to be seen as a single identity where the full laser bandwidth can be utilised for each position.

Another benefit of superimposing is that one grating can be used as a reference grating to counteract any spectral changes caused by environmental changes, for example local temperature variations. Bragg gratings spectrally shift with temperature and/or strain. By inscribing a reference grating on the same location as the data gratings, one grating could be used as the reference wavelength at the known wavelength λ_r. Any shift based on strain and/or temperature that this reference grating is experiencing is also experienced by all other gratings on this location. The environmental influences can therefore be subtracted from the data gratings with the information of the reference grating. With this technique, the gratings are insensitive to environmental changes and data can be stored and read out reliably. This however also reduces the amount of gratings available for data storage.

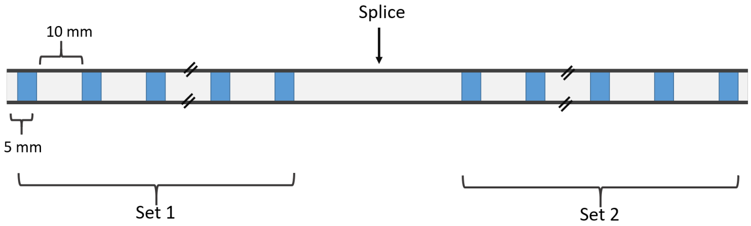

FIGURE 3.10: Schematic of the encoding prototype for calibration data encoding. Two separate fibres have been used which were then spliced together. The first fibre had gratings inscribed on 19 locations and the second one on 18.

For the first data storage prototype, two sets of fibre Bragg grating arrays were inscribed using the Small Spot Direct UV Writing technique. The inscribed gratings were

5 mm long with a 10 mm gap between each grating location. Each location contained 4 gratings. The first fibre set contained gratings on 19 positions and the second set contained gratings on 18 locations. The two grating sets were spliced together to create a single device of approximately 60 cm, which contained 37 grating locations. Each location represented one number from the calibration data file, which in total contains 37 numbers. For the prototype, the calibration data was shortened, as this was meant as a proof of concept. Instead of storing the full accuracy of the number (all decimal places), only an approximation was used and the signs were discarded to reduce the amount of superpositions and gratings required.

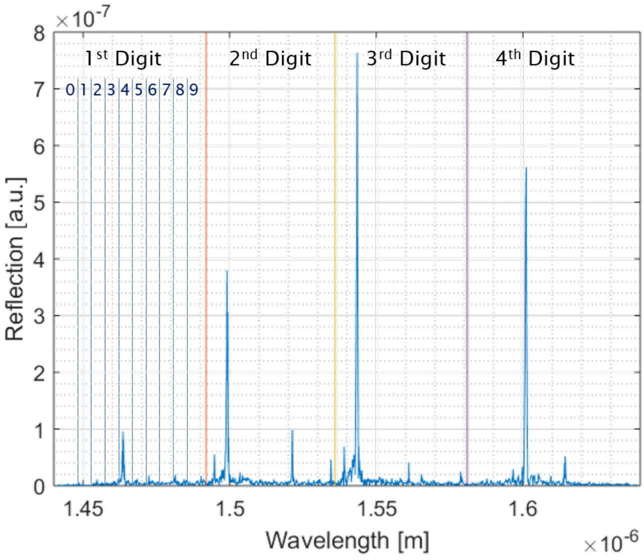

FIGURE 3.11: For the first prototype, the full spectrum was divided up into four sections, each representing one digit. Each section was then divided up again into ten subsection, each subsection representing the value of this digit.

On each location, four superimposed gratings were inscribed. The full spectrum was divided into four sections, which was again divided into 10 subsection to represent one digit. Each subsection contained one grating and the location of the grating defined the digit. This means that one single location was able to represent four digits. This decimal encoding is presented in Fig. 3.11. This prototype was a proof of concept to encode calibration data with OFDR and allowed to investigate this technique further.

Fig. 3.12 shows the spatial OFDR trace of the prototype. The array was connected backwards, such that after fibre set 1 and 2 were spliced together, fibre set 2 was spliced to the connector. Therefore fibre set 2 is spatially closer to the reference arm and is the first set to be hit by the incoming light. The gap due to the splice is clearly visible in this trace. Fibre set 1 appears to have stronger background noise compared to fibre set 2, which makes it difficult to locate the gratings. It is thus surprising that despite the noise, the interrogation accuracy of fibre set 1 is approximately 30% higher compared to set 2. The reason for the high inaccuracy in this set is again due to poor positioning of the reflector arm. If one carefully counts the number of peaks in fibre set 1, one will

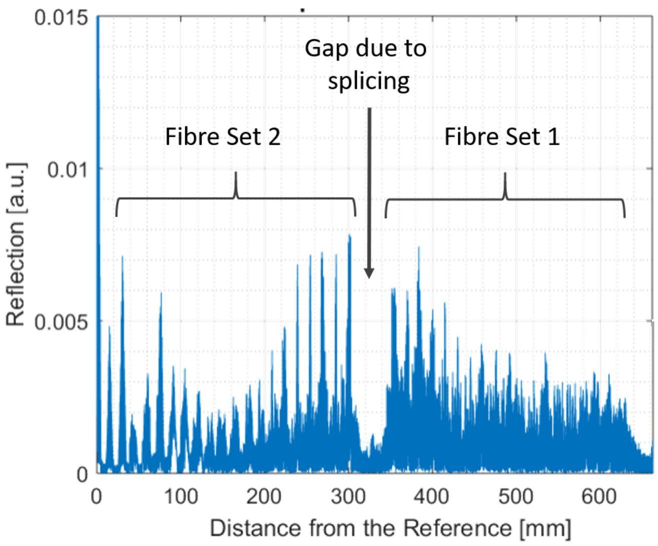

FIGURE 3.12: Spatial OFDR track of encoding prototype for calibration data encoding. Two separate fibres were used which were then spliced together. The first fibre had gratings inscribed on 19 locations and the second one on 18. Index gel was applied to the end of the fibre in order to prevent back reflections from the cleaved fibre end.

realise that there are 20 rather than 18 peaks, which given the proximity to the reference arm (first peak at 15 mm) suggests that a part of the grating array was spatially folded onto each other, just as described in Fig. 3.6.

Fig. 3.13 gives an overview of the correctly identified gratings for each set in green and the incorrectly identified gratings in red. The gratings at the bottom of fibre set two are gratings with the smallest distance from the reference arm, while gratings on the top are the ones furthest away. This reinforces the hypothesis that some gratings are folded onto each other which results in an incorrect classification. By the time this grating was fabricated and analysed, the effect of gratings spatially folding over was not known and therefore initially an error during the grating inscription was assumed. Only later, after analysing less complicated grating structures, it was found that it is beneficial to increase the delta between the reference mirror and the grating array to ensure that no gratings were reflected onto the wrong location. Further prototypes have taken this into consideration as it will be shown in the following paragraphs.

Instead of storing numerical data in a fibre, alphanumerical data was stored in the second prototype. Since Parker Aerospace, the industrial supporter of this project, is an American company, the most logical alphanumerical data to be encoded for a prototype was the Declaration of Independence. Changing the data type for the second prototype turned out to advance the data storing technique as the data format was changed from a decimal to a binary. Since this chapter refers to the interrogation, the encoding scheme will only be explained on a high level and the reader is referred to the Chapter Encoding for a detailed explanation of the encoding scheme.

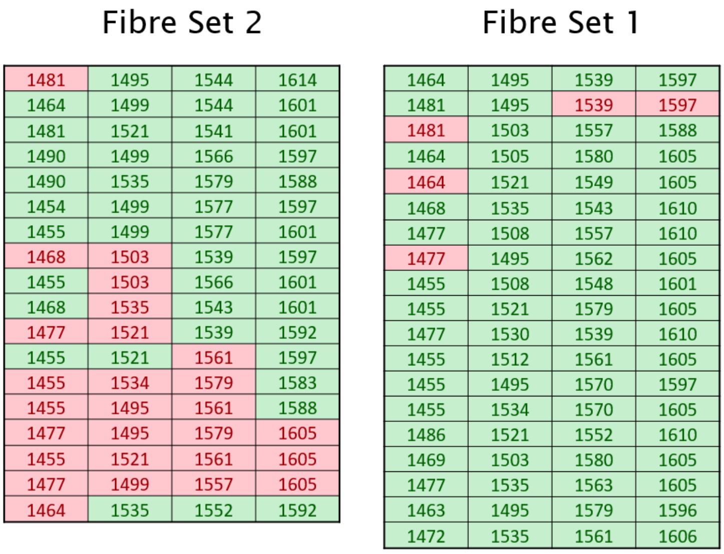

Fibre Set 2

1481	1495	1544	1614
1464	1499	1544	1601
1481	1521	1541	1601
1490	1499	1566	1597
1490	1535	1579	1588
1454	1499	1577	1597
1455	1499	1577	1601
1468	1503	1539	1597
1455	1503	1566	1601
1468	1535	1543	1601
1477	1521	1539	1592
1455	1521	1561	1597
1455	1534	1579	1583
1455	1495	1561	1588
1477	1495	1579	1605
1455	1521	1561	1605
1477	1499	1557	1605
1464	1535	1552	1592

Fibre Set 1

1464	1495	1539	1597
1481	1495	1539	1597
1481	1503	1557	1588
1464	1505	1580	1605
1464	1521	1549	1605
1468	1535	1543	1610
1477	1508	1557	1610
1477	1495	1562	1605
1455	1508	1548	1601
1455	1521	1579	1605
1477	1530	1539	1610
1455	1512	1561	1605
1455	1495	1570	1597
1455	1534	1570	1605
1486	1521	1552	1610
1469	1503	1580	1605
1477	1535	1563	1605
1463	1495	1579	1596
1472	1535	1561	1606

FIGURE 3.13: The interrogation of this prototype shows that most error occur in fibre set 2, which is at a shorter offset distance to the reference arm. A potential root cause for the high error rate in fibre set 2 is the folding phenomena, which was shown in Fig. 3.6 as the gratings appeared very close to zero-offset to the broadband reflector.

Two prototype fibres with the encoded Declaration of Independence were fabricated. Cyclops 75 had three superimposed gratings on each location and Cyclops 77 had four superimposed gratings on each location, but instead of all gratings carrying data information, an additional fifth superimposed grating was written at a constant wavelength and used as a thermal reference. All gratings were 4 mm long with a spatial separation of 5 mm between each location and a spectral separation of 1 nm between the gratings at a wavelength range from 1510-1580 nm.

In this encoding scheme, the spectrum was again divided up into spectral bins, where the presence of a grating would be considered a binary ”1” and the absence of a grating a binary ”0”. However, due to the fixed number of superpositions per location (three for Cyclops 75 and five for Cyclops 77) boundary conditions had to be defined such that in the length of the spectrum, only three (five) binary ”1” were allowed. Despite this is a binary system, numbers cannot be represented in the typical binary way. This means that in the above mentioned wavelength range, 70 spectral bins were available, but only three (five) binary ”1” (e.g. gratings) could be placed. The read out of the gratings was based on amplitude, such that the three (five) highest amplitudes defined the location of the ”1”s.

Fig. 3.14 a shows the spatial OFDR trace of Cyclops 75. It can be clearly seen that the gratings are spatially well separated, which allows accurate windowing without including neighbouring signals. Therefore, it is expected that the gratings in the spectral domain will be defined clearly, without too much noise. Fig. 3.14 b shows the spectral trace of one single location. Here it can be seen that the three superimposed gratings are well defined without other gratings being present. The notable decrease in amplitude

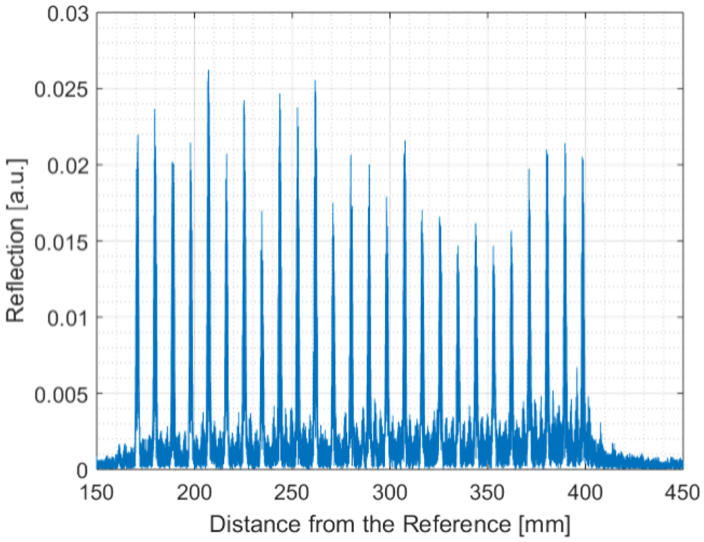

(a)

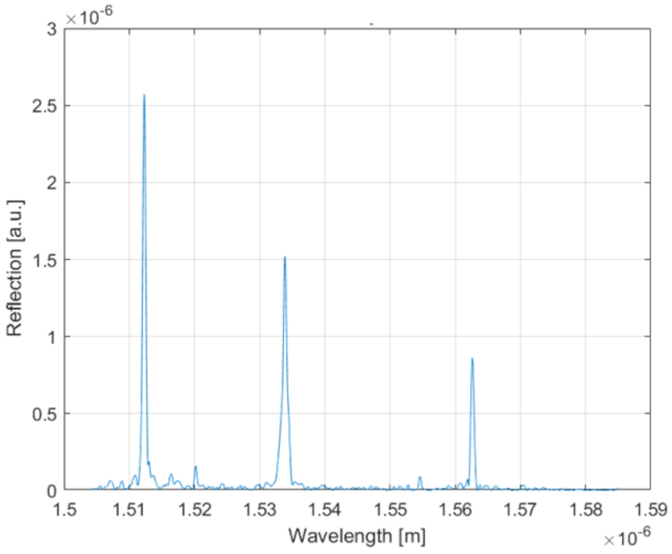

(b)

FIGURE 3.14: a)The spatial OFDR trace of Cyclops 75, a prototype encoding fibre with parts of the Declaration of Independence inscribed. Each peak is a location on the fibre, where a superposition of 3 gratings have been inscribed. b)After windowing one peak and applying the Fourier transform, the spectral information is revealed.

from short to long wavelengths is caused by the inscription order of the superimposing gratings: The short wavelengths were inscribed first and the long wavelengths last. The reader is referred to Section 2.4.3 for more details on superimposed gratings and the effect on amplitude. Overall, there were 26 locations inscribed in this fibre prototype with 3 gratings on each location. All of these 78 gratings were read out correctly.

For the follow up prototype, Cyclops 77 the number of superpositions was increased form three to five, including a reference grating, which allows to offset any thermal changes. A grating with a fixed wavelength of 1505 nm was inscribed on top of all locations and the read out before and after thermal referencing was analysed. The data was taken at room temperature without induced local temperature changes along the fibre. In one case, the data was read out and a nominal-actual comparison was carried out. In this case the thermal referencing was not used. In the other case, the difference between the designed reference gratings and the actual reference grating was calculated and this value was subtracted from the gratings of the same location. The performance of both with and without using the thermal referencing led to 94% of the gratings to be read out correctly. In other words, there was no performance difference for the thermal referencing. For larger and more localised changes in temperature, it can be assumed that this thermal referencing becomes more applicable. Fig. 3.15 gives an overview of the two fibres, into which parts of the Declaration of Independence was inscribed. More text was stored in Cyclops 77, due to an additional superimposed data grating, whereas Cyclops 75 was read out without any errors.

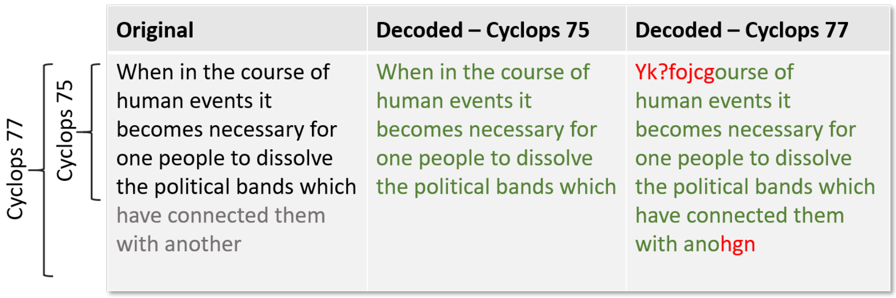

Original	Decoded – Cyclops 75	Decoded – Cyclops 77
When in the course of human events it becomes necessary for one people to dissolve the political bands which have connected them with another	When in the course of human events it becomes necessary for one people to dissolve the political bands which	Yk?fojcgourse of human events it becomes necessary for one people to dissolve the political bands which have connected them with anohgn

FIGURE 3.15: This overview shows the original encoded part of the Declaration of Independence on the left and the decoded text for each prototype in the respective column. Only three superimposed data gratings were used for Cyclops 75. This fibre contained less text, but was read out correctly. For Cyclops 77 four data gratings were used and an additional reference grating was inscribed. The additional grating allowed more data to be stored, but some errors occurred during read out.

An alternative to inscribing a reference grating is to ensure a spectrally large bin, to ensure any spectral drift due to strain or temperature will not result in an overlap of gratings in the spectrum. This however comes at a cost, as larger spectral bins mean that a lower number of combinations to place the grating in the spectrum, which results in a lower number of data that can be stored. Equally, there is a limit in how many gratings can be superimposed. This trade off will be further explored in Chapter 4.

3.4 Conclusion

This chapter focused on interrogation, the reading of the data stored in the fibre. Interrogation can be seen as the final step; reading out what has already been written (Fabrication), in a language that has already been defined (Encoding). Nevertheless, this is the central of the pillars, the second pillar out of three. And this is due to its importance in regards to the device design and its influence on fabrication. As described above, the interrogation system was the main driver in developing superimposed gratings and without developing the interrogation system first, it would not have been possible to store that much data in the device.

The focus of this chapter was on two interrogation systems: exclusively spectral as well as the combination of spectral and spatial interrogation. Spectral interrogation was briefly explained but due to the bandwidth limitations in the requirements, it was not further pursued. Instead, all efforts were set towards an OFDR system, where it was possible to zoom in on each spatial location on the fibre to run a spectral scan. In that way, OFDR can be seen as spectral interrogations on multiple different locations. Each new location can use the whole bandwidth of the interrogation system, which increases the amount of data that can be stored in the device.

There are however also drawbacks in using an OFDR system, such as the necessity to ensure a path difference between the reflector arm and the grating array in the device under test arm. If there is no path difference or a negative path difference (broadband reflector is placed in the location relative to the middle of the grating array), the part of the array that is closer to the coupler is folded spatially onto the part further from the coupler. This hinders a correct association of the spatial position and therefore induces errors in the read out. Another potential issue could be vibration. Preliminary studies have been performed in order to investigate the effect of vibrations on OFDR measurements, which indicate that the spectral signature broadens in a vibrating environment, however, more research needs to be done to understand and quantify the problem.

To allow an enhancement of the binary system, where the presence of a grating is considered a "1" and the absence of a grating is considered a "0", additional grating shapes and features were studied. A successful differentiation between Gaussian apodised and uniform gratings in the spectral domain was made, by examining the 3-dB bandwidth of the gratings. In addition, further gratings structures were examined. Different phase shifts were introduced, which created destructive interference at a small section of the grating. This was then visible as an intensity dip in the spatial OFDR trace. It was possible to change the location of the dip for a 100 π-phase shift grating from the centre of the grating to 2/3 (1/3) to the grating such that the intensity drop appeared at the beginning (or the end) of the grating. This dip was not visible in the spectral domain. A *pi*-phase shift however was resolvable in the spectral domain and hence added another layer to the encoding possibility. The grating shapes and features upgraded the system from a two layer system (grating being present or absent) to a 6 layer system:

- First layer: Gaussian grating
- Second layer: Uniform grating
- Third layer: π-phase shift gratings: visible in spatial and spectral domain
- Fourth layer: 100 π-phase shift gratings: visible in spatial domain only
- Fifth layer: 100 π-phase shift gratings with shifted dip at 1/3: visible in spatial domain only
- Sixth layer: 100 π-phase shift gratings with shifted dip at 2/3: visible in spatial domain only

The following chapter will focus on the encoding and hence explore how much data can be stored in the fibre, with the different shapes and features taken into account.

Chapter 4

Encoding

4.1 Introduction

After having covered the first two pillars: the writing of Bragg gratings in a fibre and then using them to store information; and the system that is required to read this information, we will now focus on one of the most important aspects of data storage. How to get from numbers in a spreadsheet to information that can be stored in a fibre.

There are many ways on how to go about finding an answer to that question and with many commercial optical storage devices already developed, an answer can be found by looking at the history of optical storage devices. But first of all, what is optical storage? IBM for example defines this as ″any storage method that uses a laser to store and retrieve data from optical media″ [69]. Almost immediately one thinks of the CD-ROM, DVD and Blu-ray, which are probably the most famous optical storage devices. They have a line of small pits inscribed on a spiral track on the disc, which is scanned by a laser. The intensity of the reflected light is retrieved and converted into an electrical signal.

In regards to the conversion from the analog audio signal to the digital pits and lands, pulse code modulation was used, where the analog signal is sampled at uniform intervals and a 14 bit A/D converter was used to then transform the digital signal back to analog [70, 71]. In EROS, the transformation is done by converting decimal numbers into binary and back again. However, as it will be explained in the following sections, there are different ways to achieve the conversion and some turn out to be more efficient than others.

Apart from the encoding, there is another crucial aspect to a successful storage device, which is somewhat linked to encoding: error handling. The researchers who worked on the development of the CD realised that an error correction algorithm was required, but also faced an issue similar issue to what will be described in the following sections:

They were not really sure what kind of errors would most likely need correction? Of course, scratches and greasy fingerprints were obvious, but the effect of them was unclear; would this cause single bit errors, or many neighbouring errors, so called burst errors. Another, much bigger concern was errors introduced during mass production, whereas EROS's biggest concern lies in the harsh environment it will be operated in [70]. The final section in this chapter will cover some error correction techniques and explain the effect on data capacity and fibre length of the EROS device.

4.2 Background

There are different ways to store information and one of the first things to consider, particularly when storing numbers is which format to choose. As mentioned in Chapter 3.3.1, the first EROS prototype was encoded in a non-binary format, so the numbers were not required to be translated into the more commonly used binary format. There are however some benefits when it comes to binary formats. Translating floating point numbers into binary has the advantage of implementing more commonly used error correction and encoding algorithms, but this also was mentioned as a potential requirement in conversation with Parker Aerospace. The way floating point conversion typically works, is that a decimal number is converted into a a format that includes a sign, a mantissa and an exponent. Depending on the requirement for range and precision, the number of bits allocated to represent the mantissa and exponent is adjusted. The most commonly used floating point conversion is the IEEE 754 standard, which has been developed in 1985 and has been further improved and maintained since then [72]. The 32-bit standard allocates one bit for the sign, 8 bit to represent the exponent and 23 bits for the mantissa [73]. This standard is known as single precision. The double precision uses a 64-bit number, in which one bit is allocated for the sign, 11 bit for the exponent and 52 bits for the mantissa.

In the following paragraph will focus on the feasibility of using these conversion methods for this project. The calibration data provided by Parker Aerospace can be found in Table B.1. The data consists of floating point numbers that represent polynomial coefficients. This means that using the 64-bit conversion requires a total number of 2368 bits of storage. For the 32-bit conversion, this number drops to 1184 bits. This is a large number for storing data in a form of Bragg gratings, especially considering that this does not include any bits required for error detection and correction. With the spectral interrogation method, which is described in Chapter 3.2, where only the optical spectrum of the gratings are considered, the maximum amount of bits stored in a fibre depends on the laser bandwidth and the grating bandwidth. Assuming the spectral bandwidth of the light source is 100 nm and the spectral 3-dB bandwidth of a Bragg grating is 0.3 nm, a total number of 333 gratings fit into the spectral bandwidth of the laser. This does not cover the requirement, hence a different solution for the number conversion had to be found to reduce the amount of bits that have to be stored.

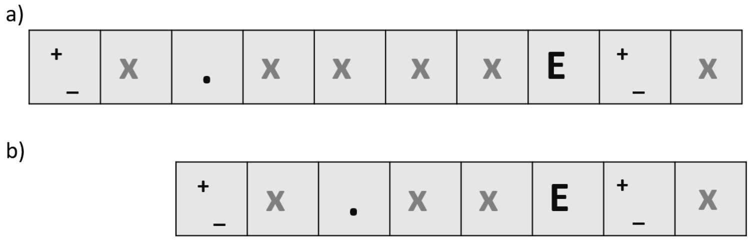

FIGURE 4.1: Example format of the calibration data from table B.1: a) long format, b) short format.

Reviewing the calibration data file from table B.1 in the Appendix, a more efficient way of representation was found. All calibration data can be represented in the format, which is visualised in Fig. 4.1 a. In this example, each grey "x" is a place holder for one digit of a calibration number. Out of the 37 calibration numbers, only 4 require this precision. The other 33 numbers could be presented in the shorter format, which is shown in Fig. 4.1 b. It was therefore decided to proceed the calculation of the data storage requirement based on two formats: long, with 6 bits and short, using only 4 bits. Fig. 4.2 shows an overview of the precision that can be achieved for a floating point value under the different conversion schemes. Although the precision of the IEEE standardised formats are better, the custom format fulfils the given requirements and provides therefore a good alternative to the standard.

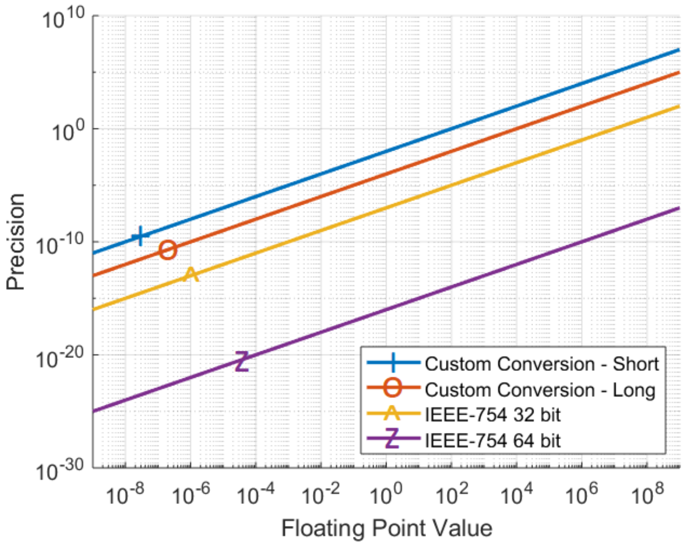

FIGURE 4.2: Overview of the precision for different floating point values. The precision changes with the value of the floating point as a fixed amount of bits is defined for the exponent and the mantissa. The custom conversion performs worse in precision, however, it does fulfil the requirements and is therefore proposed for this application. Custom Conversion - Short uses 4 bits, whereas Custom Conversion - Long uses 6 bits.

In order to then calculate the required storage capacity, the 4 or 6 digit decimal floating point numbers were translated into a binary string. For this, the number was divided up into digits and for the purpose of explaining the conversion, the signs are disregarded. When it comes to translating decimal numbers into binary, the length of the binary number can vary depending on the size of the decimal number. So is a decimal 1, a binary 1, but a decimal 2 translates to a binary 10. Assuming both decimal numbers 1 and 2 are encoded one after the other as one string, it would be impossible to know when one number starts and the other finishes. With zero-padding, all binary numbers will have the same length, by adding the appropriate number of "0" on the left. If the highest number is a 2, then a decimal 1 would be a 01. This allows to distinguish between numbers. For the calibration data, we look at single digits and convert those from decimal to binary. The largest decimal digit is, of course "9", which is 1001 in binary. Therefore all binary numbers must also be 4 digits long. Considering 3.0020E3 from table B.1, the digits to be converted are 3, 0, 0, 2, 0 and 3. Translating each digit into binary of four digits length then results in a binary sequence of 0011, 0000, 0000, 0010, 0000 and 0011. The total amount of bits required to be stored is $37 \cdot 4 \cdot 6 = 888$ for the long format and $37 \cdot 4 \cdot 4 = 592$ for the short format.

Evaluating the efficiency of this conversion it becomes clear that this way of translating decimal numbers into binary is not very efficient. To represent a decimal 8 or a 9 in binary, four binary digits are required. But this means that only two different states in a 4-bit binary sequence are used (namely 1000 for the decimal 8 and 1001 for the decimal 9). But with four binary digits, many more numbers can be represented: 10, 11, 12, 13, 14 and 15. Numbers above 9 are however not used with the current format, which means 75% of the four-digit binary is unused to the cost of an additional binary digit per decimal digit. To make this conversion more efficient, instead of converting each individual decimal digit into a binary sequence, the whole number can be converted into binary. This means instead of converting 9, 9, 9, 9, 9, 9 into binary, the number 999999 is converted as a whole. This results in the binary string 11110100001000111111, which is 20 bits long, instead of 24 bits for individual conversion. For the whole calibration data file, it results in a total amount of bits of $37 \cdot 20 = 740$ for the long format and $37 \cdot 14 = 518$ for the short format. This is an increase in efficiency of 20% for the long format and 15% for the short format.

From this example, one can see that a further improvement can be achieved by storing the full calibration file, so all 37 numbers in one single binary sequence. For the long format (using 6 digits of the calibration number), this results in a decimal number with $37 \cdot 6 = 222$ digits, and $37 \cdot 4 = 148$ digits for the short format (using only 4 digits of the calibration number). Converting a decimal number of 222 digits into binary with a binary length of 4 bits, results in a binary string with 738 bits in length. This assumes that each decimal digit is a '9'. For the short format, the 148 digit long decimal number, results in a binary string with 492 bits in total. The efficiency increase for the long format from 740 bits for the full number conversion to 738 bits for the full file conversion is negligible, but for the short format, the efficiency increased by 5%. These findings are summarised in Fig. 4.3, where the bars indicate the amount of bits required to store the full calibration data file.

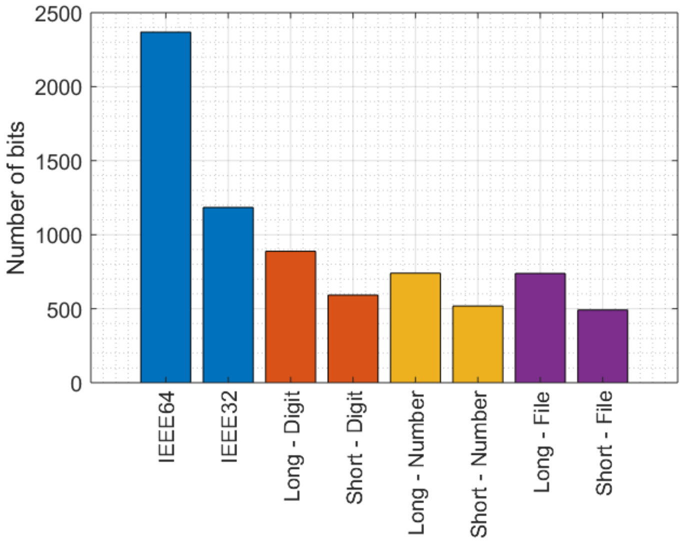

FIGURE 4.3: This figure shows the number of bits required to store the full calibration data file using different conversion methods.

In the following sections further analysis on the data encoding is preformed, particularly in regards to different combinations can be achieved and thus how much data can be stored, but also in regards to the grating design and the parameters that define the amount of data storage in the EROS device.

4.3 Encoding Scheme

Although it is clear that the way forward will go towards a binary system, for completion, the encoding scheme that was used for the first prototype will be analysed and evaluated in the following section, along with the binary encoding scheme proposed for the future device. An example of real calibration data of a typical commercial optical sensor was provided by Parker Aerospace and can be found in Table B.1. As already mentioned in Chapter 3.3.1, two prototypes were fabricated to store data in a decimal and a binary format.

Assuming the spectral bandwidth of the light source is 100 nm and the spectral 3-dB bandwidth of a Bragg grating is 0.3 nm, a total number of 333 gratings would fit into the spectral bandwidth of the laser. In Chapter 3.3.1, an encoding scheme was introduced, which was used for the first EROS prototype. The working principle was shown in Chapter 3.3.1 Fig. 3.11: The spectrum was divided up into four section, each section representing one digit of the calibration number. Each section was then again divided up into 10 subsections, labelled with a digit from 0-9, representing a value bin for the Bragg grating. If the central wavelength of the Bragg was placed in the first section (= first digit of the calibration number), and in the third subsection position (= third value bin), the encoded number is then a 2 (as the counting starts from zero). So that means that the first digit of the calibration number is 2. This is arguably not the most efficient way of storing information as 9 out of 10 subsection bins would be empty. One way to make this encoding method more efficient is by adding another grating in the subsection. Instead of only encoding *one* grating per subsection, *multiple* gratings are encoded per subsection. This however only works if the gratings are distinguishable: If multiple gratings with the same shape were written into one subsection, it would not be possible to know which of those gratings to read out first. Assume the central wavelength of one grating falls is in the second bin (= digit 1) and the other grating in the sixth (= digit 5). Because it is not possible to distinguish between the two gratings, it is not clear if the encoded number is 15 or 51. This is why different grating types are important. Using different grating types (uniform or Gaussian apodised, π-phase shift, 100 π-phase shift and position of the shift) solves this problem as Fig 4.4 shows: Assuming it is defined that Gaussian gratings are read out first and π-phase shift gratings second. If a Gaussian grating is placed in the first section, and third bin in the subsection and a π-phase shift grating is placed in the 6th subsection bin, it can be read out that the ″first digits″ of the calibration number are: 25. The question here is how many digits can be stored with this encoding scheme? Assuming an overall bandwidth of 100 nm and a grating bandwidth of 0.3 nm, 333 bins, or subsections can be formed. 10 subsections form 1 section, to represent the values from 0-9; therefore 33.3 sections can be formed. With 6 different variations of gratings shapes that were listed in Chapter 3.4 a total of $33 \times 6 = 198$ digits that can be stored on one location using this non-binary encoding scheme. The current small spot direct UV writing system limits the length of which Bragg gratings can be inscribed into a fibre to 250 mm. Assuming a grating length of 5 mm, a total number of 50 locations are available to inscribe the Bragg gratings. The potential data storage capacity is therefore $199 \times 50 = 9950$ decimal digits. Looking at the different data formats of the calibration data, where the total amount of decimal digits to be stored for the long format is 222 and for the short format 148, it becomes clear that non-binary encoding is a potential candidate for encoding and there is still some room left for implementing error correction.

However, due to the requirement of implementing a binary encoding scheme, the rest of this chapter will focus on the binary encoding scheme. The easiest implementation of a binary system using Bragg gratings would be to divide the optical spectrum in different bins and using the existence of a grating as a ″1″ and its absence as a ″0″. The main challenge for this binary system however is that there is only a limited number of Bragg gratings that can be superimposed on one location, and therefore a limited number of ″1″ that can be placed. For example, there could be ten bins in the spectrum,

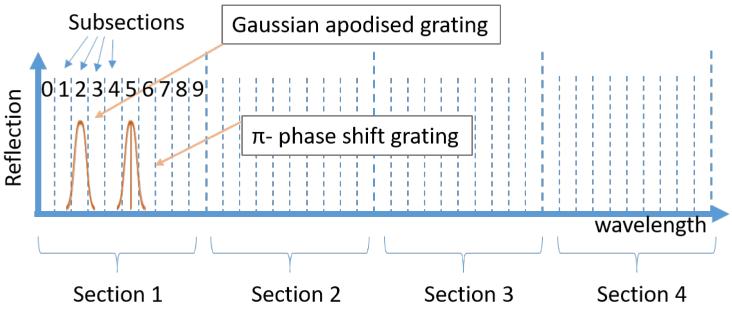

FIGURE 4.4: This diagram is a representation of the spectral view on one spatial location. It shows the how individual digits can be stored using sections and subsections. The spectral space is divided up into sections of 10, with each bin representing a number from 0-9. Inscribing a Bragg grating in a respective bin, means ”storing” the digit. Different gratings types allow the spectral space to be used more efficiently, as multiple digits can be stored rather than only one digit, leaving the other 9 places unoccupied.

but only three gratings. So there are only three ”1”s and seven ”0”, which is not a binary system in the usual sense. Therefore it is not possible to immediately use the optical spectrum as binary string to store the calibration file. To account for this, an encoding scheme was developed that connects the spectral system with the binary system to allow an efficient encoding scheme.

To better follow the explanation of the encoding scheme, the focus will be laid firstly on Gaussian apodised gratings only. Additional shapes and features and their effect on the encoding scheme will be discussed later. For this explanation, only one location will be considered, the same scheme is applicable to all other locations. The encoding scheme consists of two matrices: the *Spectrum* matrix and the *Encode* matrix. The *Spectrum* matrix has space for as many binary digits as there are the spectral bins. So if the wavelength range is from 1500-1600 nm and the spectral separation between two gratings is 1 nm, then there are 100 bins at one location. This means the *Spectrum* matrix has 100 empty places where a ”0” or a ”1” can be placed. By default, if there is no grating inscribed on this location, the *Spectrum* matrix row consists of only ”0”s. The amount of ”1”s that can be included in the matrix row therefore depends on how many gratings can be superimposed on one location.

Figure 4.5 shows an example of the *Spectrum* matrix on the left, if there were only six spectral bins and only two gratings could be superimposed. Each row shows a a different possibility to place the two gratings. This matrix contains of 15 rows, which means that there are 15 different ways to place two ”1”s in six bins. Instead of manually writing these combinations down, they can be calculated with the following equation [74]:

$$ {}_bC_n = \frac{b!}{n!(b-n)!} \tag{4.1} $$

In this equation, ${}_bC_n$ is the number of combinations, b is the number of bins and n is the number of superposed gratings, which represents the amount of ”1”s in one location.

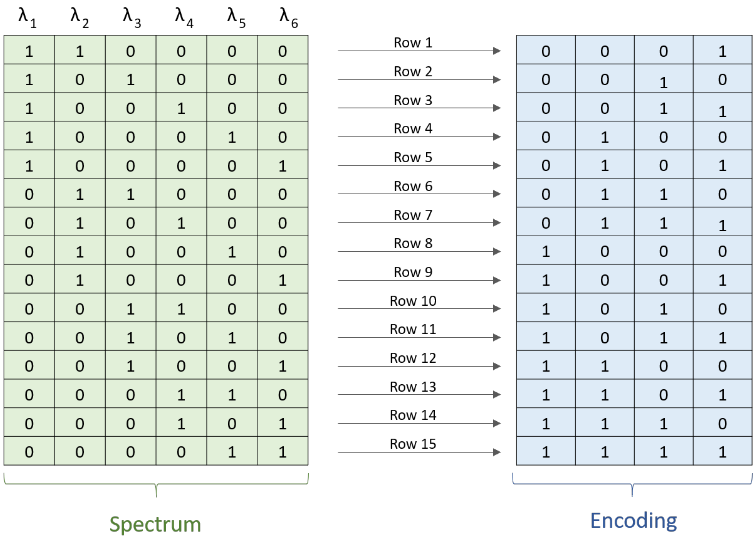

λ_1	λ_2	λ_3	λ_4	λ_5	λ_6					
1	1	0	0	0	0	Row 1	0	0	0	1
1	0	1	0	0	0	Row 2	0	0	1	0
1	0	0	1	0	0	Row 3	0	0	1	1
1	0	0	0	1	0	Row 4	0	1	0	0
1	0	0	0	0	1	Row 5	0	1	0	1
0	1	1	0	0	0	Row 6	0	1	1	0
0	1	0	1	0	0	Row 7	0	1	1	1
0	1	0	0	1	0	Row 8	1	0	0	0
0	1	0	0	0	1	Row 9	1	0	0	1
0	0	1	1	0	0	Row 10	1	0	1	0
0	0	1	0	1	0	Row 11	1	0	1	1
0	0	1	0	0	1	Row 12	1	1	0	0
0	0	0	1	1	0	Row 13	1	1	0	1
0	0	0	1	0	1	Row 14	1	1	1	0
0	0	0	0	1	1	Row 15	1	1	1	1

FIGURE 4.5: The conversion or look up table between *Spectrum* and *Encoding* matrix. The *Spectrum* matrix is a representation of the grating positions in the optical spectrum, whereas the *Encoding* matrix is a binary representation of the row number.

As already mentioned, although this spectral matrix is in a binary format, it is not truly binary, as the distribution of ″1″s and ″0″s is restricted. To translate this *Spectrum* matrix into a truly binary format, each row is allocated a number. In the example above the first row is allocated a one, the second row a two, the third a three and so on. This number is then translated to the binary format and zero-padding is applied, so ensure that the binary row numbers are the same length. The first row in the *Spectrum* matrix in Figure 4.5 is therefore allocated the binary string ″0001″ and the second row is ″0010″ and so on. This translation from the *Spectrum* matrix into the true binary format creates this new matrix, which is called *Encode* matrix. The *Encode* matrix is a truly binary matrix, which can consist of an unlimited number of ″1″s and it serves as a look up table for the calibration data.

In the example above, there are six spectral bins and two superposition, creating 15 different combinations. If the calibration data only contained digits between zero and three, each decimal digit could be represented with two binary digits: 0 = ″00″, 1 = ″01″, 2 = ″10″ and 3 = ″11″. To encode a sequence of two decimal digits, for example 1-2, both digits would be individually translated into binary: ″01″ and ″10″ and combined to one string: ″0110″. This sequence is then looked up in the *Encoding* matrix. ″0110″ can be found on row 6, which means that a grating has to be inscribed at the spectral position λ_2 and λ_3 (according to the *Spectrum* matrix positions). This is how the encoding step works. Decoding is the same principle just the other way around. If we for example read out a Bragg grating with the central wavelength at λ_3 and λ_5, the string in the *Spectrum* matrix would be ″001010″, which can be found in row 11. Row 11 in the *Encode* matrix is ″1011″ and since we know that each of our decimal digits is formed with two binary digits, the binary string ″1011″ can be split up into two binary digits strings: ”10”, which represents a decimal 2 and ”11”, which represents a decimal 3. So the number stored was a decimal 23.

An important point to mention is that the *Encoding 1* matrix must always contain equal or less rows compared to the *Spectrum* matrix to not allow a combination that cannot be represented in the *Spectrum* matrix. Consider for example six spectral bins with three superpositions, as shown in Fig. 4.6. Binary strings up to ”10100” can be represented with this scheme, but the binary string ”10101” for example would not have a spectral representation. If a number does not have a spectral representation, it cannot be represented and therefore does not exist in the encoding scheme. This would not be acceptable for storing calibration data and therefore the *Spectrum* matrix must always be longer than the *Encoding* matrix, as indicated with the orange *Encoding 2* matrix in Fig. 4.1. Here there exist a number of spectral representations that do not have a binary string associated to them. Therefore these spectral combinations will not be used to encode information.

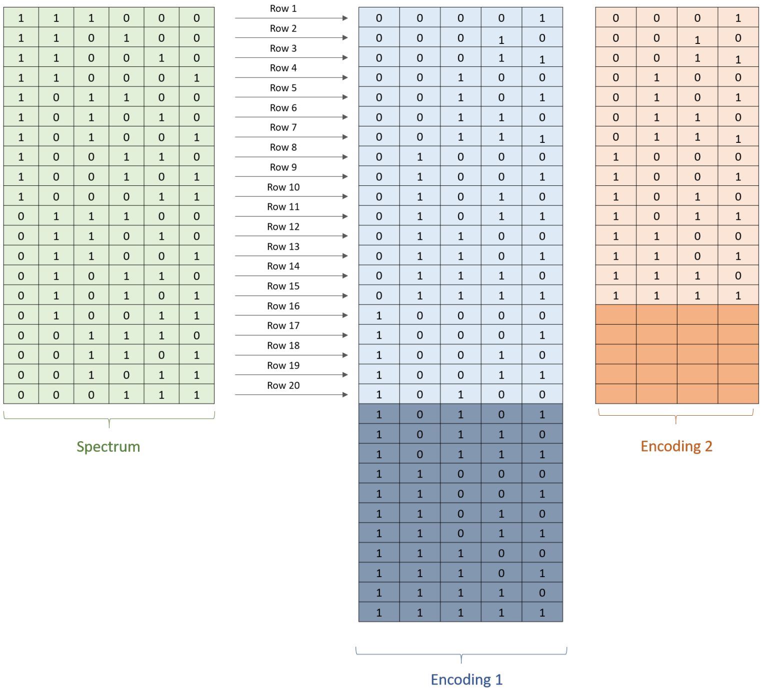

Spectrum

1	1	1	0	0	0
1	1	0	1	0	0
1	1	0	0	1	0
1	1	0	0	0	1
1	0	1	1	0	0
1	0	1	0	1	0
1	0	1	0	0	1
1	0	0	1	1	0
1	0	0	1	0	1
1	0	0	0	1	1
0	1	1	1	0	0
0	1	1	0	1	0
0	1	1	0	0	1
0	1	0	1	1	0
0	1	0	1	0	1
0	1	0	0	1	1
0	0	1	1	1	0
0	0	1	1	0	1
0	0	1	0	1	1
0	0	0	1	1	1

Encoding 1

Row 1	0	0	0	0	1
Row 2	0	0	0	1	0
Row 3	0	0	0	1	1
Row 4	0	0	1	0	0
Row 5	0	0	1	0	1
Row 6	0	0	1	1	0
Row 7	0	0	1	1	1
Row 8	0	1	0	0	0
Row 9	0	1	0	0	1
Row 10	0	1	0	1	0
Row 11	0	1	0	1	1
Row 12	0	1	1	0	0
Row 13	0	1	1	0	1
Row 14	0	1	1	1	0
Row 15	0	1	1	1	1
Row 16	1	0	0	0	0
Row 17	1	0	0	0	1
Row 18	1	0	0	1	0
Row 19	1	0	0	1	1
Row 20	1	0	1	0	0
	1	0	1	0	1
	1	0	1	1	0
	1	0	1	1	1
	1	1	0	0	0
	1	1	0	0	1
	1	1	0	1	0
	1	1	0	1	1
	1	1	1	0	0
	1	1	1	0	1
	1	1	1	1	0
	1	1	1	1	1

Encoding 2

0	0	0	1
0	0	1	0
0	0	1	1
0	1	0	0
0	1	0	1
0	1	1	0
0	1	1	1
1	0	0	0
1	0	0	1
1	0	1	0
1	0	1	1
1	1	0	0
1	1	0	1
1	1	1	0
1	1	1	1

FIGURE 4.6: This figure shows the importance of ensuring that the *Encoding* matrix is shorter than the *Spectrum* matrix. In the example of the *Encoding 1* matrix, there are some binary combinations (”10101” and larger) that do not have a spectral representation. If now the number ”11101” should be encoded, there would be no representation and therefore it would not be possible to store this number in the spectrum. The *Encoding 2* matrix on the other hand is allocating all binary possibilities a spectral representation. In this case, it does not matter that some of the spectral representation do not have a binary string allocated, as it only means that this spectral combination will never be inscribed.

How much data can be stored in the fibre therefore depends on the number of rows of the *Spectrum* matrix, as the longer the *Spectrum* matrix, the longer the *Encoding* matrix and therefore the more bits can be stored. All depends so to say on how many different ways there are to define the spectral feature of gratings in a given spectrum.

The equation to calculate the number of combined combinations N is defined by the number of spectral bins b, the amount of superimposed gratings s and how many different types of grating t can be inscribed:

$$N = \sum_{n=1}^{s} t^n \cdot {}_bC_n \tag{4.2}$$

The second part of the equation, ${}_bC_n$ is explained in equation 4.1, it calculates how many different ways there are to place the gratings with respect to the spectral bins, whereas the first part of this equation calculates how many different ways the gratings can be placed without taking the spectral space into consideration. To give an example: Consider two gratings are inscribed into 6 spectral bins, as already shown in Fig. 4.5, there are ${}_6C_2 = 15$ different ways on where the two gratings could be located in the spectral space. If now also different gratings shapes and features should be considered, then the first part of equation 4.2 must be added. This part in general determines the amount of possibilities there are to arrange a set of numbers if repetitions are allowed. In the encoding scheme, it calculates the number of possibilities to arrange the different grating types. This part does not consider the spectral bins, but only the inscribed gratings. If for example a Gaussian apodised grating is allocated the number 1 and a π-phase shift a 2, then there are $2^2 = 4$ ways to arrange the 2 digits: ″11″, ″12″, ″21″ and ″22″. And finally the sum then allows also lower numbers of gratings (either only Gaussian or only π-phase shift grating).

To give an indication if it is possible to store the calibration data into a fibre using this scheme the following assumptions are being made: The tunable laser has a bandwidth of 100 nm and the grating bin is 1 nm wide, which has been experimentally tested with the prototype Cyclops 75, shown in Chapter 3.3.1, which results in 100 spectral bins. Further it is assumed that 20 gratings of a length of 5 mm can be superimposed at a fluence of $1\,kJ/cm^2$, as shown in Chapter 2, Fig. 2.17 and a distinction between six different grating types can be made: Gaussian and uniform gratings, π-phase shift gratings, 100 π-phase shift gratings, 100 π-phase shift gratings with a dip shifted by 1/3 and 100 π-phase shift gratings with a dip shifted by 2/3. This then results in

$$\sum_{n=1}^{20} 6^n \cdot {}_{100}C_n = 2 \cdot 10^{36} \tag{4.3}$$

combinations, and therefore $2 \cdot 10^{36}$ rows in the *Encoding* matrix. Converting this into binary, results in a string with 121 bits. To ensure that all binary combinations can be represented in the spectrum (see Fig. 4.6), one bit is removed, leaving a string of 120 bits. If the short number conversion from Fig. 4.1 is used ($37 \cdot 4 = 148$ digits represented with 4 digits each), a conversion from this decimal to binary results in a binary string of 492 bits. This means in order to encode the whole calibration file, $\frac{492}{120} = 4.1 \approx 5$ spatial positions, which is a length of 25 mm of fibre.

To look at this encoding scheme more generally: Each calibration number in Appendix B can translated from a floating point number into a decimal number of four or six digits as defined in Section 4.2. All individual decimal four (or six) digit numbers of the calibration data file can then be added to one long decimal number, which is converted into a binary string. This binary string gets divided up into binary sections of a fixed length. The length is dependent on the number of rows of the *Encode* matrix consists of, which is in turn dependent on the number of spectral bins, the number of superpositions and the number of different grating types.

This example shows that the calibration data provided by Parker Aerospace can be stored in a fibre by inscribing Bragg gratings and reading the spectral and spatial information using OFDR. But how do superposition, number of spectral bins and number of grating type correlate in respect to the fibre length? This is further investigated in the following paragraph.

Fig. 4.7 shows the flow diagram for a model which outputs the required fibre length to store the calibration data dependent on a variation of certain parameters. Starting on the top left, the individual numbers in the calibration data file are translated into a short format according to Fig. 4.1 b. All these numbers are then concatenated to one decimal number of 148 digits, which translates to 492 binary bits. Any calibration number following the format of Fig. 4.1 b will now be representable in 492 bits or less.

The second part of the model is arguably the more interesting part as it contains the control knobs to change the parameters. There are three main variables that determine the length of fibre required to store data with this encoding scheme: number of superimposed gratings, number of spectral bins, number of grating types. The default values for superposition, spectral bins and grating types are shown as green number on the bottom left of Fig. 4.7. These are fed into the equation, which returns a decimal number, with the amount of different combinations to arrange the given gratings and grating types in the spectral bins. This number is then converted to binary and one bit is removed from its length to ensure that the *Encode* matrix is shorter than the *Spectrum* matrix, as shown in Fig. 4.6. The resulting length is the capacity length and together with the data length of 492 bits, the fibre length is calculated.

To see the dependencies of the three parameters to each other, it would be best to change all three parameters simultaneously and plot two parameters versus the fibre length results in three 3D plots. 3D plots however are more difficult to present on a 2D sheet of paper without the ability to pan, tilt and zoom, so a more conventional plot with the three parameters combined was plotted to summarise the key messages.

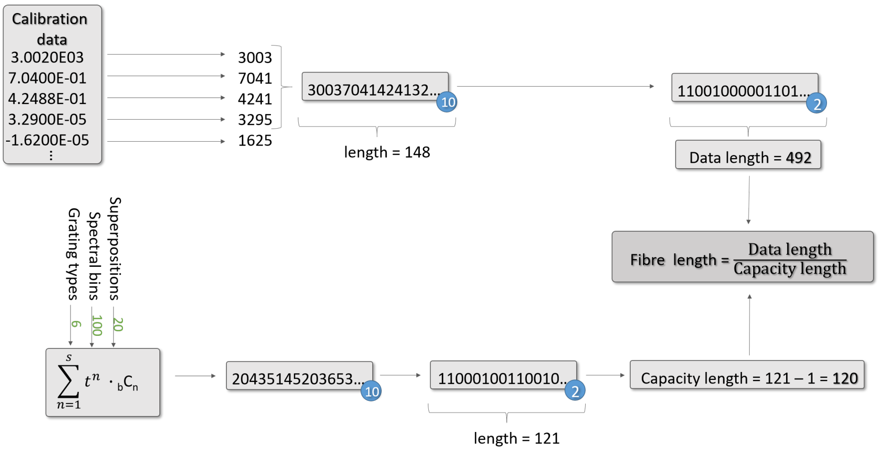

FIGURE 4.7: This flow chart visualises the different steps of the encoding scheme: starting on the top left with the calibration data, which is converted into one single decimal string of a length of 148 digits. Converting this into binary with a length of 4 bits per digit results in a binary string with 492 bits. The bottom left on this figure shows the equation to calculate the number of ways that the given superimposed gratings of certain types can be arranged in the respective spectral bins. This number is then converted into binary. One bit is subtracted to ensure that the *Encoding* matrix is shorter than the *Spectrum* matrix. The required fibre length is then calculated by dividing the data length and the capacity length.

Fig. 4.8 shows a graph with one plot for each parameter with the fibre length required to store the calibration data provided by Parker Aerospace on the x-axis. The y-axis displays the parameter value, which means that this axis is applicable for all three parameters and therefore shows the number of spectral bins, superpositions and grating types. For each parameter plot, two parameters were fixed at their default value, and the parameter of interest altered between a certain range. The default values were as follows: the default number of superimposed gratings was 20, for spectral bins 100 and the number of different grating types was 6 (uniform, Gaussian and various phase shifts as mentioned in Section 3.4). These were the parameters used in the above example. As an example on how to read this graph, the green stars show how varying the number of grating types affects the length of the fibre, for a fixed number of 20 superimposed gratings and 100 spectral bins.

Analysing the blue graph in Fig. 4.8, the number of spectral bins was varied between 50 and 150, while the number of superimposed grating is fixed at 20 and the number of grating types fixed at 6. This blue graph is a very steep curve compared to the red and the green, which indicates that a change in the number of spectral bins will have a smaller impact on the overall fibre length required to store the full calibration file. As already expected with a higher number of spectral bins, so a larger sweeping range of the tunable laser, we achieve a higher data storage capacity, which means we can store the data in a shorter fibre length. In the best case scenario, only $\lceil 3.7 \rceil = 4\,\text{cm}$ are required to store the whole data set, in a worst case, if only 50 spectral bins are available, it would require $\lceil 5.1 \rceil = 6\,\text{cm}$. The value has to be rounded up to the full

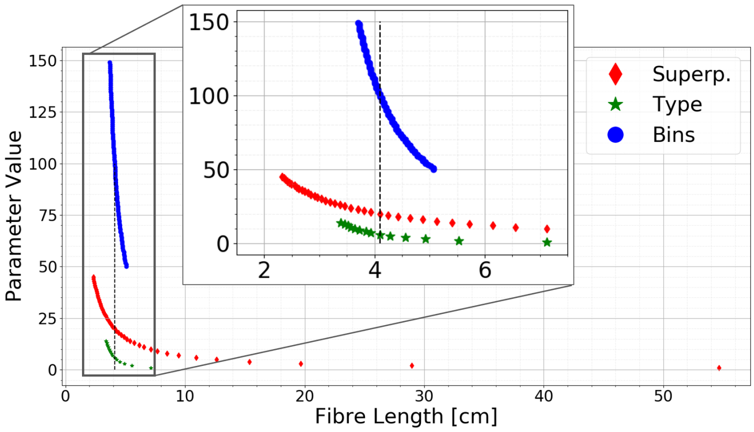

FIGURE 4.8: Visualisation of the effect on the parameters on the fibre length. The blue graph shows the effect that changing the number of spectral bins has on the length of fibre for a fixed number of superpositions (20) and a fixed number of grating types (6). The red graph shows the effect of varying the number of superpositions with a fixed number of bins (100) and a fixed number of grating types (6). The green graph shows the effect of grating types on the fibre length for 100 spectral bins and 20 superimposed gratings.

integer as the individual grating length is 5 mm with a separation of 5 mm between the individual gratings.

The green graph shows the impact of different grating types on the required fibre length. Compared to the blue line, this curve is much flatter. This means, with a small change in the parameter value, a big change in teh fibre length can be achieved. It is therefore more important to focus on creating more gratings types rather than increasing the spectral bin size in order to store more data in a shorter length. In the insert of Fig. 4.8 it is shown that the required fibre length decreases by 3 cm by increasing the number of grating types from 1 to 3 grating types.

The effect of superposition on fibre length is shown in the red plot in Fig. 4.8. This curve is the flattest line out of the three, which indicates that length improvement potential is greatest for this parameter. With the restriction of only one grating per location, the overall length required would be 55 cm and therefore exceed the maximum length of fibre that can be inscribed in one run with the small spot direct UV writing technique. This is of course a limitation that can be mitigated by using different translation stages. Inscribing two gratings on one location bring the length of fibre down to 29 cm, with three gratings to 20 cm. The benefit of focusing the development effort on superimposing gratings becomes evident with this figure. The black dashed line in the figure indicates the parameters for the example above with the default parameters to give an indication of the feasibility of the values. These default parameters are: 20 superpositions, 6 different grating types and 100 spectral bins as described in Chapter 3.

The example and the model show that it is possible to store the calibration data in a short piece of fibre. However, for the real application, more than just the data bits will be stored. To ensure a correct and reliable readout, an error detection, or even error correction algorithm needs to be put in place.

4.4 Error Detection and Error Correction

So far, data capacity alone has been considered the most important factor for storage. However, for a real application, it must be assured that the data is read out reliably. Therefore mechanisms for error detection or preferably error correction needs considering in the design. It is important to take this into consideration, as this error detection and correction will add additional bits to the data and therefore will increase the required fibre length of the final device.

To understand which error correction algorithms to use, it is important to understand the errors that occur. For EROS, this is quite difficult to predict, as the main source of errors are expected to be due to environmental conditions. However, using data that was taken from one of the prototypes (Fig. 3.13 in Chapter 3.3.1), it becomes evident that one of the main error type is a burst. Burst errors in general are difficult to correct as many errors occur back to back. Burst errors can be spread out with a technique called interleaving. Fig. 4.9 shows a graphical representation of interleaving. The data string on top spelling "Southampton" is ordered according to the numbers on top (1-11). It is then interleaved, so newly ordered into a string that is written. When reading the string, a burst error occurred and three digits were not read. The string is then ordered again from small to large numbers and the burst error is distributed along the data string, which makes it easier for other error correction algorithms to correct again, similar to how it makes it easier for us to read when single letters are missing across the whole word rather than on one location only. Interleaving does usually not leave the data in a random order, but places neighbouring bits as far away as possible form each other.

Having distributed the burst errors into bit errors now, these bit errors need to be addressed. A common error correction code for bit errors is a convolutional code. These have been successfully used for the first CD and work by convoluting error correction bits and data bits [17, 75, 76, 77]. The convolution adds redundancy into a sequence of bits and is typically implemented with a shift register. An example of such a shift register from [77] is shown in Fig. 4.10. The input data stream is shown on the top of the shift register, as well as on the bottom of the figure. The two bits in the middle are function as the memory of the register (m_1 and m_2) and the two bits on the right are the output bits. The "+" in the middle can be understood as a binary function, which results 0 if the summation is even and 1 if the summation is odd. All bit streams for each step are shown on the bottom of the figure.

FIGURE 4.9: Visualisation of interleaving to reduce the effect of burst errors: A data string is interleaved, in this case a random order was applied. This string is then written and read out. During read out, a burst error occurred. Since the string is reordered from 1 to 10, the burst error in the middle of the string during read out is now distributed along the whole word.

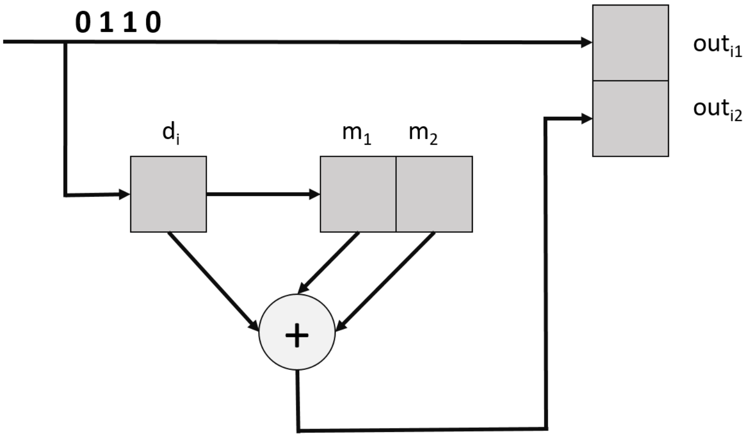

	d$_i$	m$_1$	m$_2$	out$_{i1}$	out$_{i2}$
step 1	0	0	0	0	0
step 2	1	0	0	1	1
step 3	1	1	0	1	0
step 4	0	1	1	0	0

FIGURE 4.10: Example of a shift register used for convolutional encoding. The bit sequence 0110 on top is the input for the shift register and is added one bit at a time. The two "m" boxes are the memory bits in the register. They "remember" previous inputs. By default, the "m" bits are zero at the start. Below the register, the sequence is shown for the input bit stream: the first bit added to the register is a "0", which falls into the d_i box. m_1 and m_2 are both "0". The output consists of two bozes: out_{i1} and out_{i2}. out_{i1} is the input bit, in the first instance this is "0" and out_i2 is calculated from the middle part of the shift register: the binary addition of d_i, m_1 and m_2 (0+0+0=0). For the next input (a "1"), the "0" from d_i is shifted into m_1 and the "0" from m_1 is shifted into m_2.

If the data stream to be sent is 0-1-1-0, the output bit stream can be generated as follows: In the initial state, the two memory bits are 0. The first data bit 0 is fed into the register at d_i, which results in output stream out_{i1} to become 0. Since the sum of the two memory bits and the data bit is 0, the output bit out_{i2} is 0. The second data bit is 1, so out_{i1} is 1, and the sum of the memory bits and the input bits is 1, which makes out_{i2}=1. The 1 shifts into the memory bit and the third data bit is fed into the register. This makes the output out_{i1}=1 and out_{i2}=0, since the sum of the memory bits and the input bit is now 0. This continues until the last data bit is fed into the register. The original data stream 0-1-1-0 is now encoded into 0-0-1-1-1-0-0-0.

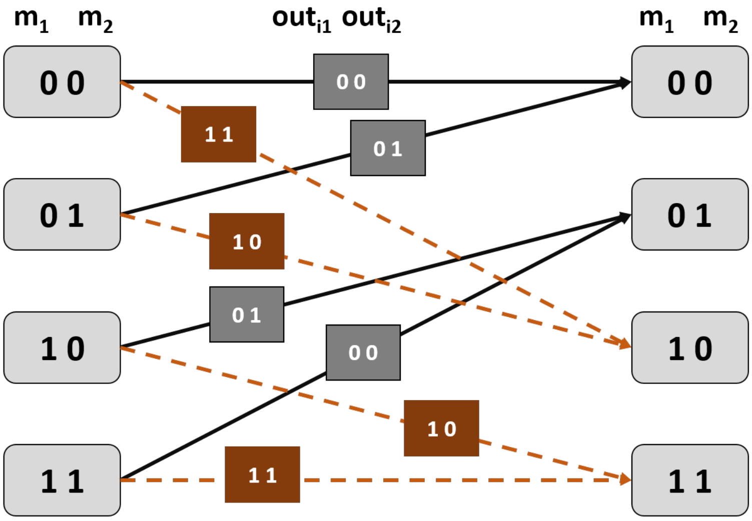

FIGURE 4.11: Transition diagram for visualising the possible transitions for the register shown in Fig. 4.10. It helps for the decoding and encoding of information. This diagram is set up as follows: On the left side, there are the *current* memory states from the register. Suppose we start in the memory state ″00″. If a ″1″ is input into the shift register in Fig. 4.10, the *future* memory state will be ″10″ (as the left memory box with a ″0″ is pushed to the right memory box, and the ″1″ from d_i is pushed into the first memory box). In this diagram, an orange dashed arrow is then drawn towards the right memory state ″10″. If however instead of a ″1″, a ″0″ was given as input, the *future* memory state would be ″00″. A ″0″ input is shown as a black arrow, which now connects the *current* memory state (″00″) and the *future* memory state (″00″). The rectangular boxes on the arrows show the output states of the shift register.

To decode the data and extract the original data stream (0-1-1-0), a transition diagram is generated, shown in Fig. 4.11. This diagram shows the current memory states on the left, the two output bits in the middle and the future memory states on the right. This diagram is created to visualise the possible transitions from each memory state. The black continuous line shows the path when a 0 has been put into the register, the orange dashed arrows when a 1 has been fed in. The diagram is created by comparing the current and future transition state and generating the input and resulting output to get to this state. For example: starting at the current memory state 0-0 and assuming a 1 has been fed into the register. The next memory state output bits will then be 1-0. A dashed orange arrow is drawn from 0-0 to 1-0, since a 1 has been fed in. The first output bit will then be 1, as this always represents the input bit (see Fig. 4.10), and the second output bit will be 1, since the sum of the two current memory bits with the input bits is 1. The rest of the diagram is completed by repeating these steps accordingly.

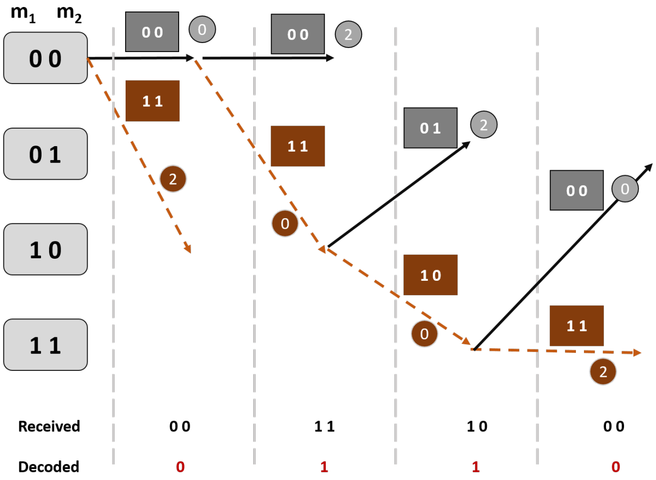

FIGURE 4.12: Trellis diagram using the Viterbi algorithm. The memory states on the left and the received data on the bottom. The square boxes show the output and the circles the Hamming distance between the output and the received data. The triangles show the bit that is fed into the register and the triangles with the red outline are the codes that are actually sent.

Once the transition diagram is completed, a trellis diagram can be created. A trellis diagram finds the most likely transmitted bit sequence from the actually transmitted sequence. The algorithm used for this is called Viterbi algorithm and the trellis diagram which shows the different paths for the received bit stream is shown in Fig. 4.12. Starting at the left side, where the memory bits are shown. By default, the memory bits are initially ″00″. From this state, there are two different transitions possible (as shown in the transition diagram in Fig. 4.11) from ″00″ to ″00″ and from ″00″ to ″10″ (black arrow and orange dashed arrow). From the same transition diagram, it can be seen that the outputs for path ″00″-″00″ (black arrow) are ″00″ (grey box in the middle of the transition diagram). Now looking for the other transition path: from ″00″ to ″10″ (following the orange arrow in the transition diagram of Fig. 4.11). The output would give ″11″ (orange box in the middle). Now back to Fig. 4.12 the decoder then needs to make a decision which path is more likely. This is done by simply comparing the theoretical output for this transition with the actual received data (shown at the bottom). In this case, the received bit string is ″00″; and the two outputs that we have to choose from are either ″00″ or ″11″. The decoder calculates the Hamming distance between the received bit string ″00″ and the possible bit strings ″00″ and ″11″. The Hamming distance is the bit difference. It is zero for a transition from ″00″ to ″00″ (as zero bits have flipped), it is two for ″11″ to ″00″ (as two bits have changed), and one for a transition from ″10″ to ″11″ (as only the last bit has flipped). A high value for the Hamming distance means that the received and possible bit string are more different and therefore less likely. The path with the highest Hamming distance is ignored, since this is the less likely path. The above steps are repeated until the end and the Hamming distances are added together for every path. In this case, the final Hamming distance is zero, which indicates that there was no errors in the received code.

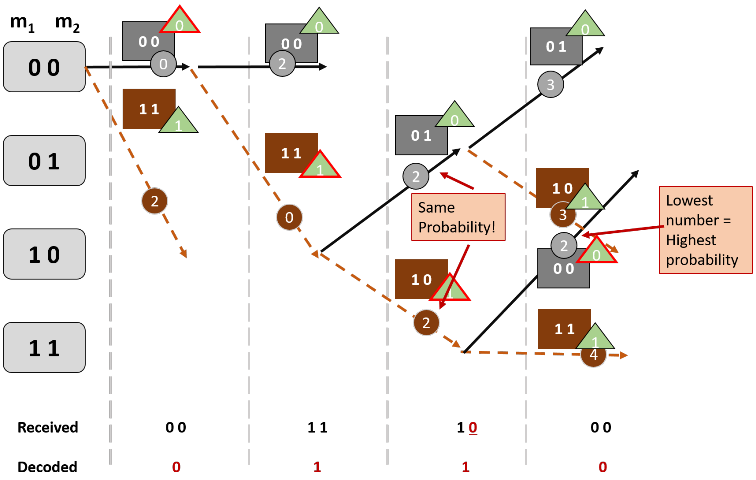

FIGURE 4.13: Trellis diagram using the Viterbi algorithm. This time with erroneous data. The Hamming distance is used for the decision making on the decoder.

Fig. 4.13 shows the case for an erroneous code. The starting point is again at 00. From there, there are two options according to the transition diagram in Fig. 4.11, namely either to 10 or to 00. Since the output, which is in the end what we receive, is 00 in the case of the 00-00-transition, and the bit sequence that we receive is also 00, the Hamming distance is zero and therefore we do not need to consider the other path. In the next step, we again have the choice between 00-00 or 00-10. Now however, we receive 11, and the output for the 00-11 transition is just 11. Hence again, the Hamming distance is 0+0=0 and we do not need to consider the other path. The next bit sequence that we receive is 11. There are two paths from 10-01 and from 10-11. The transition 10-01 gives and output of 01, and the transition 10-11 results in 10. Both paths have now a Hamming distance of 1 to the received sequence. This means those two paths have the same likelihood and the receiver needs to decide which one is the correct path. To make this decision, the next paths need to be considered. At the end, the Hamming distance of the four paths can be calculated by summarising the Hamming distance on each node. The path ending at 01 shows with one the lowest Hamming distance. The decoded sequence can then be extracted by following the track backwards from transition 01-11-10-00. This gives then the decoded and error corrected sequence 0-1-1-0.

Convolutional codes can be designed to purpose with a higher number of error correction bits for systems prone to errors. So the question for EROS remains: how many error correction bits are required and how long will the resulting fibre then be? Although one might think this should be a straightforward question to answer, it will be seen that a design decision of the beginning has a detrimental impact on the error correction possibility of the final device.

The reason why error correction is so difficult to implement in the EROS device is due to the conversion from a non-binary *Spectrum* matrix to a binary *Encoding* matrix. The

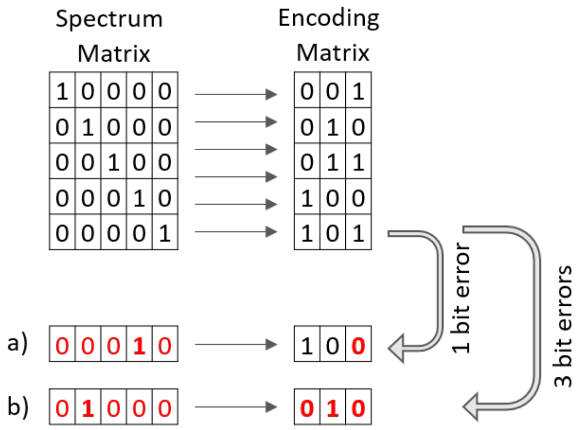

FIGURE 4.14: This illustration shows the different effects a single incorrectly read out grating can have. On the left is the *Spectrum* matrix, on the right the *Encoding* matrix. This diagram shows the effect of *one* grating being read out incorrectly. The first example marked with a) shows that if the last grating is moved forward by one position in the *Spectrum* matrix, the readout has a one-bit error in the encoding matrix. In the other example, marked with b), a grating on the second place was read out instead of the grating on position 5. This results in a three bit error, so the whole sequence to be incorrect.

size of these matrices define the storage capability, so the larger the bit stream in one row on the *Encoding* matrix, the more data can be stored on one location. The problem then is what happens if one grating is read out incorrectly. Fig. 4.14 is used to describe this in an example. Suppose there are five spectral bins and one grating (so the *Spectrum* matrix consists of five columns and five rows). The spectral position of a grating was defined in the final spectral bin, at the longest wavelength, such that the respective row in the *Spectrum* matrix would be 0-0-0-0-1, and in the *Encoding* matrix ″101″. During interrogation, it was however read out to be in the second to last spectral bin: 0-0-0-1-0, shown in red. This corresponds to ″100″ in the *Encoding* matrix. In terms of errors, deviation from the original position, it would be ″101″ (original position) - ″100″ (incorrectly read out position) results in 1 bit error. If the grating however was read out to be in the second spectral bin: 0-1-0-0-0, as shown in the second red row, the deviation from the original bit string would be 3. Therefore a single shift in grating position has different effects on the *Encoding* matrix. Therefore, since the worst case scenario is an inversion of all bits, it generally has to be assumed that all bits in the *Encoding* matrix could be incorrect.

For the expectation that 100 spectral bins, 20 superpositions and 6 grating types can be inscribed, 120 bits can be stored in one spatial location (120 bits is the number of bits in one row of the *Encoding* matrix). If one grating in this location is read out incorrectly, the whole 120 bit stream might be incorrect. Error correction then cannot be done as there is a maximum limit on how many erroneous bits are correctable per data bits. This is dependent on the error correction algorithm. A workaround to avoid all bits on one location to be incorrect is interleaving as explained above. As five spatial locations are needed to store the whole data file, the five sections can be interleaved such that assuming only one out of the five locations is incorrect, only every fifth bit is erroneous.

This has been tested for different amounts of errors with different trellis structures to cast some light on the encoding mechanisms as described in the following section, but it should be noted that this goes beyond the scope of this thesis and was implemented more to give a starting point for future research that potentially follows up on the findings of this thesis. There are three parameters that change the design of a trellis structure: the number of input bits, the number of output bits and the number of memory registers. The input and memory bits are combined to form the constraint length of a trellis, which defines the delay of input bits into the encoder. The relation between the memory registers and the outputs defines the generator polynomials. The constraint length and the generator polynomial define the design and function of a trellis and therewith also the code rate, the ratio between the data bits that are fed into the encoder and encoded bits at the output of the encoder. Or in other words, how many data bits per correction bits (also known as parity bits) are used.

To evaluate the correction capacity of a convolutional code for the EROS project, three trellis designs with high correction capabilities and different code rates were compared [78]. The code rates were set to 1/2 (one input bit is convoluted into two output bits), 1/3 (one input bit is convoluted into three output bits), and 1/4 (one input bit is convoluted into four output bits). The data string of EROS is 492 bits in length. After the data bits were encoded, the output strings vary dependent on the code rate of the trellis structure. A 1/2 code rate results in a 984 bit string, a 1/3 code rate in a 1,476 bit string and a 1/4 code rate returns a 1,968 long bit string. After the encoding, random bit error are introduced into the encoded bit string, before the decoding takes place. The error correction capability of the trellis is evaluated by comparing the original data string before the encoder (492 bits) with the decoded message after the decoder (492 bits). Fig. 4.15 a) shows the remaining (uncorrected) errors over the induced errors for a code rate of 1/2, 1/3, 1/4. It should be noted that the code was run 300 times for each simulation after which the average was taken to accommodate for generating random data and error strings. The 1/2 code rate corrects fully for up to 31 induced errors, the 1/3 code for up to 91 and the 1/4 code for up to 201 induced errors. The whole data string to store the calibration data is 492 bits long and the data is stored over 5 locations. If the 492 bits are distributed evenly over the spatial distance, there will be 99 bits stored per spatial location. If one grating on one location is read out incorrectly, a worst case could be that the binary string is reversed and all 99 bits in this location are erroneous. Assuming that all other locations are read out correctly, the number of errors in the whole data storage would be 99. The burst error from one location can be interleaved with the bits from the other locations to distribute the burst. Fig. 4.15 b shows that the convolutional codes with a code rate of 1/2 and 1/3 expect to have no error remaining for up to 25 and up to 75 induced errors, and the code with a code rate

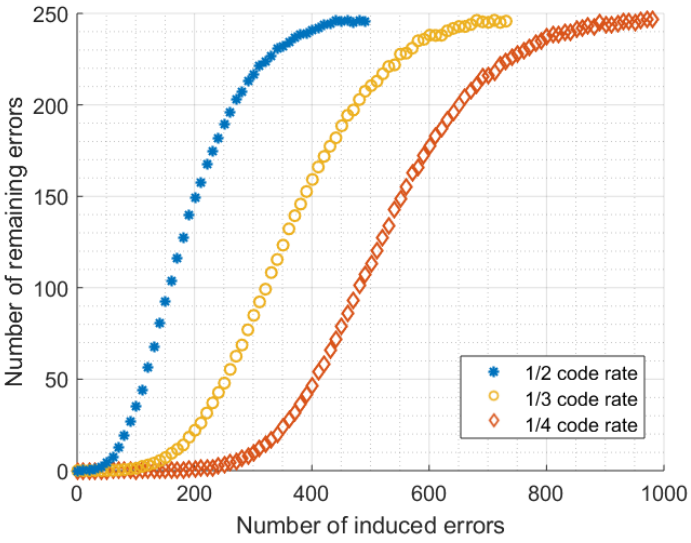

(a)

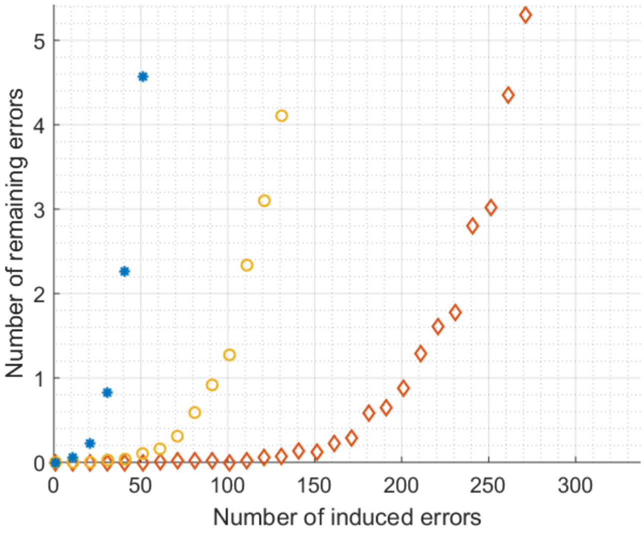

(b)

FIGURE 4.15: a) The number of remaining errors after correction over the number of induced errors. The plots show the results of convolutional codes with different code rates: 1/2, 1/3, 1/4. The code rate is the ratio between data bits that are fed into the encoder and convoluted output stream of after the encoding. b) Zoom into the figure to visualise the number of induced errors for a small single digit number of remaining errors. Fractional numbers are possible due to averaging over 300 random number simulations.

of 1/4 can provide error-free data for a total of 175 induced errors. For the example of having one erroneous location, the 1/4 code would be able to fully correct.

Although a higher code rate is able to correct the error if the bit stream of one location is erroneous, the additional parity bits come at a cost such that the message to be encoded is four times as long. This also means that the likelihood of reading out a grating incorrectly and therefore risking the whole bit stream to be erroneous is higher. The length of fibre required to store the coded data has increased to 17 cm with the addition of error correction bits.

In the discussion of error correction, it should also be noted that a complete correction (zero residual error) is critical for the encoding. This is due to the choice of converting the file as a whole into binary. A single bit error leads to the whole file and therefore all of the calibration data to be potentially incorrect. If instead of converting the whole file into binary, only each individual digit was converted into binary, a single bit error would result only in one digit of the calibration data to be incorrect. As shown in Fig. 4.3, the increase of bits to be stored increases from 492 bits for the whole file to 592 bits for the individual digits. So the cost of converting the digits individually is only 100 bits, so about one spatial location in the fibre. This consequently means that if one error is uncorrected, only one digit in the file is affected and not the file as a whole. It would therefore be advised to restrain from the more efficient approach of converting the file as a whole and rather converting them individually. In addition, further work on creating a *Spectrum* matrix that is inherently less prone to errors should be pursuit. It should also be noted that not every digit in the calibration file carries the same importance, which could be taken into account for the error correction algorithm in the future.

Another way of error correction is to write the message multiple times [79]. The sequence that occurred most often is the most likely message. This technique is called repetition coding. Repetition coding is simple, intuitive and powerful. It is commonly used for example in aerospace during a pan-pan call in emergency situations. Aircraft communication lines can get disturbed; repeating "pan-pan" three times in an emergency situation increases the likelihood of one of the "pan-pan" being transmitted and heard by controllers. The benefit if this technique compared to the other techniques mentioned above is that the errors can be corrected where they occur: in the *Spectrum* matrix during the read out. By reading the gratings and comparing grating type and position with the other identical sequences, the errors are corrected before being translated into a binary sequence. This mitigates the concern that one error in the *Spectrum* matrix could cause the complete binary string in the *Encoding* matrix to be incorrect, as the *Spectrum* matrix sequence should be error-free. It should be noted that this, of course is not a binary error correction scheme, however, it is better suited for this case and is expected to result in a lower number of errors. Further work could explore a suitable repetition rate after analysing the type of errors that are expected to occur outside a laboratory environment.

4.5 Conclusion

This chapter was the last of the three pillars, the keystone that builds the bridge from the numbers in a spreadsheet to grating features in an optical spectrum.

There are different ways to convert floating point numbers into binary, but they are not necessarily the most efficient when analysing the constraints and boundaries of the data. Therefore a different way of transforming the calibration data into a binary string has been found. To create the most compact data storage, the decimal digits of all numbers in the calibration file were concatenated to one large number. This was then converted into a binary string, the data string. With this method, the efficiency is increased by approximately 17% compared to storing the data as individual digits and compared to the IEEE 754 - 64 bit floating point conversion standard, it is approximately 79% more efficient. This of course comes at a cost and in this example the precision of the developed conversion scheme is lower than the IEEE 754 - 64 bit standard.

The encoding scheme itself consists of two matrices: the *Spectrum* matrix, which entails the spectral representation and the *Encoding* matrix, which represents the row number in a binary format and is always shorter than the *Spectrum* matrix. The *Spectrum* matrix consists of all combinations on how the gratings can be arranged in the spectral space and is therefore dependent on the spectral space itself (the spectral bins), the number of superpositions and the number of grating types. The largest improvement on data density or in other words on the shortness of the fibre required to store the whole calibration file, can be achieved by increasing the number of superpositions. For 20 superimposed gratings with a length of 5 mm, 6 different grating types and 100 spectral bins, a length of 5 cm is required to store the calibration file, considering a spatial spacing of 5 mm between each grating section.

Apart from number conversion and the encoding scheme itself, the topic of error handling was described in this chapter. Error handling is very important for the final device and with higher requirements for error correction, higher demand for capacity arises. It was shown that a convolutional code with a code rate of $1/4$ can correct for one erroneous location, but at a cost of adding four times as many bits as parity bits for correction. It was also noted that although converting the whole calibration file is more efficient, converting the digits individually reduces the impact of errors to the whole calibration data file, as a single bit error would only potentially affect a single decimal digit rather than the whole file. With repetition coding, an alternative way has been proposed to identify the correct message based on the frequency of its occurrence. This correction can be implemented in the *Spectrum* matrix, at the most likely source of error. It is expected to perform better than other error correction techniques discussed in this chapter.

In the end, the type of error correction required, depends on the type of errors encountered, which can only be evaluated outside the lab environment, with vibration, temperature, humidity and pressure close to what it is expected during flight. Future work should also be conducted to analyse the statistical probability of different grating types to be read out incorrectly, as it can be assumed that certain types are more likely to be read wrongly. To come to a conclusion of which error correction scheme should be implemented, the errors needs to be better understood in form of further testing of use cases. This is can be investigated in a future project, but is not part of this thesis.

Chapter 5

Conclusion

The aim of project EROS was to realise an in-fibre environmentally robust optical storage for aerospace applications. The device should be capable of storing calibration data for sensors, which consists of 37 floating point numbers. The proposed solution is a passive optical device, which is based on fibre Bragg gratings, periodic refractive index changes in the core of a fibre, that reflect a certain wavelength of light depending on their design.

This project was divided up into three pillars:

- Fabrication: the inscription of Bragg gratings into a fibre.
- Interrogation: the read out of the Bragg gratings.
- Encoding: the conversion of the calibration data into Bragg gratings.

Although each of the pillars can be seen as a standalone chapter, they were developed in a concurrent way with each new bit of information from one pillar being fed back into the remaining two and vice versa.

The manufacturing of the Bragg gratings was described in the fabrication chapter. The small spot direct UV writing technique was used to inscribe the gratings into single mode fibres. This method uses a small spot, composed of focused and recombined light from two arms of an interferometer. This spot therefore contains interference fringes, which were used to define the grating planes of the Bragg gratings.

Three different fibres were used as the basis of the storage device: SMF28, a standard telecommunication fibre, GF4A a cladding mode offset fibre and PS-PM980, a photosensitive polarisation maintaining fibre. Besides these three main candidates, there was another fibre that was considered due to its unique features: multicore fibre. The multicore fibre however was not further considered due to poor grating performance, caused by lensing and shadowing effects of neighbouring cores, and due to the necessity of hydrogen loading. From the three single core fibres, only SMF28 requires hydrogen loading. The problem with hydrogen loading is that the hydrogen outgases with time, which means that the writing process is time limited. Superimposed gratings, a key requirement found for the storage device is therefore considered problematic with hydrogen as subsequent would promote hydrogen out-diffusion thus a reduction and limitation in sensitivity. Good results have been achieved with GF4A and PS-PM980, both inherently photosensitive fibres.

The small spot UV writing technique is a unique grating inscription technique, which allows grating definition in a wide detuning range. But since the gratings are inscribed with only several planes at a time, it is not possible to classify the gratings in a conventional way, by monitoring the spectral response of the whole grating during fabrication. With thermal classification, grating written with the small spot direct UV writing technique has been characterised for the first time. With this understanding it was then possible to find the right grating type to withstand thermal challenges of an aerospace environment and to put these gratings into the widely defined framework of Bragg grating types.

Another key requirement for a successful optical storage device with fibre Bragg gratings is spatial co-location. Two different ways to achieve this were presented:

- Superimposed gratings: where gratings are defined in consecutive writing steps.
- Superstructured gratings: where the grating planes are calculated upfront and the co-located gratings are written in one go.

Co-located gratings have been around for almost 40 years, however, they have not been fabricated with the small spot direct UV writing technique before. Within this project 45 superimposed and 44 superstructured gratings were inscribed in a fibre. Both techniques appear to be comparable in their fabrication precision and therefore equally well suited for fabrication. It was however decided to fabricate superimposed gratings with the consecutive writing technique as it was a more straight forward approach with a drawback of taking a couple of minutes longer for the writing, but also with greater flexibility in the grating definition.

The fluence, besides grating length, is another important parameter for fabrication. It defines the velocity of the fibre movement based on the measured laser power and therefore sets the exposure of the fibre core. A fluence of $1\,kJ/cm^2$ resulted in the best trade-off between grating strength for a given grating length of 5 mm and possibility to superimpose gratings, as writing gratings with a high fluence reduces the amount of gratings that can be written at the same location. This postulated to be due to thermal effects within the fibre induced by long exposure times of the laser.

Since superimposing has an effect on already inscribed gratings, experiments to find the number of superpositions for which the effect on already inscribed gratings were as low as possible, while the reflection strength of newly inscribed gratings were sufficiently high. For 5 mm long gratings, this number was set to 20, which formed the default value for superpositions in the encoding scheme.

Two different types of interrogation for the EROS device have been suggested:

- Spectral interrogation: where the spectral response of the grating is evaluated and all information is stored in the spectral domain.
- Optical Frequency Domain Reflectometry: where the spectral and spatial information of the gratings are considered.

The final decision was based on the fact that not all data could be stored spectrally and by using both spectral and spatial information, a higher data density could be achieved. The OFDR system allows to hone in on different spatial positions, which allows a spectral grating analysis on individual points along the fibre.

An analysis of different grating types revealed that the OFDR system is capable of distinguishing between different grating types: uniform, Gaussian apodised, π-phase shift, 100 π-phase shift and 100 π-phase shift with a shifted dip at 2/3 and at 2/3 in the spatial domain.

The interrogation chapter also covers two prototypes that have been inscribed with two different encoding schemes: a non-binary encoding scheme and a binary encoding scheme. This leads to the final chapter in this thesis, the encoding chapter. This chapter has more of a computer science outlook and focuses on data conversion, a model that determines the parameter with the most impact on the grating length and on strategies to correct or reduce the impact of errors.

The calibration data file, provided by Parker Aerospace consisted of 37 floating point numbers. The IEEE 754 standard, a standard commonly used to convert these floating point numbers into binary did not provide a valuable solution, as the converted binary string was too long to be stored in the fibre with the presented technique. A new conversion scheme was developed, which allowed the choice of two different precision: short and long. For the short data format, the final binary string was reduced by approximately 80% compared to the IEEE 754 64 bit conversion format.

The number conversion however was not the only part of the encoding chapter. This chapter also analysed how to translate the binary sequence into a spectral representation. This might seem straightforward to begin with, as the presence of a grating could be seen as a binary ”1” and the absence as a binary ”0”, but that would require that all spectral position could be filled with a grating. In the example of 100 spectral bins, it would require the superposition of 100 gratings. But so far, only 45 gratings have been superimposed. Instead, a *Spectrum/Encoding* matrix pair have been created, which allowed the spectral sequence measured by the OFDR to be allocated a binary string. This look-up method allowed the transformation from the binary data into a spectral representation.

There are different parameters that influence the amount of data that can be stored in a certain length:

- Superposition: The amount of gratings that are inscribed on one spatial location.
- Spectral bins: The number of spectral bins that are available for inscription. This depends on the bandwidth of the laser (or the available spectrum) and the bandwidth of the gratings.
- Grating type: Different grating types allow a higher order of encoding - away from the binary 1=grating, 0=no grating.

The encoding chapter looked at the relationship between these parameters. A model has been developed to define the parameter with the greatest influence on the required fibre length. The most important parameter in that regard is superposition, followed by the grating types. The amount of spectral bins appear to have less of an impact on the required fibre length. The default parameter values for the above mentioned parameters were: 100 spectral bins, 20 superpositions and 6 grating types. These are all values that have been individually practically proven to be possible. With these parameter values, the full calibration file can be stored in the short data conversion format in 5 cm of fibre.

Storing all data bits however is only one part of the story, as additional bits are required to correct for potential errors that occur during read out. In the encoding chapter it was explained that by converting the whole file into a single bit string requires fewer bits and is therefore more efficient, but it also makes the storage more susceptible to errors. If only one bit in the single string is incorrect, the whole file read out (or at least everything that comes after the error) is incorrect. This is why it should be considered to convert individual digits of the calibration file instead, which costs more storage but provides a more stable and secure data storage.

In regards to error handling, different convolutional codes have been investigated. The code rate of an error correction code is defined as the ratio between input data and output string (data + error correction bits). The smaller the code rate, the more error correction bits are added. The way EROS was designed meant that reading out a single grating incorrectly could, in a worst case, cause the whole bit string on this location to be inverted. Without getting into the depth of analysing optimisation algorithms, it was also shown that a certain convolutional code with a code rate of 1/4 was able to correct sufficient errors in case one of the locations was read out incorrectly and resulted in the whole bit string to be erroneous. It should be noted that the technique of interleaving was also utilised to spread out this burst error into bit errors along the encoded bit string.

A final prototype which included the actual calibration data was unfortunately never inscribed. Instead, multiple prototypes, or pilots were written with the Declaration of Independence. These were successfully inscribed and 94% of the gratings were read out correctly.

Last but not least there are a few words on how this project could be carried further, things that can be further explored, but do not necessarily fall into the scope of this thesis:

- Environmental simulation: Two fibre samples were sent to the Parker Aerospace testing lab to evaluate the spectral performance during a cyclic test. Analysing this data provides a good insight into the lifetime of the EROS device and potential issues with different grating types.
- Vibration study: Although initial experiments have been carried out suggesting that excessive vibration cause limitations in the data acquisition, further research to the extend and comparability with aeronautic environments would give a conclusive answer on whether or not vibration repressing packaging is required. Further to this, a machine learning algorithm was implemented to classify vibrational modes of a cantilever, by measuring the spectral response of Bragg gratings in an optical fibre, attached to the cantilever. It would be interesting to see if it is possible to remove the effects of vibration on the OFDR trace to retrieve correct data even during strong vibrations.

This thesis showed that it is possible to store the calibration file of an optical sensor in an optical storage device based on fibre Bragg gratings. Different writing techniques have been explored, different read out systems analysed and conversion techniques developed. To evaluate the application suitability it is important to evaluate and explore environmental constraints, which is future work that can be investigated further in a future project.

Resulting from this PhD project, a total of 3 peer reviewed journal publications and 9 conference proceedings were made as first author. One further peer reviewed journal publication and 10 conference proceedings were made as co-author. A list of these publications can be found in Appendix A.

Appendices

Appendix A

Publication List

First Author

Senta L Jantzen, Devin Smith, Rex Bannerman, Lewis Boyd, James Gates, Peter Smith, Christopher Holmes, Inscription methods for co-located fiber Bragg gratings using small spot direct UV writing, Electronics Letters, 2021.

Senta L Jantzen, Rex Bannerman, Alexander Jantzen, Paolo Mennea, Devin Smith, James Gates, Mohammed El-Hajjar, Lewis Boyd, Peter G R Smith and Christopher Holmes, Individual inscription of spectrally multiplexed Bragg gratings in optical multicore fiber using Small Spot Direct UV Writing, Optics Express, 2020.

Senta L Jantzen, Devin Smith, Rex Bannerman, Paolo Mennea, Lewis Boyd, Peter Smith and Christopher Holmes, Fabrication of more than 40 Superimposed and Superstructured Fiber Bragg Gratings, IEEE IPC, 2020.

Senta L Jantzen, Jiarui Yu, Peter Smith and Christopher Holmes, Using k-Nearest Neighbor Algorithm to Identify Mechanical Vibrational Modes of a Cantilever with Spectrally Multiplexed Fiber Bragg Gratings, Advanced Photonics Congress, 2020.

Senta L Jantzen, Devin Smith, Rex Bannerman, Paolo Mennea, Lewis Boyd, Peter Smith and Christopher Holmes, Superstructure and Superimposed Fiber Bragg Gratings Fabricated through Small Spot Direct UV Writing, CLEO Pacific Rim, 2020.

Senta L Jantzen, Jiarui Yu, Peter Smith and Christopher Holmes, Identifying Mechanical Vibration Modes of a Cantilever Using Spectrally Multiplexed Bragg Gratings and

Machine Learning, CLEO Pacific Rim, 2020.

Senta L Jantzen, Rex Bannerman, Alexander Jantzen, Paolo Mennea, Devin Smith, James Gates, Mohammed El-Hajjar, Lewis Boyd, Peter G R Smith, and Christopher Holmes, Individual inscription of fibre Bragg gratings in multicore fibre using small-spot direct UV writing, The International Photonics and Optoelectronics Meeting (POEM), Wuhan, China, 2019.

Senta L Jantzen, Rex Bannerman, Alexander Jantzen, Sam Berry, Alan Gray, James Gates, Lewis Boyd, Peter Smith, and Christopher Holmes, Integrated optical fibre – Investigating the vibrational response using optical frequency domain reflectometry, The European Conference on Lasers and Electro-Optics (CLEO), Munich, Germany, 2019.

Senta L Jantzen, Rex Bannerman, Alexander Jantzen, Paolo Mennea, Devin Smith, James Gates, Mohammed El-Hajjar, Lewis Boyd, Peter Smith and Christopher Holmes, Small-spot direct UV written fiber Bragg gratings in multicore fiber, IEEE Avionics and Vehicle Fiber-Optics and Photonics Conference (AVFOP), Arlington, USA, 2019.

Senta L Scholl, Alexander Jantzen, Rex Bannerman, Paul Gow, Devin Smith, James Gates, Lewis Boyd, Peter Smith and Christopher Holmes, Thermal approach to classifying sequentially written fiber Bragg gratings, Optics Letters, 44 (3), 2019.

Senta L Scholl, Alexander Jantzen, Rex Bannerman, James Field, James Gates, Lewis Boyd, Peter Smith and Christopher Holmes, Classification of small-spot direct UV written fiber Bragg gratings through extreme thermal treatment, OSA Advanced Photonics Congress, Zurich, Switzerland, 2018.

Senta L Scholl, Thalia Dominguez Bucio, Mehdi Banakar, Ali Khokhar, Scott Reynolds, Graham Reed, and Frederic Gardes, Flat-top spectral response angled multimode interferometer (AMMI), Photonex Europe, Coventry, UK, 2017.

Co-Author

Christopher Holmes, Mike Godfrey, Paolo Mennea, **Senta L Jantzen**, Daniel Bull, Janice Dulieu-Barton, Flexible Photonics Embedded into Advanced Composites, Conference on Lasers and Electro-Optics Europe and European Quantum Electronics Conference

(CLEO/Europe-EQEC), 2021.

Frederic Gardes, Thalía Domínguez Bucio, Lorenzo Mastronardi, Greta De Paoli, **Senta L Jantzen**, Ilias Skandalos, Milan Milosevic, Valerio Vitali, Joaquin Faneca, Periklis Petropoulos, Francisco Jurado Romero, José Manuel Luque-González, Iñigo Molina-Fernández, Robert Halir, Alejandro Ortega-Moñux, JG Wangüemert-Pérez, Daniele Melati, Jens Schmid, Pavel Cheben, Tunable index silicon nitride for CMOS photonics applications, Integrated Optics: Devices, Materials, and Technologies XXV, 2021.

Andrea Annunziato, A Erario, Francesco Anelli, Gianluca Abbate, Michael Godfrey, **Senta L Jantzen**, James Gates, Christopher Holmes, Caterina Ciminelli and Francesco Prudenzano, Structural Health Monitoring of Composite Laminate for Aerospace Applications via Embedded Panda Fiber Bragg Grating, International Conference on Transparent Optical Networks (ICTON), 2020.

Francesco Anelli, Gianluca Abbate, **Senta L Jantzen**, James Gates, Christopher Holmes, Francesco Prudenzano, Design of Longitudinal Strain and Temperature Fiber Bragg Grating Sensor in Polarization-Maintaining Panda Fiber, International Conference on Transparent Optical Networks (ICTON), 2020.

Greta De Paoli, **Senta L Jantzen**, Thalia Dominguez Bucio, Ilias Skandalos, Christopher Holmes, Peter Smith, Milan Milosevic and Frederic Gardes, Laser trimming of the operating wavelength of silicon nitride racetrack resonators, Photonics Research, 2020.

Frederic Gardes, Thalia Domınguez Bucio, Greta de Paoli, Stefan Ilie, Ilias Skandalos, Cosimo Lacava, Milan Milosevic, **Senta L Jantzen**, Ali Khokhar, Periklis Petropoulos, Tunable index silicon nitride for extended silicon photonics applications, Asia Communications and Photonics Conference, 2019.

Alexander Jantzen, Paul Gow, **Senta L Jantzen**, Lewis Boyd, Peter Smith and Christopher Holmes, Laser-based fabrication of micromechanical diaphragms for pressure sensing using Bragg Gratings, The European Conference on Lasers and Electro- Optics (CLEO), Munich, Germany, 2019.

Christopher Holmes, **Senta L Jantzen**, Naruo Yoshikawa, Russell Minns, Daniella Hares, Giulio Cupilari, Alan Gray, Devin Smith, James Gates, William Brocklesby, Christopher

Wood, Jeremy Frey, Peter Smith, Mapping water contamination of jet fuel, IEEE Avionics and Vehicle Fiber-Optics and Photonics Conference (AVFOP), Arlington, USA, 2019.

Alexander Jantzen, Paul Gow, Alan Gray, **Senta L Scholl**, James Gates, Peter Smith, Lewis Boyd, and Christopher Holmes, Pressure sensing based on ratiometric Bragg grating loss in a planar silica diaphragm platform, Advanced Photonics Congress, Zurich, Switzerland, 2018.

Christopher Holmes, Paul Gow, Alexander Jantzen, Alan Gray, **Senta L Scholl**, James Gates and Peter Smith, High temperature operation of integrated optical fiber, Conference on Lasers and Electro-Optics/Pacific Rim (CLEO-PR), Hong Kong, 2018.

Thalia Dominguez Bucio, **Senta L Scholl**, Stephan Ilie, Cosimo Lacava, Kapil Debnath, Ali Khokhar, Mehdi Banakar, Moise Sotto, Katarzyna Grabska, Marco Clementi, Daniele Bajoni, Matteo Galli, Shinichi Saito, Periklis Petropoulos and Frederic Gardes, Low-temperature NH3-free silicon nitride platforms for integrated photonics, IEEE 15th International Conference on Group IV Photonics (GFP), 2018.

Appendix B

Calibration Data

TABLE B.1: Calibration data provided by Parker Aerospace.

Count	Number
1	3002
2	7.0400E-01
3	4.2488E-01
4	3.2900E-05
5	-1.6200E-05
6	-4.9100E-06
7	6.3400E-06
8	-1.0500E-05
9	-1.3200E-04
10	1.6900E-05
11	-6.8000E-06
12	1.4500E-05
13	-1.0700E-03
14	-1.9700E-05
15	-8.6300E-06
16	4.2900E-05
17	6.9500E-05
18	3.0900E-03
19	5.9500E-05
20	3.0100E-07
21	-3.1100E-04
22	7.6000E-04
23	-9.1600E-03
24	-9.9900E-01
25	1.1800E-03
26	-1.1800E-04
27	-3.3000E-03
28	-1.1600E-04
29	4.8100E-04
30	1.8000E-02
31	-1.6400E-03
32	8.1054E+00
33	4.2708E+01
34	1.8100E-02
35	-6.1700E-02
36	9.7500E-01
37	5.9300E-02

Bibliography

[1] S. L. Scholl, A. Jantzen, R. H. S. Bannerman, P. C. Gow, D. H. Smith, J. C. Gates, L. J. Boyd, P. G. R. Smith, and C. Holmes. Thermal approach to classifying sequentially written fiber Bragg gratings. *Optics Letters*, 44(3):703–706, 2019.

[2] J. Canning. Fibre gratings and devices for sensors and laser. *Laser and Photonics Reviews*, 2(4):275–289, 2008.

[3] International Civil Aviation Organization Civil Aviation Statistics of the World and ICAO. www.data.worldbank.org/indicator/is.air.psgr. Accessed on 10 November 2021.

[4] International Air Transport Association (IATA). International Air Transport Asssciation - Annual Review 2020. Technical report, 2020.

[5] V. Grewe, A. G. Rao, T. Grönstedt, C. Xisto, F. Linke, J. Melkert, J. Middel, B. Ohlenforst, S. Blakey, S. Christie, S. Matthes, and K. Dahlmann. Evaluating the climate impact of aviation emission scenarios towards the Paris agreement including COVID-19 effects. *Nature Communications*, 12(1):1–10, 2021.

[6] A. Kharina and D. Rutherford. Fuel efficiency trends for new commercial jet aircraft: 1960 to 2014. *White Paper, The International Council on Clean Transportation*, (8):27, 2015.

[7] European Commision. *Flightpath 2050*. Publications Office of the European Union, 2012.

[8] International Air Transport Association (IATA). Press Release 66: Net-Zero Carbon Emissions by 2050, 2021.

[9] R. Di Sante. Fibre Optic Sensors for Structural Health Monitoring of Aircraft Composite Structures: Recent Advances and Applications. *Sensors*, 15(8):18666–18713, 2015.

[10] K. Diamanti and C. Soutis. Structural health monitoring techniques for aircraft composite structures. *Progress in Aerospace Sciences*, 46(8):342–352, 2010.

[11] B. Culshaw and A. Kersey. Fiber-Optic Sensing: A Historical Perspective. *Journal of Lightwave Technology*, 26(9):1064–1078, 2008.

[12] Z. Ding, C. Wang, K. Liu, J. Jiang, D. Yang, G. Pan, Z. Pu, and T. Liu. Distributed optical fiber sensors based on optical frequency domain reflectometry: A review. *Sensors*, 18(4):1–31, 2018.

[13] J. Li, J. Gan, Z. Zhang, X. Heng, C. Yang, Q. Qian, S. Xu, and Z. Yang. High spatial resolution distributed fiber strain sensor based on phase-OFDR. *Optics Express*, 25(22):27913, 2017.

[14] Komite Nasional Keselamatan Transportasi Republic of Indonesia. Final Aircraft Accident Investigation Report - KNKT 18.10.35.04. 2019.

[15] Federal Aviation Administration. Summary of the FAA's Review of the Boeing 737 MAX - Return to Service of the Boeing 737 MAX Aircraft. *Report*, 2020.

[16] A. Jantzen. *The Design, Fabrication and Development of Micromechanical Integrated Optical Pressure Sensors for Aerospace*. PhD thesis, 2019.

[17] H. Peek, J. Bergmans, J. van Haaren, F. Toolenaar, and S. Stan. *Origins and Successors of the Compact Disc - Contributions of Philips to Optical Storage*. Springer Verlag, 2009.

[18] R. Kashyap. Optical Memory, U.S. Patent Number 5 530 666 Jun. 25, 1996.

[19] S. Keren, E. Brand, Y. Levi, B. Levit, and M. Horowitz. Data storage in optical fibers and reconstruction by use of low-coherence spectral interferometry. *Optics Letters*, 27(2):125–7, 2002.

[20] M. A. Englund, L. G. Edvell, and A. Graf. Method of Optical Data Storage, U.S. Patent Application Number, 2007/0277191A1, 2007.

[21] M. Castiglioni and D. D. Favero. OLiD: Diamond's FBG Network Monitoring System. *White Paper*, 2015.

[22] Diamond SA. Optical line identification www.diamond-fo.com/technologies/technology/optical-line-identification-olid. Accessed on 05 September 2021.

[23] T. A. Goebel, M. Weissflog, R. G. Krämer, M. Heck, D. Richter, and S. Nolte. Tuning multichannel filters based on FBG in multicore fibers. *Procedings of SPIE, Frontiers in Ultrafast Optics: Biomedical, Scientific, and Industrial Applications*, 10908, 2019.

[24] O. V. Butov, A. P. Bazakutsa, Y. K. Chamorovskiy, A. N. Fedorov, and I. A. Shevtsov. All-fiber highly sensitive bragg grating bend sensor. *Sensors*, 19(19):1–9, 2019.

[25] C. Holmes, S. Ambran, P. Cooper, A. Webb, J. C. Gates, C. B. E. Gawith, J. Sahu, and P. G. R. Smith. Bend monitoring and refractive index sensing using flat fibre and multicore Bragg gratings. *Measurement Science and Technology*, 31:1–6, 2020.

[26] M. Amanzadeh, S. M. Aminossadati, M. S. Kizil, and A. D. Rakić. Recent developments in fibre optic shape sensing. *Measurement: Journal of the International Measurement Confederation*, 128:119–137, 2018.

[27] K. O. Hill, Y. Fujii, D. C. Johnson, and B. S. Kawasaki. Photosensitivity in optical fiber waveguides: Application to reflection filter fabrication. *Applied Physics Letters*, 32(10):647–649, 1978.

[28] G. Meltz, W. W. Morey, and W. H. Glenn. Formation of Bragg gratings in optical fibers by a transverse holographic method. *Optics Letters*, 14(15):823, 1989.

[29] K. O. Hill, B. Malo, F. Bilodeau, D. C. Johnson, and J. Albert. Bragg gratings fabricated in monomode photosensitive optical fiber by UV exposure through a phase mask. *Applied Physics Letters*, 62(10):1035–1037, 1993.

[30] W. H. Loh, M. J. Cole, M. N. Zervas, S. Barcelos, and R. I. Laming. Complex grating structures with uniform phase masks based on the moving fiber–scanning beam technique. *Optics Letters*, 20(20):2051, 1995.

[31] B. Malo, K. Hill, F. Bilodeau, D. C. Johnson, and J. Albert. Point-by-point fabrication of micro-Bragg gratings in photosensitive fibre using single eximer pulse refractive index modification techniques. *Electronics Letters*, 29(18):1668–1669, 1993.

[32] A. Martinez, M. Dubov, I. Khrushchev, and I. Bennion. Direct Writing of Fibre Bragg Gratings by Femtosecond Laser. *Electronics Letters*, 40(19), 2004.

[33] G. D. Marshall, R. J. Williams, N. Jovanovic, M. J. Steel, and M. J. Withford. Point-by-point written fiber-Bragg gratings and their application in complex grating designs. *Optics Express*, 18(19):19844, 2010.

[34] A. Ghatak and K. Thyagarajan. *Introduction to fiber optics*. Cambridge University Press, 2007.

[35] E. Udd and W. B. Spillman. *Fiber Optic Sensors: An Introduction for Engineers and Scientists*. John Wiley and Sons, 2011.

[36] D. Gloge. Weakly Guiding Fibers. *Applied Optics*, 10(10):2252–2258, 1971.

[37] T. Erdogan. Fiber Grating Spectra. *Journal of Lightwave Technology*, 15(8):1277–1294, 1997.

[38] R. Kashyap. *Fiber Bragg Gratings*. Elselvier Inc., 2010.

[39] F. Gan and L. Xu. *Photonic Glasses*. World Scientific Publishing Co. Pte. Ltd., 2006.

[40] G. Brambilla, V. Pruneri, L. Reekie, and D. N. Payne. Enhanced photosensitivity in germanosilicate fibers exposed to CO_2 laser radiation. *Optics Letters*, 24(15):1023–1025, 2008.

[41] A. Othonos. Fiber Bragg Gratings. *Review of Scientific Instruments*, 68:4309–4341, 1997.

[42] M. Douay, W. X. Xie, T. Taunay, P. Bernage, P. Niay, P. Cordier, B. Poumellec, L. Dong, J. F. Bayon, H. Poignant, and E. Delevaque. Densification involved in the UV-based photosensitivity of silica glasses and optical fibers. *Journal of Lightwave Technology*, 15(8):1329–1342, 1997.

[43] H. L. Rogers. *Direct UV-written Bragg gratings for waveguide characterisation and advanced applications*. PhD thesis, 2013.

[44] I. Petermann, B. Sahlgren, S. Helmfrid, A. T. Friberg, and P. Fonjallaz. Fabrication of advanced fiber Bragg gratings by use of sequential writing with a continuous-wave ultraviolet laser source. *Applied Optics*, 41(6):1051, 2002.

[45] K. Hsu, L. Sheu, K. Chuang, S. Chang, and Y. Lai. Fiber Bragg grating sequential UV-writing method with real-time interferometric side-diffraction position monitoring. *Optics Express*, 13(10):3795, 2005.

[46] M. Gagné, L. Bojor, R. Maciejko, and R. Kashyap. Novel custom fiber Bragg grating fabrication technique based on push-pull phase shifting interferometry. *Optics express*, 16(26):21550–21557, 2008.

[47] R. H. S. Bannerman, J. C. Gates, C. Holmes, P. L. Mennea, C. Sima, and P. G.R. Smith. Fiber Bragg gratings fabricated using highly detunable small-spot uvwriting around 1550 nm. *BGPP - Photonics and Fiber Technology Congress*, 1:1–2, 2016.

[48] G. D. Emmerson, S. P. Watts, C. B. E. Gawith, V. Albanis, M. Ibsen, R. B. Williams, and P. G. R. Smith. Fabrication of directly UV-written channel waveguides with simultaneously defined integral Bragg gratings. *Electronics Letters*, 38(24):1531–1532, 2002.

[49] S. L. Scholl, A. Jantzen, R. H. S. Bannerman, J. Field, J. C. Gates, L. J. Boyd, P. G. R. Smith, and C. Holmes. Classification of Small-Spot Direct UV Written Fiber Bragg Gratings Through Extreme Thermal Treatment. pages 3–4, 2018.

[50] A. Jantzen, R. H. S. Bannerman, S. A. Berry, J. C. Gates, P. C. Gow, L. J. Boyd, P. G. R. Smith, and C. Holmes. Observations from direct UV-written, non-hydrogen-loaded , thermally regenerated Bragg gratings in double-clad photosensitive fiber. *Optics Letters*, 42(19), 2017.

[51] S. L. Jantzen, R. H. S. Bannerman, A. Jantzen, P. Mennea, D. Smith, J. C. Gates, L. J. Boyd, P. G. R. Smith, and C. Holmes. Individual inscription of spectrally

multiplexed Bragg gratings in optical multicore fiber using Small Spot Direct UV Writing. *Optics Express*, 28(14):21300–21309, 2020.

[52] C. Holmes, J. C. Gates, L. G. Carpenter, H. L. Rogers, R. M. Parker, P. A. Cooper, Sima Chaotan, F. R. Mahamd-Adikan, C. B.E. Gawith, and P. G. R. Smith. Direct UV-written planar Bragg grating sensors. *Measurement Science and Technology*, 26(11), 2015.

[53] Thorlabs. Datasheet: Single Mode Fibre - SMF28. www.thorlabs.com, Acceessed on 24 February 2021.

[54] Thorlabs. Datasheet: Photosensitive Single Mode Fibre - GF4A. www.thorlabs.com, Acceessed on 24 February 2021.

[55] Thorlabs. Datasheet: Polarization Maintaining Single Mode Optical Fibre - PS-PM980. www.thorlabs.com, Accessed 24 February 2021.

[56] A. Cusano, A. Cutolo, and J. Albert. *Fiber Bragg Grating Sensors: Research Advancements, Industrial Applications and Market Exploitation*. Bentham Science Publishers Ltd., 2015.

[57] B. S. Kawasaki, K. O. Hill, D. C. Johnson, and Y. Fujii. Narrow-band Bragg reflectors in optical fibers. *Optics Letters*, 3(2):66–68, 1978.

[58] G. M. H. Flockhart, W. N. MacPherson, J. S. Barton, J. D. C. Jones, L. Zhang, and I. Bennion. Two-axis bend measurement with Bragg gratings in multicore optical fiber. *Optics Letters*, 28(6):387–389, 2003.

[59] E. Lindley, S. Min, S. Leon-Saval, N. Cvetojevic, J. Lawrence, S. Ellis, and J. Bland-Hawthorn. Demonstration of uniform multicore fiber Bragg gratings. *Optics Express*, 22(25):31575–31581, 2014.

[60] A. Donko, M. Beresna, Y. Jung, J. Hayes, D. Richardson, and G. Brambilla. Point-by-point inscription of Bragg gratings in a multicore fibre. *CLEO-Pacific Rim*, 2017.

[61] R. J. Williams, R. G. Krämer, S. Nolte, and M. J. Withford. Femtosecond direct-writing of low-loss fiber Bragg gratings using a continuous core-scanning technique. *Optics Letters*, 38(11):1918–1920, 2013.

[62] R. Hui and M. O'Sullivan. *Fibre Optic Measurement Techniques*. Elsevier Ltd, 2009.

[63] R. Duncan, B. Soller, and D. Gifford. OFDR-based distributed sensing and fault detection for single-and multi-mode avionics fiber-optics. *Joint Conference on Aging Aircraft*, 2007.

[64] B. Soller, D. Gifford, M. Wolfe, and M. Froggatt. High resolution optical frequency domain reflectometry for characterization of components and assemblies. *Optics Express*, 13(2):666–674, 2005.

[65] R. M. Ridder and C. G. H. Roeloffzen. *Wavelength Filters in Fibre Optics*. Springer Verlag, 2006.

[66] Agilent Technologies. Datasheet: Agilent 81600B Tunable Laser Source Family User's Guide, 2005.

[67] Agilent Technologies. Datasheet: Keysight Technologies Power Sensor Modules Optical Heads Return Loss Modules.

[68] Thorlabs. Datasheet: Retroreflector. www.thorlabs.com, Accessed on 12 June 2021.

[69] IBM. Optical storage, https://www.ibm.com/docs/en/i/7.4?topic=solutions-optical-storage. Accessed on 04 August 2021.

[70] H. H. Peek. The emergence of the compact disc - History of Communications. *IEEE Communications Magazine*, 48(1):10–17, 2010.

[71] J. Van De Plassche, R and H. J. Schouwenaars. A Monolithic 14 Bit A/D Converter. *IEEE Journal of Solid-State Circuits*, 17(6):1112–1117, 1982.

[72] D. G. Hough. The IEEE Standard 754: One for the History Books. *Computer*, 52(12):109–112, 2019.

[73] J. Ganssle. *The Firmware Handbook: Chapter 14 - IEEE 754 Floating Point Numbers*. Newnes, 2004.

[74] K. P. Bogart. *Combinatorics Through Guided Discovery*. CreateSpace Independent Publishing Platform, 2017.

[75] J. H. van Lint. *Introduction to Coding Theory*. Springer Verlag, 1991.

[76] S. Lin and D. J. Costello. *Error Control Coding: Fundamentals and Applications*. Prentice-Hall Series in Computer Applications in Electrical Engineering, 1983.

[77] L. Hanzo, T.H. Liew, and B.L Yeap. Turbo Coding, Turbo Equalisation and Space-Time Coding: For Transmission over Fading Channels. John Wiley and Sons Ltd., 2002.

[78] M. Lal-Sani. *An Approach towards Reducing Transmit Signal Power Consumption in Digital Communication by Use of Low Overhead Multiple Error Correcting Code*. PhD thesis, 2018.

[79] R. H. Morelos-Zaragoza. *The Art of Error Correcting Coding*. John Wiley and Sons Ltd., 2006.